Tomographic Reconstruction of the Morphology of Silicon Nanoparticle Clusters

Stephen David Jones

A thesis presented for the degree of

DOCTOR OF PHILOSOPHY

Department of Physics

Faculty of Science

University of Cape Town

October 2014

Abstract

Semiconducting silicon nanoparticles and nanoparticle clusters are studied using conventional TEM, high resolution TEM and transmission electron tomography techniques. TEM and TEM based tomography provide the means to determine the size and morphology of primary particles and clusters, while the structure of printed macroscopic layers has previously been characterised via small angle X-ray scattering (SAXS). High resolution TEM studies were also carried out on the nanoparticles at high magnification in order to examine the internal structure of the nanoparticles, which is found to contain both ordered as well as amorphous regions. As the nanoparticle clusters studied in this work are tightly bound, dense structures, traditional alignment techniques do not produce satisfactory alignment of the micrographs from which the tomograms are reconstructed, resulting in reconstructions which possess significant artifacts. This limitation is overcome by the development of a new correlation based alignment technique which produces superior alignment when compared to previous techniques, especially in the case of dense samples. The resulting alignment has allowed for the reconstruction of tomograms from which morphological information of the nanoparticle clusters is inferred. The clusters are found to be tightly bound hierarchical clusters, consisting of a large central core surrounded by smaller particles, whose surfaces are faceted. The morphological information gained from the tomography studies has been combined with the macroscopic structure of the layers to infer the arrangement of the nanoparticle clusters within the particle network of the printed layers.

“Nothing has such power to broaden the mind as the ability to investigate systematically and truly all that comes under thy observation in life.”

Marcus Aurelius - Emperor of Rome

Acknowledgements

To my supervisors, Professors Margit Härting and David Britton, for your support, dedication and assistance throughout the course of this work, thank you.

To my betters, Sidney and Estelle Jones, thank you for inspiring me to reach my potential and for endowing me with the skills needed to do so. One could not ask for better parents. I am as proud of you as I hope you are of me.

To my dearest Raegan, thank you for the love, support and kindness that you have shown me all these long years and for the years to come.

To my sister, Debi Croucher, and her family, thank you all for your support over the years.

To my equals, Uli Männl, Rudi Nüssl, Emmanuel Jonah, Batsi Magunje and the rest of the members of the NanoSciences Innovation Centre past and present, thank you for your camaraderie and support, both academically as well as in the lab.

To Stanley Walton, thank you for your assistance with space, time and other writing implements, it has proved to be invaluable.

To those who are no longer here, Alice Weiner, Jeffrey Weiner and Carl Greeff, thank you for your faith in me, you are all missed. To Hagar Schultz, thank you for providing me with access to and assistance with the vitrography setup. In your absence, I thank you.

To you, the reader, I hope that you find this work as interesting as I.

This work was supported by the NanoPower Africa Project funded by United States Agency for International Development (USAID) through the Higher Education for Development (HED) office, the US Airforce Office of Scientific Research through the project "Nanoparticle Solutions for Printed Electronic Applications" and by the University of Cape Town Vice Chancellors Strategic Fund. S.D. Jones was supported with a bursary from the national Research Foundation (NRF) of South Africa.

Contents

1 Introduction

The field of printed electronics has received much attention, both in the scientific community as well as industry. With the promise of flexible, cost effective and truly ubiquitous computing, printed electronics has made a significant impact on all aspects of contemporary electronics ranging from printed conducting tracks [1], semiconductor junctions [2] to display technology [3]. Although many decades extant, recent advances in the field have seen the creation of electronic devices which not only rival, but in some cases surpass, their conventional electronic counterparts [2, 4, 5]. As printed electronics relies on some form of ink, often containing functional particulate matter, the fields of printed electronics and nanotechnology are inextricably linked. In the case where printed devices are fabricated from functional electronic inks, composed of the nanoparticulate material, binding agents, and thinning agents [6], the particles must form a dense network, with a packing density above the percolation threshold of the material, for charge transport to take place.

Using the silicon nanoparticles under study here, several types of fully printed devices have already been constructed, such as thermistors [4], transistors [7, 5] and solar cells [2]. However, relatively little is known regarding the arrangement of the particles within the printed networks. Clearly, measures of average particle size and shape do correlate with the electronic properties of printed layers produced with such particles, but this information is insufficient to infer structural information of the network within a printed layer composed of well known particles [8]. To gain average particle size and shape information, transmission electron microscopy (TEM) presents a highly accurate means of direct measurement, provided that sample preparation is reliable [9, 10, 11], especially when the particles tend to cluster. Aggregation is particularly problematic for imaging techniques which do not operate in transmission mode, such as scanning electron microscopy (SEM) [12, 13]. In contrast, in transmission mode, information with respect to individual particles can be obtained from particles, clusters and from particles that overlay each another. In this thesis TEM and TEM based tomography are used to char-

acterise the individual silicon nanoparticles in particle clusters [14, 15, 16].

New correlation based alignment methods have been developed to ensure superior alignment of the acquired tomographic data sets when compared to previous techniques [17]. Aside from the improvement in the alignment of a data set, this new method is robust against acquisition artefacts, which arise from automatic data acquisition. A new software package has also been developed which creates both three dimensional test structures as well as two dimensional projections of the test structures, in order to facilitate the testing of various reconstruction and image processing techniques.

TEM and TEM based tomography provide the means to determine the size and morphology of primary particles and clusters, while the structure of macroscopic layers has previously been characterised via small angle X-ray scattering (SAXS), which offers the advantage of transmission while still observing a relatively large sample area with nanoscale precision [18, 19, 20, 21]. TEM and SAXS measurements have previously been combined in studies of nanoparticles and nanoscale precipitates [19, 20, 21, 22], in which good agreement was found between both methods. The work presented here, however, represents the first use of TEM and SAXS to interpret the structural information of printed layers provided by SAXS, based on morphological information for the nanoparticle clusters obtained by electron tomography.

The radii of gyration corresponding to various particulate network arrangements are calculated from the tomograms and the results compared with those obtained from the SAXS experiments, and the network arrangements which reproduce the radii of gyration determined by SAXS are presented.

Each experimental study is presented in its own chapter, along with all associated experimental results. Chapter 2 provides a brief overview of nanoparticulate materials as well as a description of the production of the silicon nanoparticles under study as well as a description of the layer deposition onto substrates. Chapter 3 is concerned with the two dimensional analysis of the Si nanoparticles via electron microscopy. The particles are characterised for size and shape as well as

an analysis of the internal structure at high resolution. Chapter 4 presents the general improvements to the field of microscopy including the synthetic data generation software as well as the new tomography alignment method. In addition to the improvements to electron tomography, chapter 4 presents a three dimensional analysis of the Si nanoparticles via electron tomography with respect to size and shape. Chapter 5 firstly explains the basic principles of SAXS and the necessary concept of the radius of gyration. Using these concepts, the morphology of the primary nanoparticle clusters is related to previous SAXS studies of printed layers to determine the arrangement of the clusters in the nanoparticle network, before the concluding remarks are presented in chapter 6.

2 General Overview of Nanoparticles and Printed Nanoparticulate Systems

This chapter introduces nanoparticulate materials, their production methods as well as their various uses. The chapter begins with a technical definition of a nanoparticle and continues with a brief discussion as to why these systems are of great interest in the physical sciences. An overview of the most common nanoparticle production methods is provided as well as a detailed description with regards to the production of the semiconducting silicon nanoparticles used in this study. The chapter ends with a description of the fabrication of printed layers formed from silicon nanoparticulate inks.

2.1 Introduction to Nanoscale Materials

In the field of nanotechnology a nanoparticle is defined as an object with all three dimensions smaller than 100 nm [23]. Early studies which were performed on nanoscale materials referred to the materials as ultrafine particles [24, 25]. However, towards the end of the 1990's, before the US National Nanotechnology Initiative began to standardise nomenclature as well as classification techniques, the name *nanoparticle* was popularised by the same authors who used the term ultrafine particles [26].

Although often considered a discovery of modern science, artisans have been using nanoparticles for centuries to achieve, for example, the lustre effect which is observable in various types of pottery glazes and glassware as well as in paints [27, 28, 29]. Interestingly, the optical properties of nanomaterials were also documented by Faraday in his paper on the interactions of gold with light [30].

The properties of bulk materials are generally considered to be independent of the size or quantity of material of which they are composed, while in the case of nanomaterials there exist optical material properties which are size dependent [31]. This difference in the material properties may be attributed to the large surface

to volume ratio of nanoparticles [32]. In particular, the the ratio of surface to non-surface atoms, which increases at small particle sizes, is sufficiently large such that the material properties are dominated by the surface states and not by the bulk properties of the material [33].

Other properties of nanoscale structures involve electron confinement, a phenomenon where nanoparticles effectively trap electrons to produce different optical properties compared to those of the bulk material via quantum effects [34, 35, 36]. In the field of photovoltaics (PV) it has been shown that the absorption of solar energy is higher in devices composed of nano particles than in those composed of continuous sheets of thin film materials [37]. In the case of metallic nanoparticles, for example, other nanoscale properties such as surface plasmon resonance (SPR) may appear [38, 39, 40]. SPR, termed localised surface plasmon resonance (LSPR) for nanoscale materials [41, 42], refers to the collective oscillation of the electrons at the surface of a solid or liquid by stimulation from incident light [43]. Magnetic nanoparticles are able to be created from bulk materials such that they exhibit a phenomenon known as superparamagnetism [44, 45, 46], whereby the magnetisation of the material is able to change direction with changing temperature [47].

2.2 Semiconducting Nanoparticles

Semiconducting nanoparticles include metal oxides [48, 49, 50, 51], chalcogenides [52, 53], and elemental semiconductors such as silicon [54]. Metal oxide nanoparticles have found applications in the fields of electronics, computer science [48] as well as medicine [55] and catalysis [56, 57, 58, 59, 60]. Chalcogenides, while widely used for their optical properties [61], have also been used to produce highly efficient thin-film solar cells [62] as well as energy storage devices [63]. Silicon nanoparticles are widely used throughout science as well as industry, with the size, surface properties and morphology of the particles dictating their use. Among the smallest of these nanoparticles are quantum dots, which exhibit electron confinement [64, 65]. Silicon based quantum dots have been used in computer science [66], photovoltaics

[67], display technology [68] and medical applications [69].

Silicon nanoparticles with sizes above the confinement limit may be loosely categorised into two groups: those particles with an insulating layer of silicon dioxide, termed oxide capped, and those without [70], termed uncapped or oxide free. Particles from each group have found different uses in contemporary nanotechnology. Clearly, oxide capped semiconducting nanoparticles are not ideal for the fabrication of devices which rely on the transport of charge through networks composed of nanoparticles. These particles are, however, extensively used in medical applications [71] as well as for their optical properties [72].

Uncapped semiconducting nanoparticles, such as the particles studied here, are well suited to the fabrication of semiconducting layers as the charge transport is not impeded by the oxide layer [73]. In a network, the silicon nanoparticles presented here differ from bulk silicon in that they possess thermally specific activated charge transport properties [73, 4]. These properties have led to the successful development of the many printed electronic devices outlined in the introduction.

2.3 Nanoparticle Production

2.3.1 The Top-Down and Bottom-Up Approaches

Knowledge regarding the production of nanoparticles is important as material properties may vary depending on the production method used, even in the case of two different particles composed of the same elements. In the case of silicon, nanoparticles produced by chemical vapour synthesis (CVS) methods [74] have significantly different morphological and electronic properties when compared to the silicon nanoparticles investigated in this thesis [75].

There are two main approaches by which nanomaterials are created in contemporary nanoscience, which are generally termed termed *top down* and *bottom up*. In the top down approach nanoparticles are created by the reduction in size of bulk materials, while in the bottom up approach nanoparticles are created by the

assembly of atoms or molecules [76]. The most common bottom up techniques include CVS [77] as well as aerosol [78] and liquid phase methods [79].

The most straightforward form of top down nanoparticle production is milling, in which bulk materials are reduced to nanoscale particles by comminution in a ball-, vertical-, or planetary mill or some other such mechanical hardware [80, 81, 82]. Other common top down techniques also include photolithography [83] and electron beam lithography [84, 85].

2.3.2 Silicon Nanoparticle Production by High Energy Milling

Particle size reduction, termed comminution or milling in industry, is defined as the mechanical breakdown of solids into smaller particles [86]. In addition to increasing the surface area of solids, milling is also able to increase the number of regions of high activity within the sample [87]. The relationship between comminution energy and milled particle size to the initial feedstock size, has been researched extensively, and is fundamental to comminution theory [88, 89, 90]. The spatial distribution of the imparted energy is typically non-uniform, with high concentrations of energy distributed around holes, corners, cracks or other material defects [91, 92].

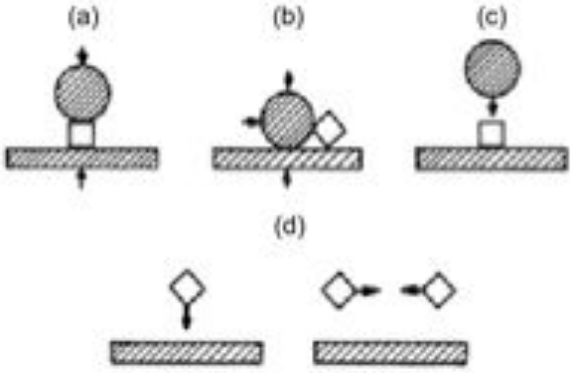

Figure 2.1: Primary force types observed in milling. The milling media are shown as shaded objects, while the material being milled is shown as white solid objects. The black arrows represent applied forces: (a) compression; (b) shear; (c) stroke impact; (d) impact collision [93].

The primary force types observed in a typical mill are shown in figure (2.1) [93]. Figure (2.1a) shows compression, where the milling medium applies a force perpendicular to the material without collision. Figure (2.1b) shows the application of a shear force to the sample, which leads to the process referred to as attrition. In contrast, in figure (2.1c), the forces involved in the collision between milling media and the feedstock against the wall of the mill are shown. This manner of collision is referred to as stroke impact. Both of the figures under figure (2.1d) show the feedstock colliding with either the mill wall or other material being milled, without a collision with the milling media. This is termed impact collision, which can also lead to fracturing [93].

In general, vibration mills have been used extensively for the production of fine particles as well as nanoparticles with induced mechanical activation [94, 95]. The milling chamber is constrained to move along a circular or elliptical orbit by the rotation of large internal weights, which are out of balance. The resulting three dimensional motion may be described by four variables: the frequency of the vibration, the horizontal and vertical vibrational amplitudes, and the phase angle [96]. Typical values of frequency and amplitude are of the order of 20 rev/s and 10 cm respectively.

The semiconducting silicon nanoparticles under study in this thesis were created via the high energy milling of bulk metallurgical grade silicon. The mill used for nanoparticle production was an 800W vibration mill, manufactured by Siebtechnik. The silicon used in this work is 2503 grade metallurgical silicon supplied by silicon Smelters, Polokwane, South Africa. Prior to each milling session, the milling apparatus was cleaned by first milling silica for 5 minutes and then cleaning the milling media, consisting of the milling chamber, or mortar and the pestle, with acetone and ethanol, to avoid any risk of contamination. Three sample types were produced, each differing in total milling time and thus total milling energy. The bulk of the work will be focussed on 300 minute continuously milled silicon, with 90 and 15 minute milled silicon also examined by high resolution two dimensional electron microscopy imaging, presented in Chapter 3.

2.4 Printed Silicon Layers

The silicon nanoparticles mentioned above are used as the functional pigment in water-based inks with an acrylic screen printing binder (PST Sensors (Pty) Ltd, South Africa). In this water-based ink, where the acrylic monomer polymerizes by hydrolysis at ambient temperature, propan-1, 2-diol (propylene glycol) was used as a thinner as well as a retarder [97, 98]. The role of the thinner was to create thixotropic inks with viscosities conducive to screen printing, the compositions of which were determined according to the weight ratios of the silicon nanoparticles to the commercial binder for complementary SAXS. Inks were produced with 20%, 50%, 60%, 70% and 80% particles by weight, with the balance of the weight coming from the commercial binder.

Deposition of the nanoparticle inks onto substrates was achieved with conventional screen printing techniques. The substrate used was 100 μm thick polyester terephthalate (PET) and the printer used for deposition was an ATMA AT-60PD semi automatic flatbed screen printer. The structures which were printed were squares with sides of length 1.5 cm, with samples produced for each of the five inks described above. The geometric parameters were chosen to conform to the experimental requirements of the SAXS measurements, presented in chapter 5.

3 Two Dimensional Analysis of Si Nanoparticles

This chapter describes electron microscopy based studies to investigate the size and give the first indication of the morphology and internal structure of the silicon particles produced by the high energy milling process described in the previous chapter. In addition the fundamentals of electron microscopy, which form the basis of the new approaches presented in chapter 4, will be discussed.

3.1 Introduction to Transmission Electron Microscopy (TEM)

The resolution of any optical instrument, taken as the ability of the instrument to distinguish between two closely spaced points, known as the diffraction limit, is given by [99]

$$d \equiv \frac{\lambda}{2N_A}, \tag{3.1}$$

where λ is the wavelength of the radiation used, and N_A is the numerical aperture of the instrument, which is a dimensionless metric which characterises the angular acceptance of the system in a particular medium. As an example, a modern optical microscope with a 650 nm light source with air as an external medium, has a resolving power of only 342 nm [100]. In order to increase the resolution of traditional optical systems, light sources of shorter wavelength have been used to increase the resolution to approximately 200 nm. The electron microscope is, in principal, similar to the optical microscope, with the exception being the use of an electron beam in place of an optical light source. As the wavelength of the electron beam is significantly smaller than that of visible light, 0.005 nm vs 200 nm, the diffraction limit of the electron beam is much lower and, consequently, the resolution is orders of magnitude greater for a similar numerical aperture. In practice TEM instruments are limited, not by the diffraction limit of the electron beam, but rather by imperfections in the electron lenses used to achieve focus and magnification, which cause distortions in acquired images. These distortions, referred to as

spherical and chromatic aberrations, may be corrected for by installing additional hardware, termed aberration correctors, in the TEM instrument [101, 102].

Electron microscopy may be categorised into two groups: transmission electron microscopy (TEM) and scanning electron microscopy (SEM), as shown in figure (3.1). In the case of scanning electron microscopy, both the detector and the beam are positioned on the same side of the sample, with a raster image formed by the deflection of backscattered or secondary electrons emitted from different points on the surface [103]. In the case of transmission electron microscopy, the sample is positioned in between the electron beam and the detector. Thus a direct image is formed in the image plane of the microscope by the beam of electrons which have penetrated the sample entirely. One of the key differences between the two techniques is the energy imparted to the electron beam, approximately 300 kV v.s. 15 kV for TEM and SEM respectively [104, 103]. This significant difference in beam energy allows the probing of near atomic scale structures in the case of the TEM, while the resolution of a typical SEM is limited to a few nanometers. As the observed TEM image is formed from transmitted electrons, TEM is able to yield structural information regarding the sample, while the SEM signal, composed of deflected electrons, is typically used to study surface properties of the sample.

As the transmission cross-section of the electrons varies inversely as the thickness of the sample, areas which are thicker will produce fewer transmitted electrons and appear darker in the micrograph, whereas thin areas will appear brighter in micrographs. This form of contrast is termed *mass thickness contrast* in the literature. In the case of crystalline materials, such as the silicon nano particles under study here, an additional contrast is observed in acquired images which is due to variations in the intensity of the acquired diffracted beam across the sample. The diffracted beam yields information regarding both the general crystal orientation relative to the electron beam, also known as the crystal phase, as well as local changes in crystal orientation [105]. Contrast arising from the diffracted beam is termed *diffraction contrast* in the literature. Changes in the relative phases of the electrons in the transmitted beam give rise to a third contrast, known in the

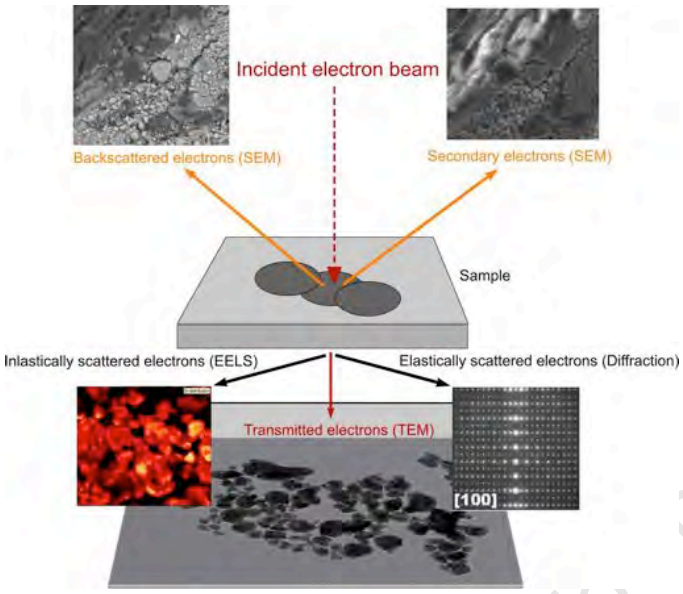

Figure 3.1: Schematic representation of the differences between TEM and SEM.

literature as *phase contrast*. Phase contrast imaging remains the highest resolution of all TEM imaging techniques, even allowing the imaging of individual columns of atoms [105]. The overall contrast observed in acquired TEM images is the superposition of the mass thickness, diffraction and phase contrast mechanisms. Thus all transmitted electron micrographs acquired are density images.

The high energy electrons which constitute the primary beam are generated by an electron gun, which produces a fine beam of electrons of precise energy, from a small source region by either thermionic emission or field emission [106] and then imparting energy to the electrons by accelerating them through a region of high potential. As the electrons travel at velocities comparable to the speed of light [107], their relativistic wavelength is given by

$$\lambda = \frac{h}{\sqrt{2m_0eV\left(1+\frac{eV}{2m_0c^2}\right)}}, \tag{3.2}$$

where V is the accelerating potential, m_0 is the rest mass of an electron, e is the electronic charge, h is Planck's constant and c is the speed of light in vacuum. In

the case of thermionic electron sources, the current density of the source is given by Richardson's law [108, 109] and in the case of field emission sources, the current density can be estimated from the Fowler-Nordheim formula [110].

As both field emission and thermionic electron sources produce beams which are divergent over the length of the microscope column, the beam must be focused to a point on the sample. In classical electron microscopy, lenses which use combinations of electrostatic and magnetic fields are used to achieve magnification and focus. These electron lenses, have a focal length which is defined as [111]

$$f = \frac{K \cdot V^{\,2}}{(N \cdot I)}\,, \tag{3.3}$$

where K is a lens constant, N the number of windings and I the current of the lens. In modern TEM instruments magnification and focus are achieved by the use of magnetic lenses, devices which focus or deflect the electron beam by making use of the magnetic Lorentz force [106]. Magnification of the sample in the image plane of the microscope is achieved by multiple stacking of electron lenses. There are five primary electron lens types common to all TEM instruments. These lenses are termed gun lenses, projector lenses, condenser lenses, objective lenses and stigmator lenses.

The gun lens is used to form a fine beam immediately after emission, while the condenser lens is used to control the spot size of the beam. Thus the gun and condenser lens also define the total beam current. The objective lens is usually an immersion lens which occupies a dual role as it is used both to focus the electron beam and provide the first stage of magnification, while the projector lens controls the final stage of magnification. The stigmator lens corrects for astigmatism, caused by deviations in the precise circular symmetry of the pole piece.

The electron beam, which forms the image in the image plane of the microscope, has two components resulting from three primary beam-sample interactions as shown in figure (3.1): unscattered or transmitted electrons, elastically scattered or diffracted electrons and inelastically scattered electrons [112, 113]. Imaging

which makes use of the interference between the unscattered and scattered beams is known as bright field imaging in the literature and forms the basis of the experiments to follow.

3.2 Experimental

3.2.1 Sample Preparation

The silicon nanoparticles were produced as described in section (2.3.2), with their differences owing to the milling time chosen. For the particle size characterisation, presented in section (3.2.2) below, particles produced by milling the feedstock for 300 minutes were used, while for the high resolution TEM (HRTEM) characterisation of the internal structure, presented in section (3.2.3), two additional samples, produced by milling for 90 and 15 minutes respectively, were used. For TEM sample preparation, the powders were dispersed in methanol and sonicated using a bath sonicator for approximately 7 seconds in order to break up large agglomerates. The sonicated dispersions were dropped onto holey carbon coated grids using a micro-pipette. In high resolution TEM this allows the viewing of fine structures in objects which lie partially over a hole. For the conventional TEM analysis, to determine the particle size distribution, plain carbon grids were used, which allowed for a greater density of sample material per grid.

3.2.2 Transmission Electron Microscopy

The microscope used for data acquisition was an FEI T20 TEM, fitted with a Lanthanum Hexaboride (LaB_6) filament. As the magnification required for size classification is relatively low, the LaB_6 filament provides a higher current density for a wide field of view at low magnification when compared to a field emission gun (FEG), which, as a direct result of small source size, does not allow for the illumination of large sample areas at low magnification [108]. Micrographs were acquired at a magnification of 10kX at an accelerating voltage of 200kV. The Gatan

imaging camera used in the T20 was set to acquire images of size 2048×2048 pixels at a pixel resolution of 4Å. In order to enhance the appearance of edges, all images were acquired at a constant defocus of $-2\mu m$.

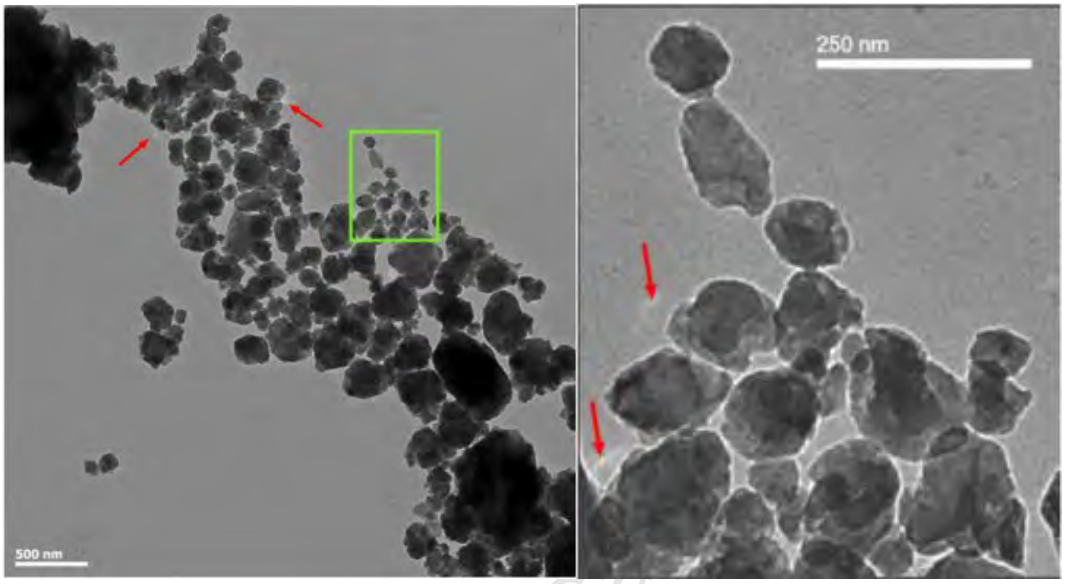

(a) (b)

Figure 3.2: A subset of the TEM images used to determine particle size information of the milled silicon particles. (a), a low magnification micrograph and (b), an enlarged view of the highlighted rectangular region in (a).

Figure (3.2) shows a micrograph of silicon particles produced by milling for 300 minutes. Upon first inspection it is clear that a large amount of sample material is visible on the TEM grid, which is a direct result of the use of plain carbon grids. It is also clear that many of the structures appear not to be single particles but rather agglomerates or clusters of nanoparticles of varying size. From an examination of the contrast in figure (3.2a) it is clear that the sample material on the grid is polydisperse with respect to its thickness distribution, as the observable greyscale values range from light grey, corresponding to a high transmission, to black, corresponding to zero transmitted beam current. However, the regions which correspond to zero beam current appear far less often and correspond to very large agglomerates rather than single particles or small clusters. In

bright field imaging, particles which lie close to a zone axis tend to appear darker. This phenomenon, known as the *zone axis condition* in the literature, results in a stronger diffraction component of the transmitted beam, which results in stronger contrast in the bright field images [105]. In this case, however, the darker regions in figure (3.2) are as a result of the thickness of the sample. The aspect ratios of both particles and clusters appear to be greater than unity, which may imply that the larger particles are, in fact, clusters of smaller particles, as previously inferred from SAXS and SEM studies [114].

From the enlarged view shown in figure (3.2b), it can be verified that many of the structures visible in (a) are, in fact, not single nanoparticles but are rather the primary clusters of nanoparticles, as these structures possess internal structure at the higher magnification. As the nanoparticles are semiconducting, beam-sample charging effects are present and are observable as the white ghosting artefacts, indicated by the red arrows, which appear to extend outwards from the edges of some of the particle clusters. As the ghosting obscures neither cluster shape nor size, it does not negatively affect the analysis. In contrast, the well-defined white outlines, termed *Fresnel Fringes* in the literature, which are visible around the perimeters of most of the particles as well as clusters, are the intended effect of the previously mentioned defocus used to enhance the appearance of sample edges. The Fresnel fringes are as a result of electron diffraction of the electron beam from the sharp edges of the sample. The superposition of these diffracted waves creates a standing wave interference pattern, which is visible as a white outline in the case of defocus and as a black outline in the case of over focus [108].

As the average shape of the clusters appears ellipsoidal, measurement of both the long axis and the short axis of each particle or cluster is required in order to characterise their average size and shape. The long and short axes are defined for an arbitrary ellipse in figure (3.3), where a is the minor axis and b the major axis of the ellipse irrespective of its orientation.

Thus, measuring both the long and short axes of sufficiently many primary clusters should yield both the size distribution and quantitative information on their aspect

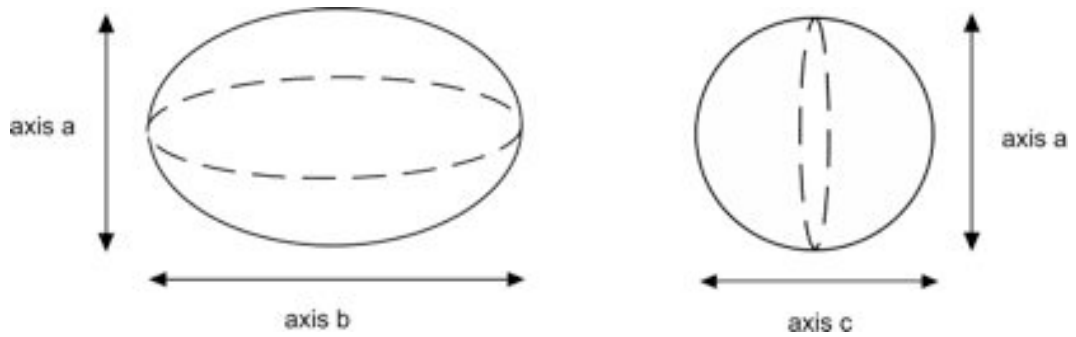

Figure 3.3: Definition of the long and short axes used for particle size characterisation.

ratio. The aspect ratio for a single biaxial particle is defined as

$$A = \frac{b}{a}, \tag{3.4}$$

and for a distribution of biaxial particles is defined as

$$\bar{A} = \frac{1}{N} \sum_{i=1}^{N} \frac{b_i}{a_i}. \tag{3.5}$$

Two different micrographs of the same sample have been found to yield similar results with respect to morphology. In addition micrographs of two different samples from the same batch have also been found to yield similar results with respect to morphology, which indicates that the particle production methods are consistent. Consequently, all of the experimental data has been combined into a single large dataset, consisting of approximately 3400 particle clusters. Figure (3.4) shows the combined long and short axis size distributions and the aspect ratio in the form of histograms.

In order to model the morphology of the nanoclusters, a log-normal distribution

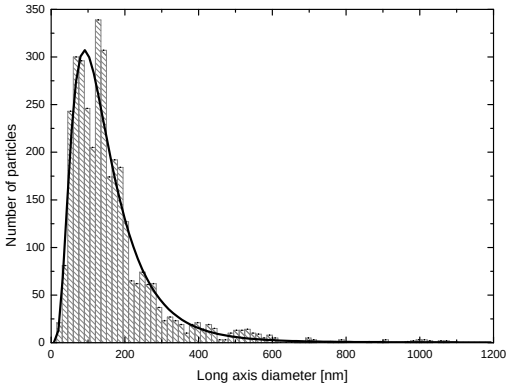

(a)

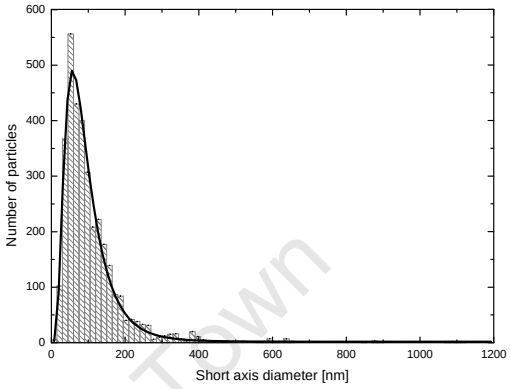

(b)

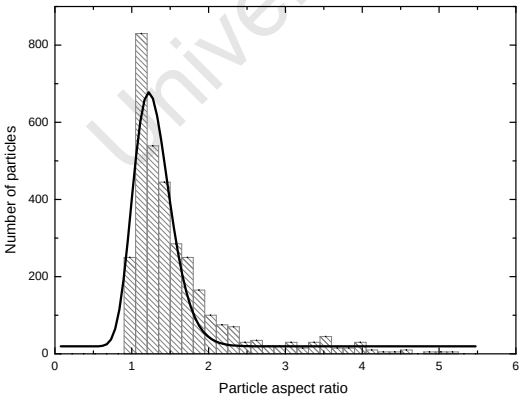

(c)

	μ (nm)	σ (nm)	r^2
Long Axis	126.7	3.4	0.95
Short Axis	78.4	1.2	0.93
Aspect Ratio	1.3	0.1	0.96

(d)

Figure 3.4: A summary of all TEM based size distribution data with lognormal fits in black, used to gain quantitative information about the morphology of nanoparticle clusters: (a) the long and short axis size distribution, (b) the short axis size distribution, (c) the particle aspect ratio, and (d) summary of fitting results.

was fitted to the histogram data shown in figure (3.4),

$$y \equiv y_0 \frac{A}{\sqrt{2\pi}\sigma x} e^{-} \left(\frac{ln\left(\frac{x}{\mu}^2\right)}{2\sigma^2} \right), \tag{3.6}$$

where σ, μ and A are the logarithmic standard deviation, mean and intensity of the distribution respectively. The log-normal distribution was chosen because it is well suited to modelling data which contain peaks which are not symmetric, of the kind visible in the histograms of figure (3.4), which all appear to possess tails to the right and which are bounded by zero as a minimum.

Figures (3.4a) and (3.4b) show histograms of the combined long and short axis data respectively, with log-normal distributions fitted to both sets of data. The aspect ratio plot presented in figure (3.4c) shows the shape distribution data calculated from the TEM measurements, also with a log-normal fit to the data, while the table in figure (3.4d) summarises the fit results. At first glance it may appear that a bimodal distribution function would better describe the data presented in (3.4a). However when the standard histogram error, taken as $\frac{1}{\sqrt{n}}$, where n is the number of counts in the histogram bin, is taken into account, a single peak function is sufficient to describe the data, which is confirmed by the correlation value seen in the table shown in (3.4d).

The long and short axes have values of 126 ± 3nm and 78 ± 1nm respectively. As can be seen from the histogram data, as well as from figures (3.4a) and (3.4b), the average shape is indeed elliptical, with the most commonly observed distribution aspect ratio taking on a value of approximately 1.3.

Aside from the largest peaks, it is interesting to note the significantly smaller peaks in the distributions, which appear at around 560nm in figure (3.4a) and at around 340nm in figure (3.4b). As the smaller peaks possess an intensity of the order of 20 counts and a width of approximately 5 histogram bins fitting of these peaks was not attempted. These secondary peaks correspond to the sizes of the large clusters observed in the TEM images and have an aspect ratio of approximately

1.6, larger than that calculated from the mean cluster dimensions.

The ratio of the larger to smaller peak intensity of the histogram data gives an approximation to the predominance of each cluster size. In the case of the long axis, the ratio takes on a value of 15, which implies that the large clusters are counted only 6% of the time, while in the case of the short axis, the large clusters are included only 4% of the time. Thus the majority of the size distribution data corresponds either to single particles or to small clusters of particles, with little contribution from larger clusters.

3.2.3 High Resolution TEM

The two microscopes used for the data acquisition in the high resolution experiment were the FEI F20 FEGTEM and JEOL JEM 2100 TEM, both fitted with field emission gun electron sources. The FEG sources are far superior for HRTEM when compared to LaB_6 filaments as they provide a brightness, or electron density, increase at the specimen plane of the order of 10^3 at higher magnification, with a narrow field of view [108]. Micrographs were acquired at a magnification of 100kX at an accelerating voltage of 200kV. Both CCD cameras were set to acquire images of size 4096×4096 pixels at a pixel resolution of 1Å. As the goal of this experiment was to observe fine structure, a lower defocus was used than for the size distribution analysis.

Figure (3.5) shows representative images acquired during the high resolution experiment. Figure (3.5a) shows the data acquired for the 300 minute milled particles, on the T20 and figures (3.5b) and (3.5c) show the data acquired for the 90 and 15 minute milled particles respectively, on the JEOL 2100. From the real space images, it can be concluded that the surfaces of the particle clusters are composed of regions which appear to possess ordered structure as well as regions which appear to be amorphous. This may be attributed to the milling process, which has been shown to chemically reduce oxides of the semiconductor material, which produces the stable, uncapped surfaces seen in the micrographs [115]. The

Fourier transforms of the micrographs, shown on the right of the figures, depict the crystal lattice planes visible at the surfaces, which can be seen as distinct double spot patterns, with greater clarity. The lattice spacings were calculated as the distances between two spots of the same pair, while the associated uncertainties were quantified by the radii of the spots.

Figure (3.6) summarises the results of the lattice plane calculations for all three sample types, with subfigures (a), (b) and (c) depicting the results for 300, 90 and 15 minute milled particles respectively. The known lattice parameters, which are well documented in the literature, for bulk monocrystalline silicon are reproduced for convenience in the table in figure (3.6d). On examination of figure (3.6) it is clear that all produced nano particles possess highly ordered surface regions, regardless of the milling time, and that these ordered regions correspond to crystalline silicon.

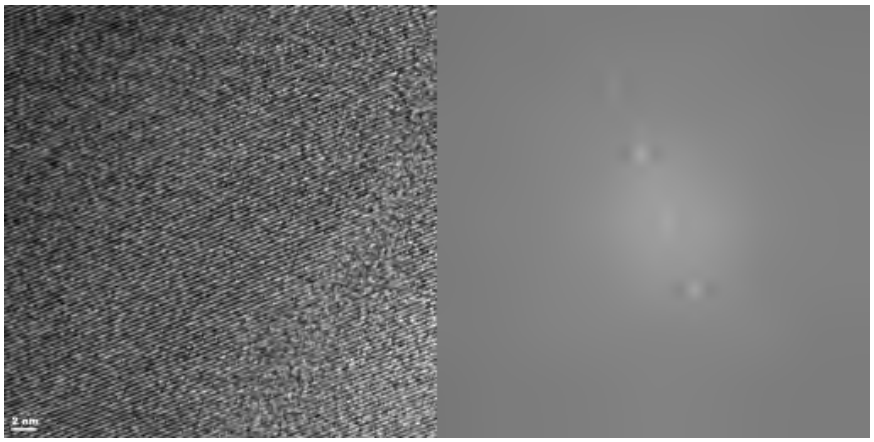

(a)

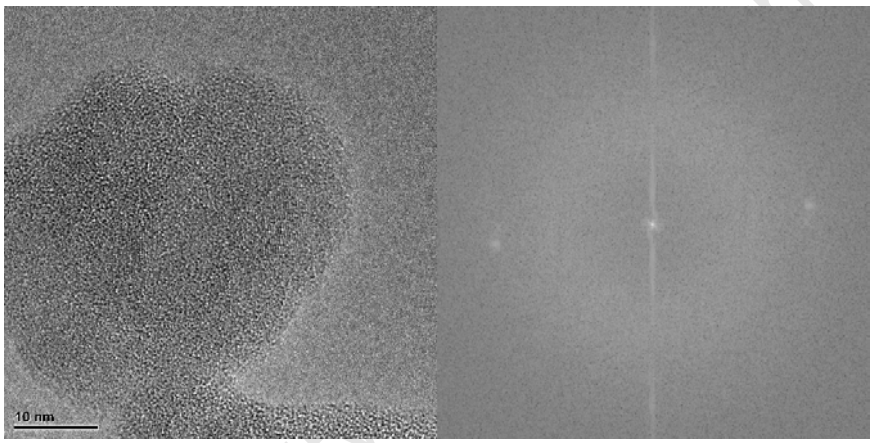

(b)

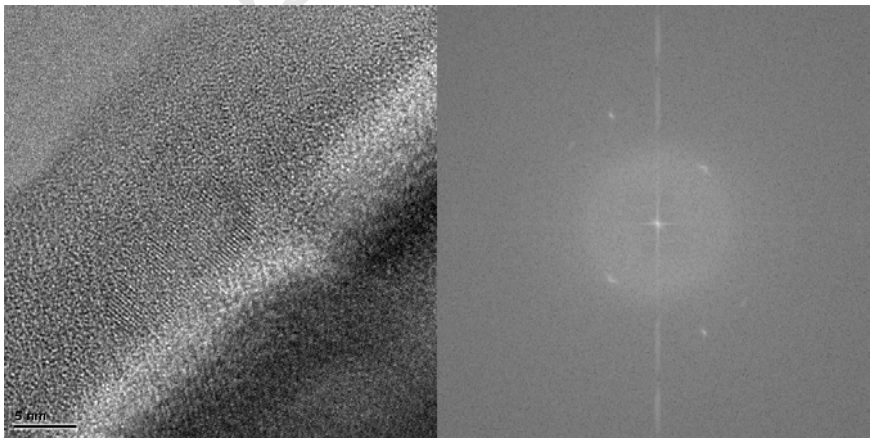

(c)

Figure 3.5: Representative high resolution micrographs (left) and their Fourier transforms (right): (a) 300, (b) 90 and (c) 15 minute milled particles respectively.

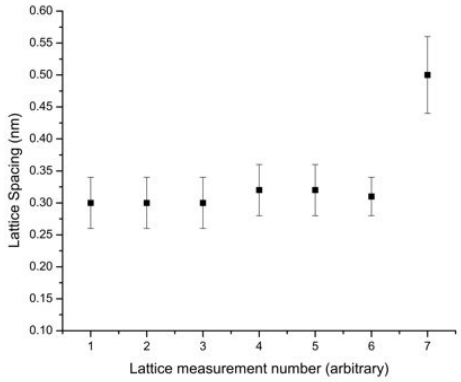

(a)

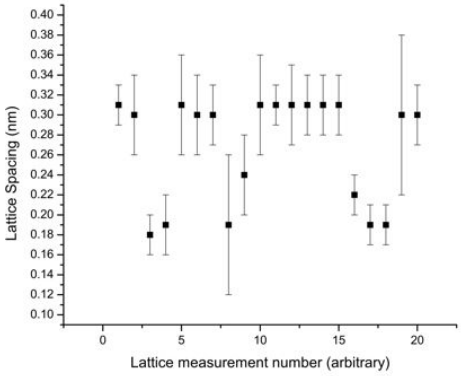

(b)

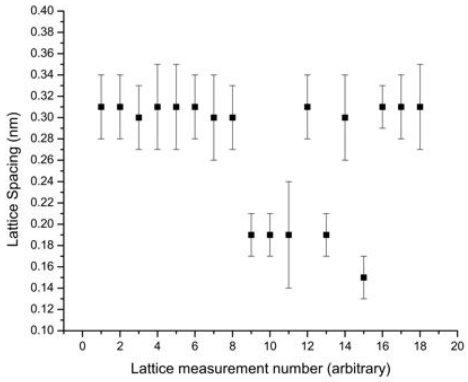

(c)

Plane	Size (nm)
001	0.543
011	0.384
111	0.314
220	0.192
311	0.164
400	0.136

(d)

Figure 3.6: A summary of HRTEM lattice parameter calculation results. (a) 300 minute milled Si, (b) 90 minute milled Si, (c) 15 minute milled Si, (d) the known lattice spacings for silicon.

4 Three Dimensional Analysis of Si Nanoparticles

This chapter describes electron tomography based studies to investigate the size and give the first indication of the morphology and internal structure of nanoparticles and nanoparticle clusters in three dimensions. A new correlation based alignment method, which allows for superior alignment of a tomographic data set when compared to previous techniques, is presented in this chapter. It will be shown that this superior alignment of the data set, in turn, results in superior reconstructions. Computer software which produces statistically distributed virtual phantom data for use in general electron microscopy is also presented. The fundamentals of electron tomography, which form the basis of the new approaches presented in this chapter, are also discussed.

4.1 Electron Tomography and Experimental Procedures

Tomography in general refers to the three dimensional imaging of a sample by sectioning [116]. Derived from the Greek words *tomos*, meaning part or section, and *graphein*, the infinitive "to write", the word tomography literally means to write a part or section. This is accomplished by passing some kind of incident wave, with a penetration depth larger than the physical dimensions of the sample, through the sample and then collecting the wave after interaction with the sample to produce a shadowgraph. The experimental setup used to generate and collect the penetrating beam is referred to as a tomograph, although this nomenclature is not common in electron microscopy, while the resulting three dimensional reconstructed model, is referred to as a tomogram.

Electron tomography, therefore, is a microscopy technique in which a three dimensional representation of a sample is created by reconstruction, from a series of micrographs acquired at various angles on a TEM [117]. These angles, known as tilt angles, fall in a plane perpendicular to the image plane of the microscope [118]. As the images inside a TEM are formed from transmission, the micrographs correspond to a set of projections of the sample at the various tilt angles, as illus-

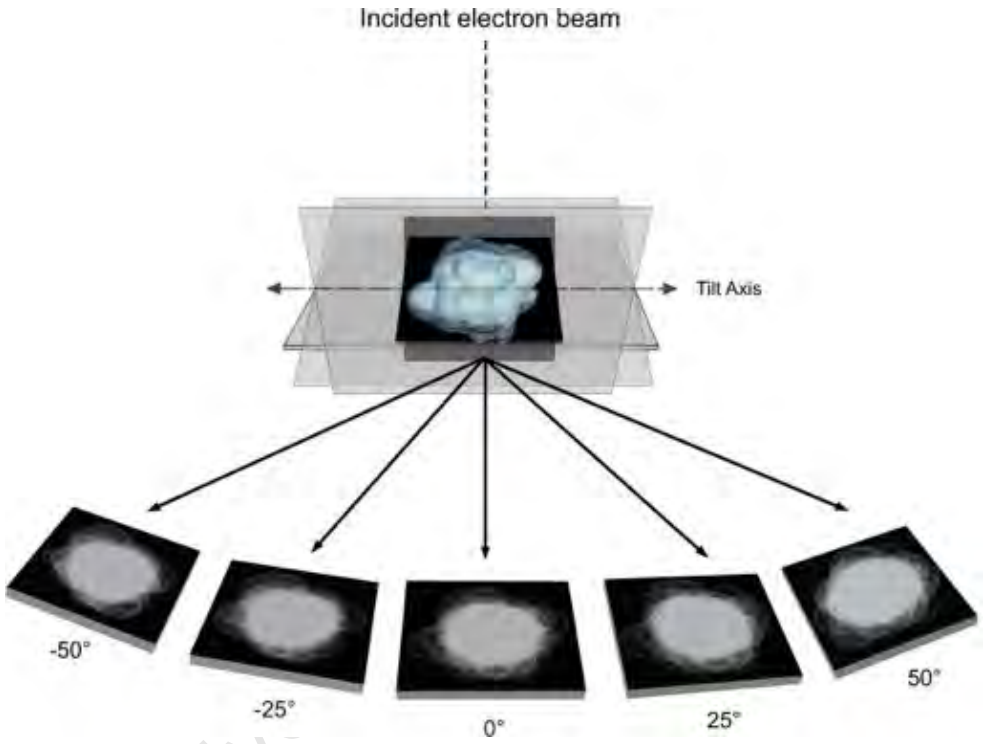

Figure 4.1: Schematic representation of the principles of tomography showing images recorded at different tilt angles of the sample from $-50°$ to $+50°$, about an axis perpendicular to the electron beam.

trated in figure (4.1), which depicts the principles of tomography schematically. A three dimensional model of the sample, as seen in the upper part of figure (4.1), can be reconstructed from the projection images by a number of computational techniques which will be discussed later in this section.

The first step in electron tomography begins with the collection of the sample projection images at the various tilt angles. As contemporary tomography conducted on heterogeneous samples typically involves the acquisition of hundreds, or in some cases thousands, of projection images, the task of image acquisition is generally carried out by automated computer software such as UCSF Tomo, Leginon and others [119, 120, 121, 122, 123, 124]. These software packages, although varied and complex, all offer a similar set of functions. As the Leginon software package was used for all tomography data acquisition presented in this thesis, its features will be discussed in more detail.

In its broadest scope, the Leginon software offers two primary modes of operation: to both automatically locate regions of interest as well as acquire projection images or to automatically acquire projection images of a region manually selected by the operator [119]. All tomographic image series collected for this work were acquired in manual selection mode, which instructs the microscope to automatically acquire images about a manually selected sample location. This was done in order to avoid errors associated with sample occlusion at high tilt angles, as well as to avoid the possibility of the automatic selection algorithm selecting an undesirable sample region.

In a typical tomography experiment the microscope will be required to change magnification, by approximately two orders of magnitude, approximately one thousands times [125]. For each of these magnification changes the electron beam must remain centred on the sample at precisely the same point. These calibrations, essential to the correct functioning of the Leginon system, make use of the transformation matrices between the coordinate system relative to the imaging hardware and the coordinate system relative to the positioning hardware of the microscope and are computed from three images.

These images are acquired at zero shift, at a defined x shift and y shift in two orthogonal directions respectively. The resultant image shifts are computed by phase correlation, a Fourier space image registration technique where the relative translative offsets between two images are calculated. The shifts are used to calculate the necessary transformation matrix, which is stored internally for later use. These transformation matrices must be calculated for every magnification used in data acquisition. Phase correlation is also used for focus as well as astigmatism calibrations. In these cases, a number of images are taken and the response of the microscope to known changes in focus as well as astigmatism are measured and compared to the un-perturbed images.

The CCD cameras used are imperfect and the pixels which constitute the sensors have different responses to the incident beam [126]. These varying pixel responses are corrected for by a process known as flat field imaging or CCD flattening. Flat field images are acquired for each combination of camera settings (size, position, and binning) that will be used throughout data acquisition. These images are acquired by flooding the sample stage without a sample, and by extension, the CCD with a high intensity electron beam. The images are then acquired with an exposure time which results in the CCD pixel intensities taking on values which are approximately half of the dynamic range of the CCD camera. Generally, in practice three images are acquired and averaged together to produce the final flat field image. This image contains all variations of pixel intensity due to varying pixel response, optical distortion which may arise from dirt or microscopic damage to the CCD, and any machine bias which may influence the acquired images. The final flat field image contains the unique watermark or vignette of the CCD, which may then be used to correct all future images.

Although automatic data acquisition in electron tomography is both robust and accurate, both the software techniques and the microscope hardware are imperfect [120]. As a result, the images which are acquired are misaligned with respect to each other. That is to say, a feature which appears in the centre of one tilt series image will most likely appear off centre in the neighbouring images [127].

This tilt seres misalignment must be corrected prior to any three dimensional reconstruction in order to avoid catastrophic irregularities and artefacts in the final tomogram [128]. The alignment of tilt series images in electron tomography is an ongoing research topic, with improvements in the form of new software techniques as well as mathematical methods being published regularly [129]. As a new alignment technique is presented in this thesis, the discussion of alignment in electron tomography is deferred to Section (4.2) in which the new alignment technique is explained in the context of the current research in the field.

Once the acquired tilt series has been aligned, the next step towards building the final tomogram is creating the initial three dimensional reconstruction, which is later refined to form the final model of the sample. One of the most easy to implement reconstruction techniques used in electron tomography is known as back projection (BP) [130]. Figure (4.2a) depicts the acquisition of a tomographic data set, with the sample represented by the geometrical arrangement within the square, the rays of the transmitted electron beam by the black arrows and the acquired projection images in the form of intensity profiles which surround the sample, located at the bottom of the figure. Figure (4.2b) shows the reverse of the process depicted in figure (4.2a), namely the projection of rays back towards their point of origin, which is the fundamental principle of back projection. Mathematically, this is achieved by making use of the Radon transform, such that the spatial distribution of the density in the computed reconstruction is proportional to the density of the sample [131].

One of the primary disadvantages of back projection is that simply projecting the images backwards without filtering or weighting results in a blurred reconstruction. Figure (4.3) shows two identical spherical phantoms, or virtual test data, used to test electron microscopy techniques, of uniform density which have been reconstructed using unfiltered and filtered back projection methods respectively. From the figure it is clear that the reconstruction produced by filtered back projection, shown in figure (4.3b) closely matches a uniformly dense solid sphere, while the reconstruction produced by unfiltered back projection, shown in figure (4.3a),

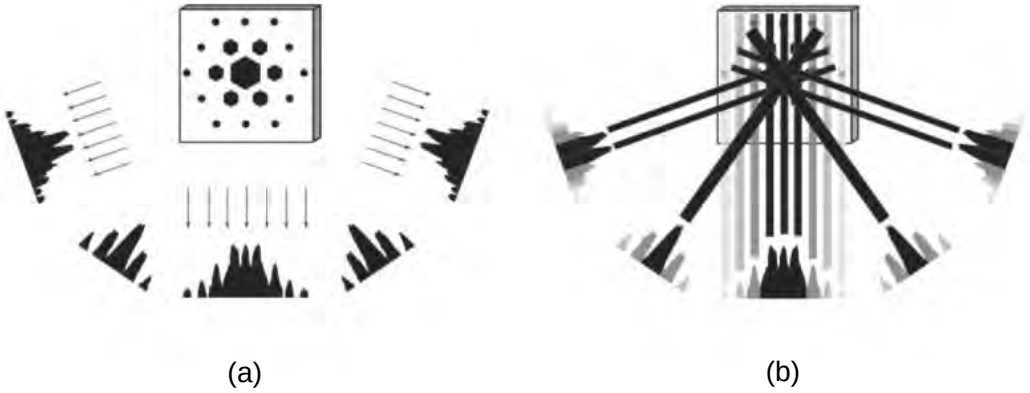

Figure 4.2: Schematic representation of the principle of Back Projection in electron tomography [132]. (a) forward projection of a structure in different directions to form a set of images. (b) back projection of features in the images to reconstruct the structure.

appears to correspond to a sphere with density which decreases radially outwards from the centre of the sphere, resulting in the reconstruction appearing blurred. This blurring effect comes from the overlapping of the Fourier-transformed tilt series images around the low frequency region. To control these effects, a ramp filter, corresponding to $|x|$ in Fourier space, is applied during reconstruction [133]. The purpose of the filtering (or weighting) in the improved back projection scheme is to modify the source images, prior to back projection, in such a way so as to remove or, at the very least minimise, the blurring effect inherent to unfiltered reconstruction algorithms, depicted in figure (4.3a) [134]. All reconstructions presented in this thesis were created using weighted back projection.

The two reconstruction methods presented thus far may be grouped into the single category of real space reconstruction, as the three dimensional model is created in real space. In addition to real space reconstruction algorithms there also exist Fourier space reconstruction algorithms in which the three dimensional recon-

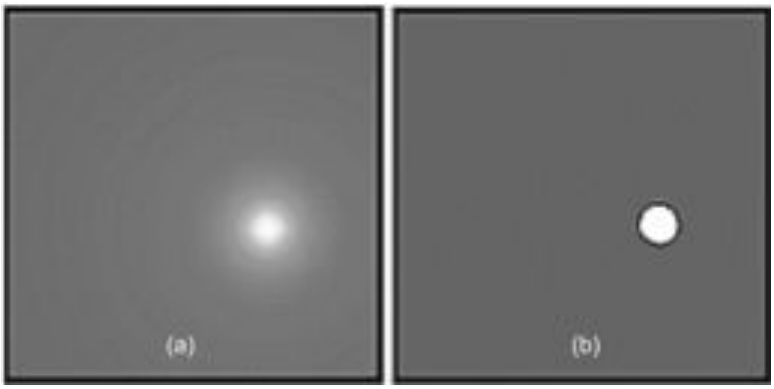

Figure 4.3: Visualisation of the differences between the unfiltered (a) and filtered (b) back projection [132].

structions are first created in Fourier space before being converted to the desired reconstruction in real space.

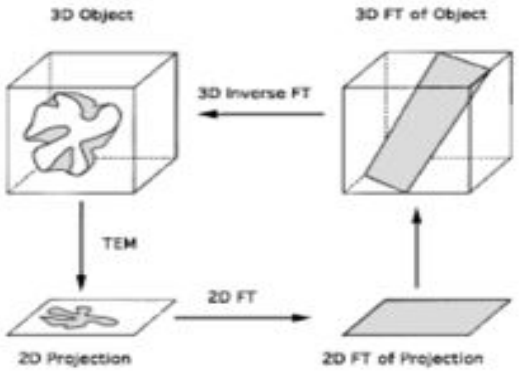

Figure 4.4: Schematic representation of the principle of Fourier space reconstruction in electron tomography [135].

Figure (4.4) depicts the process of Fourier space reconstruction schematically. The four subfigures illustrate the various stages which are required in order create the reconstruction, while the black arrows illustrate the flow of the process. The process begins with the physical sample to be reconstructed. The next stage involves the acquisition of a single projection image. This image is then transformed into Fourier space using numerical Fourier Transform (FT) techniques. The process

continues with the rotation of the transformed projection image by the angle of acquisition, after which it is inserted into a three dimensional model in Fourier space, termed the Fourier model. Once this process has been completed for all projection images, the real space reconstruction is recovered by applying the inverse Fourier transformation to the Fourier-space model.

These Fourier space methods are made possible by the central section theorem which states that, in the case of a two dimensional reconstruction from one dimensional images, the Fourier transform of a one dimensional projection is mathematically equivalent to a section at the same angle through the centre of the two dimensional Fourier transform of the object. This concept has been extended to three dimensions and, more recently, generalised to n dimensions [136].

4.1.1 Practical Limitations on Electron Tomography (ET)

Practical limitations, such as the angular acquisition range, which are limited by the physical geometry of the microscope stage hardware result in the inability to create reconstructions without artefacts. The most common artefact is known as the missing wedge, which is most easily explained in the context of Fourier space reconstruction. As not all projection angles are attainable, each missing image corresponding to a projection angle leaves an empty plane in the Fourier space model. As such, many missing projection angles result in many missing planes and, in the case of a single axis tomographic experiment, the region not covered in Fourier space has the shape of a wedge. The effect of the missing wedge is such that the Fourier space model, when converted to real space, results in both a blurring of the reconstruction, as a result of missing information, and as resolution anisotropy along the z axis relative to the x, y axes.

Consider an acquired tilt series with an angular range of -50° to 50° and a resolution of 1nm in the tilt series images with a size of 1024×1024 pixels and a total of 500 images. The resolution of the tomogram in the image plane parallel to the tilt axis, d_x, is set by the lateral resolution of the input images used for

the reconstruction. According to the Crowther criterion [137], the in-plane tomogram resolution, d_y in the image plane, perpendicular to the tilt axis, is described by

$$d_y = \pi \cdot \frac{D}{N}, \tag{4.1}$$

where D is the thickness of the sample, and N is the number of projections used to create the tomogram. The tomogram resolution along the axis perpendicular to the image plane, d_z, is given by

$$d_z = d_y \cdot e_{yz}, \tag{4.2}$$

where e_{yz}, known as the elongation factor, is defined as [137]

$$e_{yz} = \sqrt{\frac{\alpha + sin(\alpha) \cdot cos(\alpha)}{\alpha - sin(\alpha) \cdot cos(\alpha)}}, \tag{4.3}$$

where α is the absolute value of the maximum projection angle, in this case 50°.

From the TEM images presented in section 3.2.2, the primary clusters under study are known to have a mean long axis of approximately 120 nm. As a conservative first approximation to the thickness of the sample, which in this case corresponds to a collection of silicon nanoclusters that tend to lie flat on the sample grid, it is reasonable to assume a maximum sample thickness equal to the longest axis observed in two dimensions, 120 nm. Thus, according to equation (4.1) the resultant tomogram should have a minimum resolution of 0.75 nm per pixel along the axis perpendicular to the tilt axis in the image plane. This resolution is clearly much smaller than the resolution of the rescaled images used in tomogram construction, $1nm$ per pixel. Thus, the resolution of both axes in the image plane can be said to both have a pixel resolution of at least 1 nm, removing the anisotropy described in equation (4.1). Calculating the elongation factor, e_{yz}, for the tilt range used in

tomogram reconstruction from equation (4.3) yields a value of 1.8, which implies that features along the z axis will appear 1.8 times longer than they should.

4.2 A New Correlation Based Alignment Technique for Use in Electron Tomography

In this section a new correlation based method for the alignment of a single axis tilt series is presented. Rather than performing the pairwise correlation procedure with the central image as the starting point, the method presented here calculates the optimal starting position within the tilt series and proceeds towards both ends. The starting position is determined by maximisation of a viability function, J, which rewards cumulative series correlation and penalises both cumulative series shift and distance from the centre of the image series.

4.2.1 Overview of Alignment Methods for Electron Tomography

The alignment methods most frequently used in 3D microscopy may be broadly categorised into two groups, marker based alignment [138] and marker free alignment [139]. In the case of marker based alignment, fiducial markers are added to the specimen during sample preparation. The markers, often gold nanoparticles [140], are assumed to be immobile with respect to the sample and thus a change in position of the markers implies movement of the sample [141]. Alignment is produced by tracking the positions of markers and comparing their positions across many images in the tilt series [140, 127]. Methods have been developed which allow the fiducial marker alignment of an image series where not all marker positions need not be identified in every member of the tilt series [142], only that a minimum density of markers must be exceeded. If a pairwise method is employed features need only exist in neighbouring images.

Hybrid methods [143] also exist in which a global alignment is calculated from the positions of all fiducial markers within a sample, after which refinement is carried

out by dividing the tilt series images into segments, where a certain minimum number of fiducial markers is present in each segment, and then performing the marker based alignment again but on a local scale, thereby refining the global alignment[143].

Tracking the positions of the fiducial markers across a tilt series as well as ensuring correct correspondence between them is complex. However, several methods have been developed to automatically track the positions of the fiducial markers [144], which facilitate a more tractable analysis. Although fiducial marker based alignment produces consistent alignment throughout the entire tilt series [145], not every sample lends itself to the fiducial marker method. It may be difficult to produce a sample which contains the appropriate density of fiducial markers, and also, the colloidal gold particles, which are most frequently used, are often the most dense material present in the sample and may introduce artefacts into the reconstructed model.

The most popular alternative to the fiducial marker method is the correlation method [139], which uses a sliding inner product process to determine the similarity between two signals which are separated by a time lag. In image processing the two dimensional cross correlation function is used to locate the presence of a mask image within a second image, which is the basis for marker free alignment in electron tomography. When the cross correlation operation is applied to a pair of images the result is a two dimensional matrix whose elements are populated by the intensities of the correlation operation, or measures of similarity, between the two images at every point. Thus the x and y coordinates of the peak in the correlation matrix represent the number of pixels that one image must be shifted by in the x and y directions to be in alignment with the second image. In order to calculate the rotational shift between two images, one of the images is repeatedly rotated by an increasing known angle while the cross correlation function is applied to each of the rotated images and the second image in turn. This process is repeated until the correlation matrix with the highest intensity is found. The accuracy of aligning two images with each other using cross correlation techniques improves

with increasing similarity between the two images.

In electron tomography a pair of images may not be correlated directly without correcting for length distortion, an effect where the length of the image area perpendicular to the tilt axis is compressed at high tilt angle [146]. The effect of length distortion may be exacerbated by acquiring the tilt series far from the eucentric height of the microscope [147]. Coarse alignment is produced by applying the cross correlation function to successive neighbouring image pairs within the image series. As correlation based alignment techniques produce a cumulative error along the alignment path in the tilt series, the central image, often the zero plane image, is conventionally used as the starting point, or seed, of the alignment. Alignment produced by the correlation method may be further refined through an iterative process of aligning reprojections from successively refined reconstructions with their corresponding images within the acquired tilt series [148, 149]. As alignment is obtained from image pairs, the correlation method does not produce consistent global alignment. Rather, with the pairwise technique, alignment is heavily biased in favour of the alignment of the image used as the starting point. In addition, the ability to refine the alignment of a tilt series by the iterative reconstruction technique is hindered by the number and quality of the projections used for comparison with the tilt series images. Hybrid techniques have also been developed which aim to merge the marker based and marker free alignment schemes [139]. These methods work by identifying features in the sample images which are mathematically unique. The locations of these features are then tracked throughout the image series in a similar manner to fiducial markers. Although hybrid methods produce good alignment, they are not automatically applicable as they require a certain minimum number and density of calculated features to produce accurate alignment.

The choice of the central image position as the seed has become a de facto standard and is widely implemented in microscopy software [150, 151, 152]. This choice does not allow for the fact that the central image may be misaligned relative to the rest of the image series, which would tend to shift information near the centre of the

tomogram out of frame, resulting in information loss in the reconstructed model. It is also possible for another image in the tilt series to produce better overall alignment of that series, a possibility which is generally overlooked in favour of minimising cumulative alignment error.

4.2.2 The Viability Method of Alignment

The *viability alignment* method proposed here allows the user to align an image series by choosing a user-defined seed position or by allowing the alignment procedure to calculate the optimal seed position. To compensate for the cumulative alignment error the viability of positions far from the central region are heavily weighted as will be described below. Once the viability of each position in the image series as the seed has been determined, a pairwise, correlation based alignment is then performed, starting at the optimal seed position and moving outwards towards either end of the series. The result is a fully automatic, coarse alignment method which allows the alignment of an image series, even where the central region is badly misaligned, by starting the alignment at a position in the series determined in a quantifiable, repeatable manner. The optimal seed position is defined as the position in the image series that results in maximum cumulative correlation between all pairs of neighbouring images and minimum cumulative relative shift or rotation. Relative image shift, τ_τ, and rotation, τ_ρ, may be expressed mathematically as follows

$$\tau_\tau(i) \equiv \frac{s_x^i}{L_x^i} \cdot \frac{s_y^i}{L_y^i}, \tag{4.4}$$

and

$$\tau_\rho(i) \equiv \frac{\theta_i}{2\pi}, \tag{4.5}$$

where s_x^i, s_y^i are the translational alignment parameters and θ_i the rotational alignment parameter. L_x^i and L_y^i are the x and y dimensions of the i-th tilt series image.

In order to ensure that seed position candidates far from the centre of the series are heavily weighted a function is employed which treats all images in a user-definable central region as equal and increases, with a user definable sharpness, outside of this region. The penalty function, termed E, is defined as

$$E(i) \equiv \frac{(\Delta i)^2}{L^m \sin^2\left(\frac{\pi \Delta i}{L}\right)}, \tag{4.6}$$

where L is the length of the central region, $m = 1, 2$ and controls the slope of the function outside of the central region. Δi is the distance from position i to the centre of the series. To measure the similarity between consecutive image pairs, the cross correlation function is used as a figure of merit and is defined as

$$ccfn_x(n) = \frac{\frac{1}{n_x}\sum_{k=0}^{n_x-1}(f((k+n+n_x)mod(n_x)) - Ave_f)(g(k) - Ave_g)}{\sigma_f \cdot \sigma_g}, \tag{4.7}$$

where f denotes an image, g the reference image, n_x is the size of the square image and σ_f, σ_g are the standard deviations of the pixel values from images f and g respectively. The variable n is defined as: $n = -\frac{n_x}{2}, ..., +\frac{n_x}{2}$ and Ave_f, Ave_g are the average pixel values of images f, g. The seed position viability function, J, is then constructed as follows:

$$J(i) \equiv \sum_{i=seed}^{N} \frac{\frac{\max(ccf(T_{i+1},T_i))}{L_x L_y}}{|\tau_{\tau,\rho}(i)| \cdot E(i)} + \sum_{i=seed}^{0} \frac{\frac{\max(ccf(T_{i-1},T_i))}{L_x L_y}}{|\tau_{\tau,\rho}(i)| \cdot E(i)}, \tag{4.8}$$

where $\tau_{\tau,\rho}$ refers to either τ_τ or $\tau\rho$ from equations (4.4, 4.5) when dealing with translational or rotational alignment respectively. The viability function numerator is constructed in such a way so as to increase J with increasing normalised circulant cross correlation between every two pairs of images. Thus, the higher the sum of the peaks of the correlation matrices between every two image pairs, starting at position i, the more viable position i is as the seed. This on its own is insufficient, as it is possible that alignment performed with a badly misaligned

image position as the seed would cause features to be translated or rotated out of the image series once aligned.

The denominator of the viability function is constructed to be a series of penalties on the viability of position i in the image series as the seed position used for alignment. The sum of the peaks of all correlation matrices are divided by their translational or rotational alignment parameters. Thus the viability of position i as the seed position increases with decreasing cumulative shift or rotation used to produce alignment, thereby decreasing the likelihood of choosing a seed position corresponding to a badly misaligned image.

Aligning the tilt series with respect to successive images in the series exhaustively, J is calculated for every possible seed position. Pairwise alignment is then started at the seed position corresponding to the highest value of J.

It is also worth noting that the hybrid methods mentioned previously [139] may be applied to the viability method presented here. In this case mathematically unique features could be extracted as markers from the projection images and alignment produced by tracking and correlating the positions of these features throughout the image series. Unfortunately, these extracted features do not often exist in sufficient density between neighbouring image pairs, and are not automatically applicable to samples investigated by electron tomography owing to factors such as sample size, density and thickness [139].

4.2.3 Testing the Alignment Methods with Simulated Data

To test the alignment procedures a model comprised of a set of differently sized cuboids, each having a quasi-random voxel intensity was created as shown in figure (4.5). The random voxel intensity, within well-defined bounds, creates both fine and coarse structure in the synthesized volume to allow a verification of the original pattern at every level of resolution.

The purpose of employing randomly distributed cuboids was to ensure that the volume, when considered as a whole, would be free of translational and rotational

symmetry even though individual the elements in the volume possess symmetry. Hence all projections calculated would better represent data collected from a heterogeneous sample. From this model an image series was projected corresponding to a single-axis tilt of $[-60°, 60°]$ with a step of $2°$. This phantom image series was then used as a reference to create two image series, for testing the translational and rotational correction algorithms, each with severe alignment errors introduced.

A random translation error of 25%, centered about zero, was applied to each image of the model image series, yielding the translation test data shown in part in figure (4.6a). These data were used to reconstruct the volume as shown in figure (4.7a). The effect of the translational misalignment is clear as almost no detail of either the shape or distribution of the cuboids is visible when compared to the reference model shown in figure (4.5). A random rotational error of $15°$, centered around $0°$ was also introduced as shown in figure (4.8a), with the reconstruction shown in figure (4.9). The rotational misalignment was applied using the image rotation subroutines present in SPARX [151].

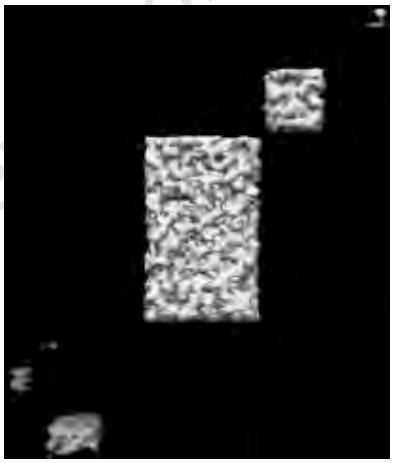

Figure 4.5: Front view of the synthesized reference volume, in the form of six cuboids, which serves as a base of comparison for both the translational and rotational alignment methods.

After applying the translation correction algorithm to the misaligned images of

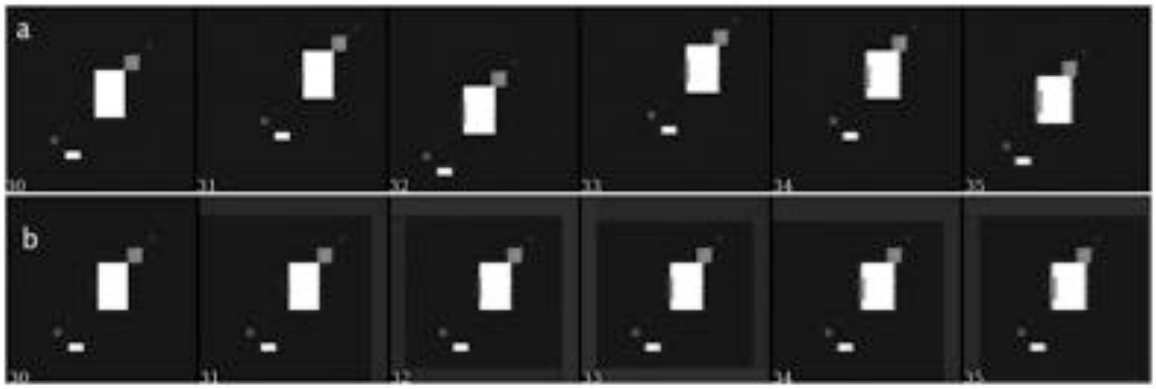

Figure 4.6: Six image subset of a single-axis test series with translation error introduced. The subset depicts projections 30 to 35 out of 60, corresponding to a tilt of 0° to 10° in steps of 2°. The leftmost image in the series is the zero-plane image. The second row depicts the same subset post alignment.

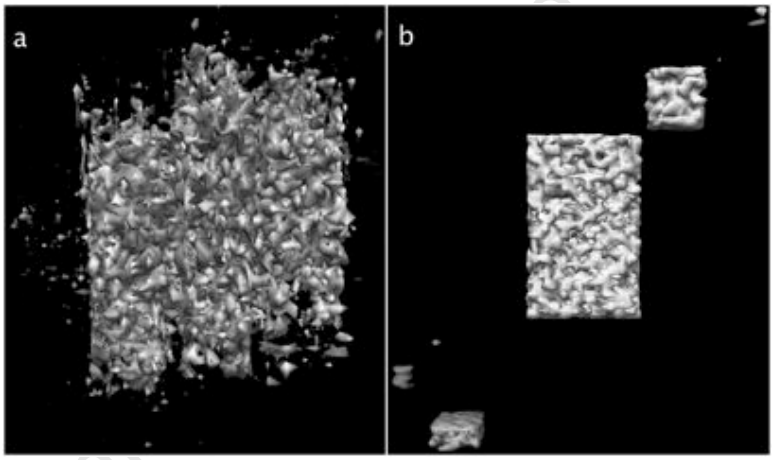

Figure 4.7: Three dimensional reconstructions of the synthesised data. On the left, a reconstruction performed on the misaligned image series. On the right, a reconstruction performed on the translationally aligned series.

the model image-series, the reconstruction, as shown in figure (4.7b), is much improved to yield a satisfactory result. Comparing the model volume shown in figure (4.5) with the translation corrected reconstructed volume shown in figure (4.7b), not only are the distributions and locations of the cuboids preserved but also their shape and even the surface structure of the individual objects closely

match. The basis of the high quality of the reconstruction lies in the quality of aligning the individual images to a seed position chosen by the translation correction algorithm.

Figure (4.6b) shows the same consecutive projections, numbered 30 to 35, as in figure (4.6a), but after the translation correction was applied to the misaligned single-axis tilt-series, with the zero-plane image, image 30, used as the seed image in the alignment. By comparing the individual images it is easy to see that the various projections are correctly aligned with each other. The grey bars visible at the borders of the aligned images illustrate the translational shifts, relative to the seed image, applied to those images which demonstrates that even large errors are corrected satisfactorily.

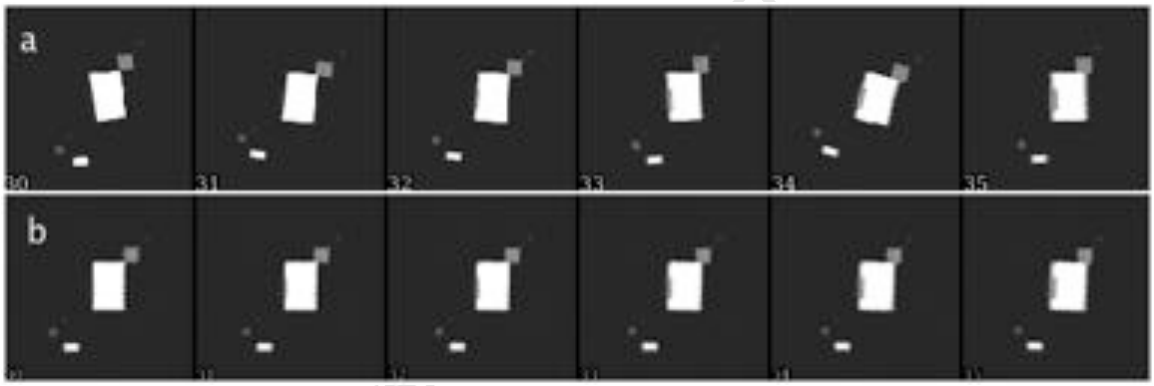

Figure 4.8: Subset of six images of the single-axis test series. Row a shows the synthesised test data with rotation error introduced. Row b depicts the same subset of images post alignment, with image 37 used as the seed.

After applying the rotational alignment correction, the dataset depicted in figure (4.8b) was obtained as well as the reconstructions depicted in figure (4.10). As can be seen from the reconstructions, the projection images are reasonably well aligned with respect to each other. Comparing the reconstructions in figure (4.10) shows the usefulness of the seed image approach as altering nothing but the starting point of the alignment adds significant information to the reconstruction. The effect of the accumulated alignment error is visible in figure (4.10 b) as the top edge of the large central cuboid is no longer horizontal as in the reference volume. Figure

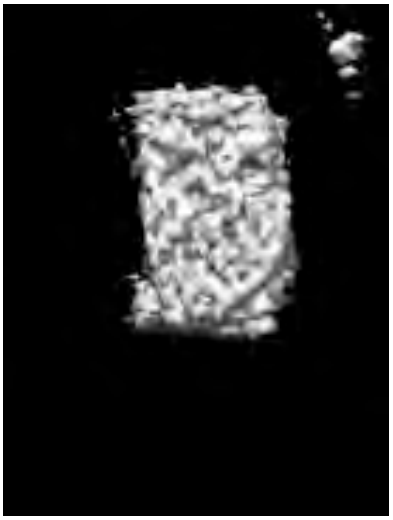

Figure 4.9: Three dimensional reconstruction of the rotated dataset. Some structure is still visible even after rotational misalignment when compared to the reference model shown in figure (4.5).

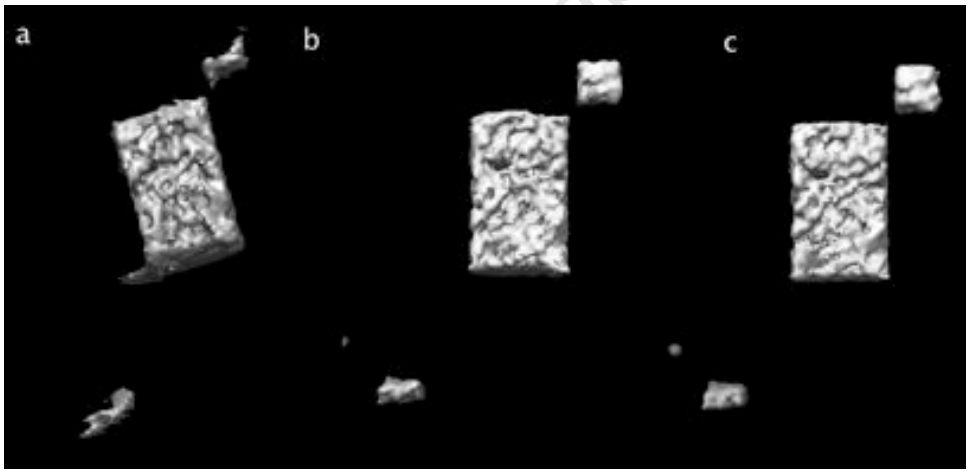

Figure 4.10: Three dimensional reconstructions of the rotation corrected image-series. Left, using the zero-plane image as the seed; centre, using image 27 as the seed; right, using the seed position corresponding to the maximum value of J, image 37, as the seed.

(4.10 c) illustrates the effect of maximising the viability function to determine the alignment seed position. The top edge of the central cuboid is closer to horizontal

and, in general, the larger structures appear to more closely match the reference volume shown in figure(4.5)

On comparison of figure (4.10) with figure (4.5) it is clear that the rotational alignment is not perfect. The coarse structure of the larger cuboids is mostly preserved, however, the small cuboid located at the upper right hand side of the reference volume is missing, as is the single-point element at the lower left hand corner. The fine structure present in the reference volume is also affected but is still reflected in the rotation corrected reconstruction. This incomplete alignment and loss of data stems from the image distortion introduced by digital rotation.

As the misalignment introduced into the test data is known, residuals which provide a goodness-of-alignment score for both the translational and rotational alignment procedures may be defined. In both cases the metrics are defined as the square root of the sum of squares of the differences between calculated image alignment parameters and known introduced misalignment parameters. The translational residual metric, R_τ, is defined as

$$R_\tau \equiv \sum_{i=0}^{N} \sqrt{\left(s_x^i - \rho_x^i\right)^2 + \left(s_y^i - \rho_y^i\right)^2}, \tag{4.9}$$

where N is the size of the image series, s_x^i and s_y^i are the calculated translation parameters for the i-th series image and ρ_x^i and ρ_y^i are the known image shifts introduced to the reference series. The rotational residual metric, R_ρ, is defined similarly as,

$$R_\rho \equiv \sum_{i=0}^{N} \sqrt{\left(s_\alpha^i - \rho_\alpha^i\right)^2}, \tag{4.10}$$

where N is the size of the image series, s_α^i is the calculated rotation parameter for the i-th series image and ρ_α^i is the known image shift introduced to the i-th image in the reference series. Thus, the lower the residual score, the better the quality of alignment. Figures (4.11a) and (4.11b) depict visualisations of R_τ and J with

respect to seed image position for the test data presented in figure (4.6). From figure (4.11a) it can be confirmed that the seed image position which produced the best overall alignment to the randomly misaligned image series was image 30, the zero plane image. From figure (4.11b) it can be confirmed that the maximum value of J does indeed correspond to the seed image position that resulted in the lowest translational residual score.

Figures (4.12a) and (4.12b) depict visualisations of R_ρ and J with respect to seed image position for the rotational alignment test data presented in figure (4.8). From figure (4.12a) the seed image position which produced the best overall alignment to the randomly misaligned image series was image 37, not the zero plane image. From figure (4.12b) it can be seen that the maximum value of J does indeed correspond to the seed image position that resulted in the lowest rotational residual score. It is worth noting that the large scatter observed in figures (4.11a, b) and (4.12a,b) is as a result of the large randomly assigned misalignments which, in turn, produce large random scatter in the figures. It is also worth noting that, as the relationship between neighbouring J values is complex, the form of the visualisation of the J function is arbitrary. To investigate the performance of the viability method under conditions of noise, per-pixel zero-mean Gaussian noise with standard deviation, in colour value, of $32, 64$ and 128 was added to the test data shown in figure (4.6) to create three new image series. As the test data shown in figure (4.6) has an average mean pixel value of 33 and standard deviation of 45, the noise levels chosen correspond to medium, high and very high levels of noise. These three image series were then aligned with the viability method and the series sum of the J values from each new series was plotted as a function of image noise in figure (4.13a).

Finally, pairwise correlation-based alignment methods in general require that the images within all correlated image pairs must be similar. Should these images differ by a significant amount, the correlation operation and the resulting image alignment may be poor. To maximise similarity between images within an image series, one may acquire the images with a small tilt angle increment. In this way,

each successive image is tilted only slightly when compared to its neighbours. To test the effect of tilt angle increment on the function J, the test data shown in figure (4.6) was reprojected with tilt angle increments of $1, 2$ and 5 degrees. Figure (4.13b) shows the series sum of the J function for the alignment produced from the reprojections. From this it can be deduced that, while the quality of alignment decreases with increasing tilt angle increment, good alignment is still obtained with a tilt angle increment of $5°$. In addition a similar quality of alignment is obtained from a low noise sample with a $2°$ angular increment as is obtained from a medium noise sample with a tilt angle increment of $5°$. The alignments presented here are produced from unfiltered images. Image filtering, often bandpass filtering, is used in correlation based alignment techniques to improve the accuracy of the cross correlation operation by reducing the noise levels in the projection images, while retaining as much signal data as possible. This improved signal-to-noise ratio, which often results in superior displacement calculations, is obtained at the expense of image data that are often lost in the high frequency domain.

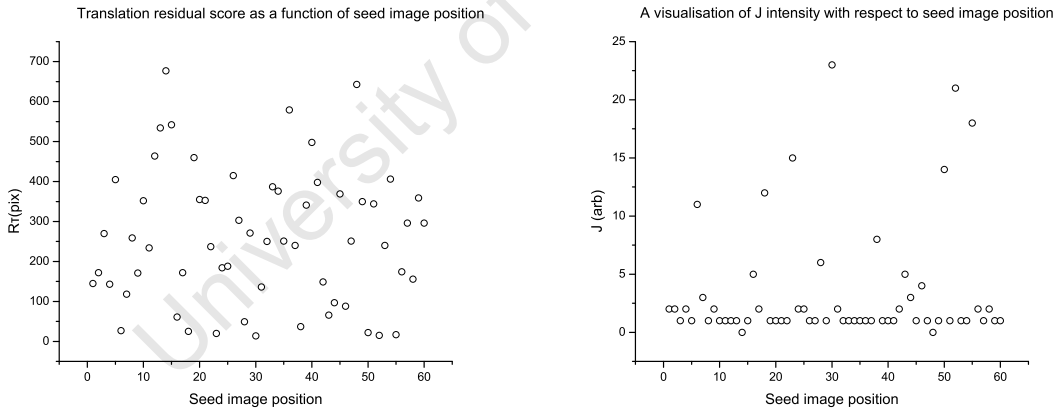

(a) (b)

Figure 4.11: Residual scores and J intensity values for the translation corrected test data presented in figure (4.6b). (a), Visualisation of the residuals produced by the translational alignment. (b), The intensity of the J function produced by the translational alignment.

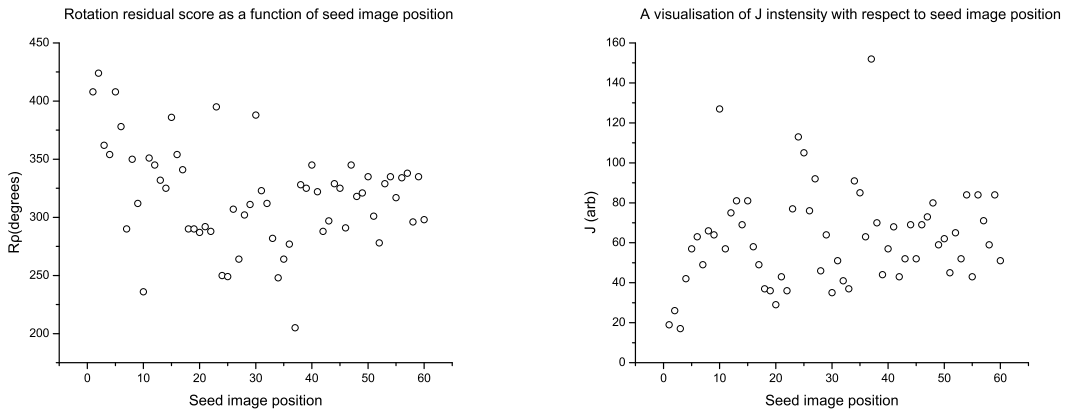

(a) (b)

Figure 4.12: Residual scores and J intensity values for the rotation corrected test data presented in figure (4.8b). (a), The residuals produced by the rotational alignment. (b), The intensity of the J function produced by the rotational alignment.

Table (4.1) shows the processor time required, on a personal computer equipped with an Intel core i7 processor, with a clock speed of 2.2 GHz, to produce alignment as well as the memory requirements of the alignment procedures for the synthetic test data. The times displayed in the table are the total times taken to produce alignment of all 60 images. As all positions in the series are tested for viability, the computational requirement of the algorithm is $O(N^2)$ with respect to the number of images in the series. Thus, if the number of images in the series is doubled, the time taken to produce alignment will increase by a factor of four. The software has been tested with data sets up to 700 images and produces alignment in a few hours. Although this is comparatively slow with respect to other alignment methods, reconstruction techniques and data acquisition of such large data sets are inherently time consuming processes, which are not badly effected by the increased time required by the viability method to produce alignment. Should faster computational times be required, the series images may be re-binned to produce images of smaller size, which greatly reduces the computation time required align

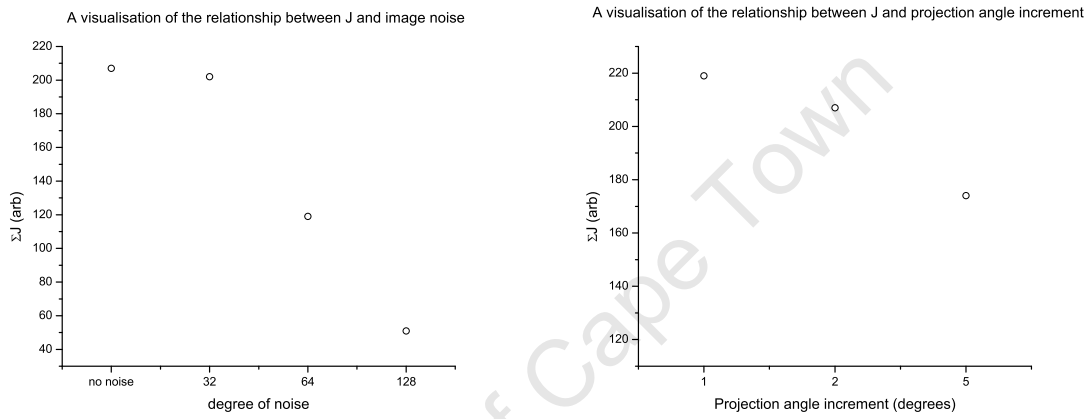

(a) (b)

Figure 4.13: Visualisation of the relationships between the viability function, J, and image noise as well as projection angle increment. (a), Relationship between the series-accumulated J values and image noise for the test data derived from figure (4.6). (b), The relationship between the series-accumulated J values and projection angle step size for the test data derived from figure (4.6), reprojected with angular spacings of $1, 2$ and 5 degrees.

the images.

Alignment type	time (s)	$\delta_{time}(s)$	RAM (MB)	$\delta_{RAM}(MB)$
translational	219	20	42	7.7
rotational	653	31	50	9.2

Table 4.1: Completion times and memory usage for the alignments shown in figures (4.6) and (4.8).

4.2.4 Testing the Alignment Methods with Experimental Data

To test the alignment algorithms a single-axis tilt series of images was taken of silicon nanoparticles dispersed on a TEM grid after sonication in ethanol. These nanoparticles form stable aggregates [8], rendering them a good candidate for the procedure as there is no global symmetry within the sample to be exploited. A sample subset of the tilt-series is shown in figure (4.14).

The tilt-series was acquired on a Tecnai T20 TEM using the UCSF Tomo and Leginon software packages [153]. The data was acquired with a beam voltage of 200KV and a magnification factor of 10,000X. The angular range of the acquisition was $[-50°, 50°]$ with a step of $0.2°$.

Due to the accuracy of the T20, the rotational shifts in the dataset were negligible and rotation correction was unnecessary. Figure (4.15) shows the viability of each position in the image series as the seed for the alignment. As can be seen from the figure, the central image, image 250, is the least optimal starting point for the alignment, while image 347 has been determined to be optimal, within the parameters defined in equation (4.8). A subset of the viability corrected dataset is shown in figure (4.16).

Figure (4.17) shows the reconstructions of the uncorrected data (a), conventionally aligned data (b) and the viability aligned data (c) in frames $1, 2$ and 3 respectively. Close examination of (b) and (c) reveal the alignment differences between the two

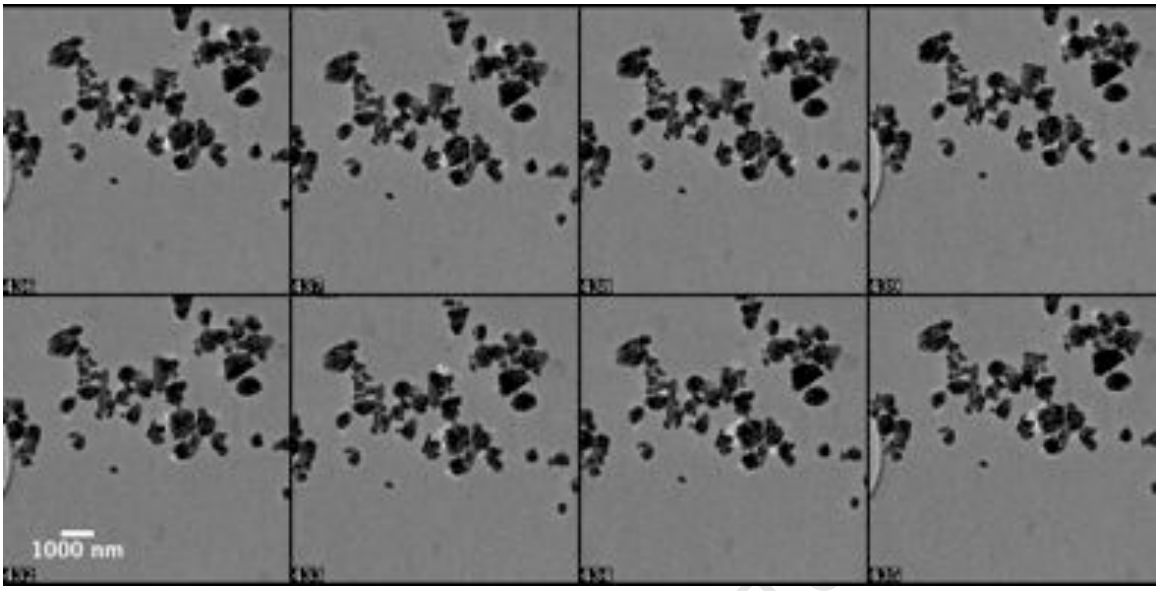

Figure 4.14: Sample subset of a tilt-series of nano silicon. The subset depicts projections 432 to 439 out of 500, corresponding to a tilt of $-43.2°$ to $-43.6°$ in steps of $0.2°$. Each nanoparticle is unique and, in general, the particles form large clusters.

methods. While most of the data appears in both reconstructions, the reconstruction presented in frame 3 more closely resembles the experimental data, pictured in figure (4.14) than does the reconstruction presented in frame 2. The reconstruction presented in frame 3 also appears sharper, with more of the fine details being preserved than in the conventionally aligned data set, presented in frame 2 when compared to the acquired image series subset in figure (4.14).

4.2.5 Application of the Viability Method to Dense Samples

The alignment techniques introduced here offer an alternative to feature based correlation methods [139] and extend the functionality of existing pairwise correlation methods [154] especially in cases where the input tilt series is badly misaligned relative to the sample coordinate system near the central region. When the central region is badly misaligned the method of penalties and viability proposed here

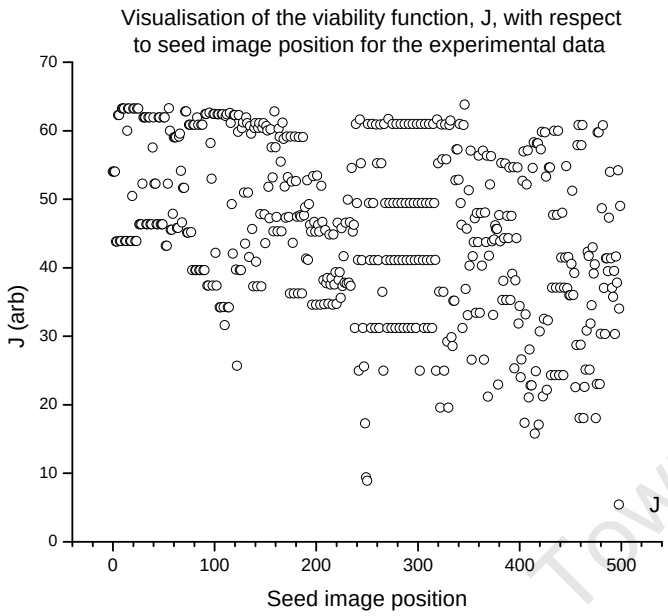

Figure 4.15: Visualisation of the viability function, J as a function of seed image position for the experimental data presented in figure (4.14). As can be seen from the figure, the seed image position corresponding to the maximum value of J is 347.

allows for the selection of a new starting point for the pairwise alignment. Even in cases where the central region is not badly misaligned, the proposed methods often calculate an image other than the central image as the seed. In these cases alignment is improved by a few pixels, however the overall alignment is more consistent as the method produces an aligned tilt series which preserves, on average, image data close to the centre of the series images. This in turn produces reconstructions which contain the maximum amount of pixel data from all images in the series.

The robustness of the technique against poor misalignment of the central series image is particularly important for dense samples, such as metal oxide particles, chalcogenides and the silicon nanoparticles under investigation here, which are particularly susceptible to central image misalignment during the automatic data

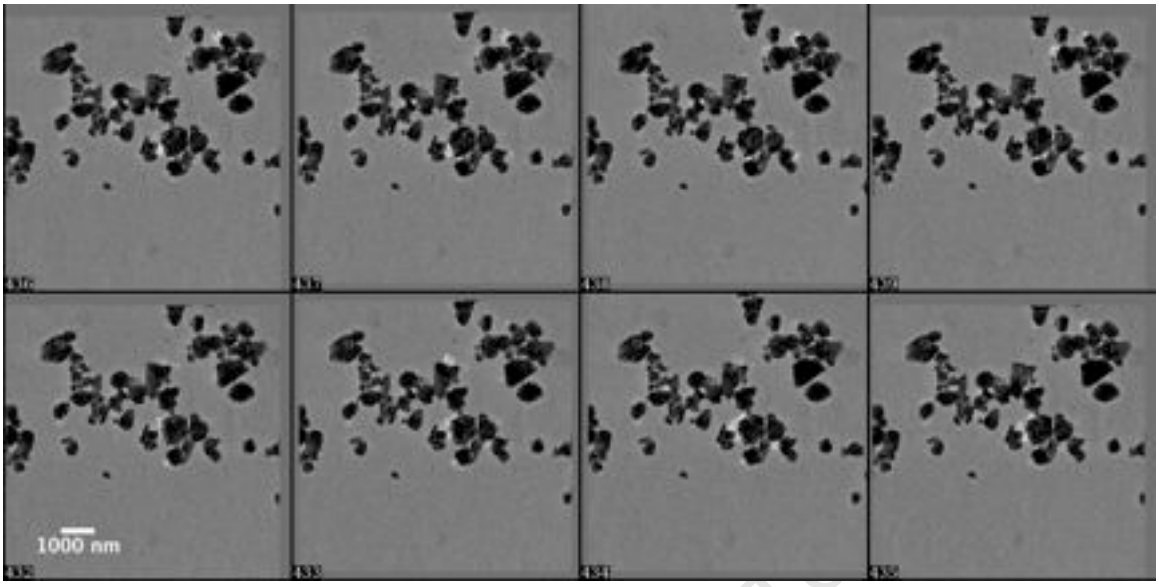

Figure 4.16: The sample subset, depicted in figure (4.14), after the viability translation correction algorithm was applied, using image number 347 as the seed.

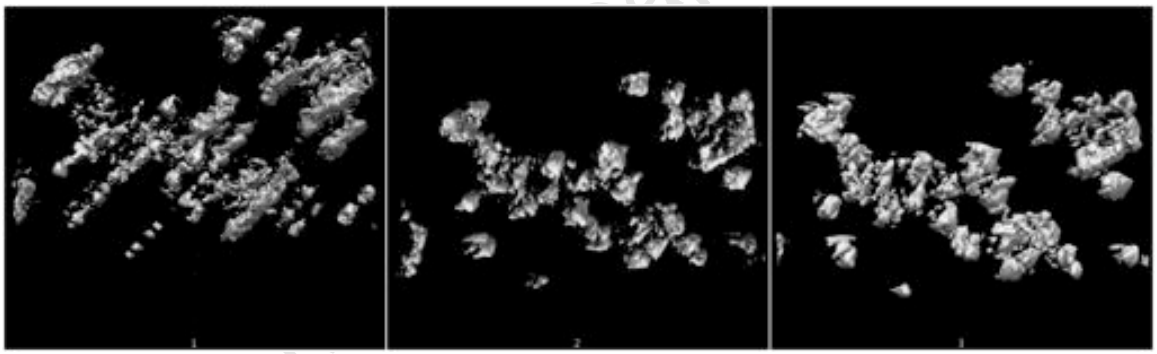

Figure 4.17: Reconstructions of the real data. On the left is the uncorrected data, in the centre is the aligned data using the central image as the seed and on the right is the alignment produced with the seed image position corresponding to the highest value of J, image 347.

acquisition processes, described previously. The misalignment stems from the fact that the central image is not the first image collected in the series. Conventionally, the central image is collected midway through the acquisition process as the software begins acquisition at the image with the largest negative tilt angle. Given

that the data acquisition software must reposition the TEM grid prior to the acquisition of each image and that correlation methods are used to achieve this, the same cumulative alignment error which effects correlation based pairwise alignment is also a problem during the data acquisition phase, which often results in misalignment of the central image.

The marker-free approach of the alignment technique is also well-suited to dense samples as there may be insufficient visible fiducial markers, owing to occlusion of the markers by the dense sample material, available with which to produce tilt series alignment. Similarly, hybrid techniques which make use of generated mathematical landmarks, which are in principle similar to fiducial markers, may also perform worse when applied to dense sample materials. Finally, in the case of dense semiconducting samples, the beam-sample charging effects, described previously, are also able to interfere with or corrupt both mathematically generated landmarks as well as the appearance of fiducial markers.

4.3 Phantom Statistical (PhaST) - A Software Tool for the Creation of Three Dimensional Phantom Data in Electron Microscopy

In this section a new computer software package designed to facilitate the creation of synthetic volumetric test data, also known as phantom data, for use in electron microscopy, is presented. In electron microscopy, phantom data is defined as an artificially generated data set, specifically designed to test one or more electron microscopy methods. As various methods are better suited to either a particular sample type or method of sample preparation, it is often necessary to synthesise a known data set to test the various three dimensional electron microscopy (3DEM) methods and deduce which is most appropriate for the experimental setup at hand. Phantom data is also used extensively in the development of both new software techniques as well as with existing software which has been modified for a particular experiment. For example, in section 4.2 phantom data, in the form of cuboid test

structures, was used to test the alignment produced by the viability method when compared to the standard correlation based alignment technique. As the data was synthesised, it was possible to deliberately introduce known alignment errors and compare the alignment results to the known introduced misalignment.

Creation of phantom data is typically a two stage process. The first stage of the process involves creating a three dimensional model which corresponds to a virtual sample with properties specified by the user. The second stage revolves around projecting images from this model corresponding to the angular tilts and rotations specified by the user. The user is then able to use both the synthesised model as well as projections in order to test experimental methods. In three dimensional electron microscopy, the purpose of a phantom creation software package is therefore both to create the virtual sample model as well as arbitrary projections, which correspond to virtual acquired micrographs. These images may then have various errors applied to them, the most common of which are in plane shifts and rotations of the images themselves, which aids in the testing of alignment techniques, as well as the application of a random uncertainty to the pixel colour values of the images, which reproduces the grainy background effect often observed in micrographs, in order to test the response of a method to varying levels of noise present in real micrographs.

To date there exist relatively few tools which focus specifically on the creation of phantom data for use in electron microscopy [155, 156, 151]. The tools which are currently widely available offer a core set of functionality, comprising the model and projection creation described above. These software tools differ in the manner in which the user interacts with the software. The tools initially created for this purpose were all primarily text based, requiring the user to produce a script containing the information of all objects to be included in the produced model as well as the information describing the desired projections to be created, which rendered the model creation process conceptually difficult to implement. This problem was later addressed by the addition of graphical tools which, while providing the same core functionality as their text based counterparts, allow the user to observe the

model currently under construction in real time by dragging primitive objects from a graphical list and then dropping the primitive objects into the three dimensional model, which allow for the rapid construction of detailed models.

The software packages mentioned above all assume the creation of a particular immutable model as their goal. As an example consider a script written for the XMIPP [156, 157, 158] text based phantom creation tool. An identical three dimensional model will be created each time the script is run because the script is unable to facilitate random effects in synthesised models. The same limitation applies to graphical tools such as Phan3D [155], rendering these tools ill suited to model samples which are known to be distributed in some way with a probability distribution function. As an example, if the user wanted to simulate a colloidal sample by a set of spheres, the user would have to manually place each sphere, of correct radius, into the model at the correct location in three dimensional space. This becomes frustrating when the number of spheres required is in the tens or hundreds. In contrast, the PhaST package developed for this work allows the user to create three dimensional models, from a set of three dimensional objects, whose parameters are able to be drawn from a list of distributions, in a manner described below. Thus the user gains the ability not just to create an exactly specified model, with each execution of the script file, but rather a model may be defined which is flexible within certain constraints, such that a slightly different model is produced with every execution of the identical script file.

4.3.1 Model Creation in the PhaST Software Package

As mentioned above, the PhaST tool makes use of script files in order to synthesise the three dimensional model, termed the model geometry file, from a set of three dimensional primitive objects, referred to as primitives, and from a list of distributions. Table (4.2) illustrates the list of supported primitive objects, while table (4.3) illustrates the list of distributions from which all parameters of the primitive objects may be drawn.

cuboid	x	y	z	ϕ	θ	ψ	l	b	h
ellipsoid	x	y	z	ϕ	θ	ψ	a	b	c
cylinder	x	y	z	ϕ	θ	ψ	l	r	
toroid	x	y	z	ϕ	θ	ψ	R	r	
cone	x	y	z	ϕ	θ	ψ	h	r	
sphere	x	y	z	r					
point	x	y	z						

Table 4.2: List of primitive types available for model creation and the parameters required. See text for definitions.

In table (4.2) x, y, z are the coordinates for the centre of the element, ϕ, θ, ψ are the euclidian angles corresponding to element rotation, l corresponds to length, b to breadth and h to height. The cylindrical radial parameter is r and a, b, and c are the three principal axes of an ellipsoid. For the toroid, R and r correspond to the outer and inner radii respectively. In the case of the cone h and r are the perpendicular height and base radius. For the sphere, r is the radius.

normal (Gaussian)	GSS	μ	σ
log-normal	LGS	μ	σ
weibull	WEI	λ	κ
uniform	UNI	α	β
absolute	ABS	C	

Table 4.3: List of distributions and the parameters required for model creation and projection. See text for definitions.

In table (4.3) μ is the mean, σ the standard deviation of the mean, λ the scale factor, κ the shape factor, α the left bound and β the right bound and C an integer constant.

One of the most common problems encountered during statistical modelling is that of the boundary. When drawing random numbers from distributions the

package must enforce boundary constraints. There are a number of examples of this phenomenon within the software, all of which are treated in the same manner, namely truncation. As an example, if a Gaussian error is applied to a projection image, it is possible that the value generated may fall out of the range of valid pixel colour values, such as below 0 or above 255. In these cases the pixel values are set to 0 and 255 respectively. Another example would be a set of spheres in which x, y and z coordinates have been drawn from a Weibull distribution. Should the mean of this distribution be of the order of the total size of the volume, many of these spheres would appear only partially, if at all, in the rendered model. In these cases as well, the model is simply truncated, or cut to fit, the volume specified by the user in the model geometry file.

The model geometry file consists of a set of commands which the phantom creation software interprets and converts into a three dimensional model. All primitives, drawn from the list shown in table (4.2), which are included in the model geometry file must conform to the following grammar:

Number	Primitive Type	Location	Orientation	Structure

where Number refers to the quantity of objects to be added to the scene, Primitive Type refers to one of the element types defined in table (4.2), Location refers to the x,y and z coordinates of the centre of the object, Orientation refers to the three Euler angles, ϕ, θ, ψ, of the primitive, and Structure represents the size parameters which describe the primitive, according to the definitions in table (4.2).

The Number, Location, Orientation and Structure parameters must be drawn from the distribution pool defined in table (4.3). Distribution names are all three letters long and are related obviously to the distributions to which they refer. The normal distribution is termed GSS, log-normal is referred to as LGS, Weibull becomes WEI, the uniform distribution is designated the contraction UNI and the constant value flat distribution is termed ABS. A sample model geometry file, used to create the model depicted in figures (4.19 a) and (4.19 b), is shown in figure (4.18).

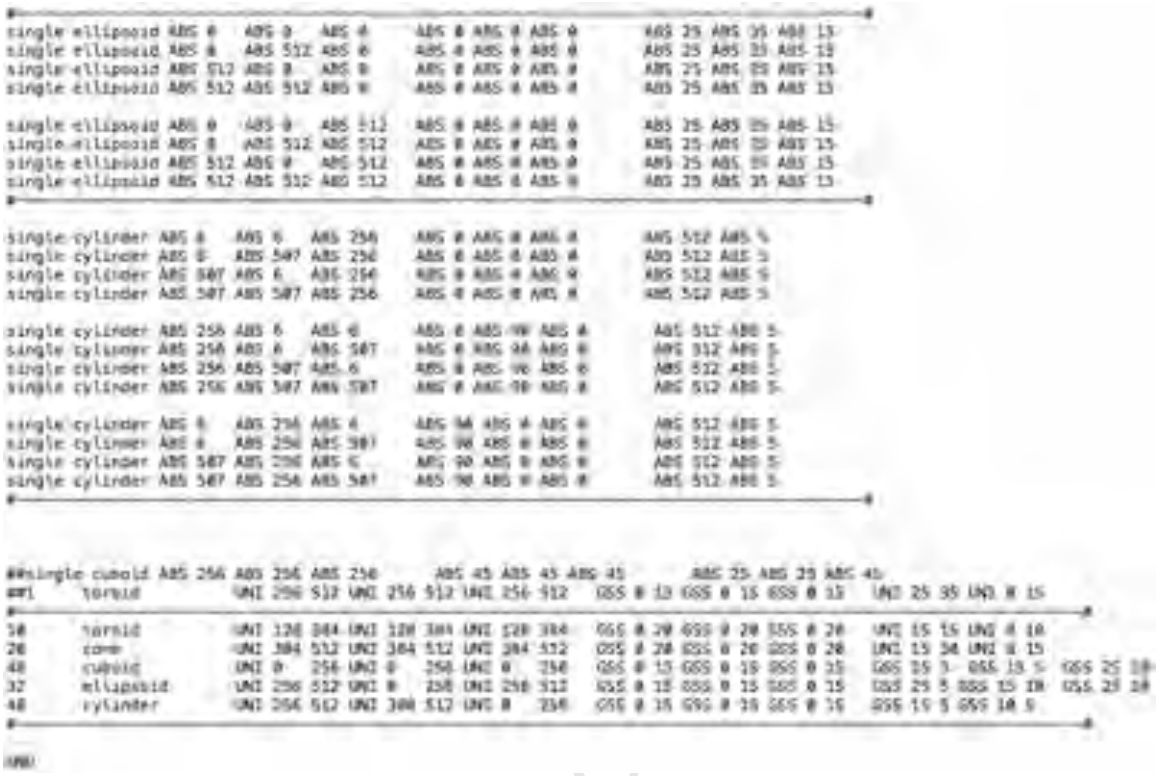

Figure 4.18: An example input file, used to generate the volume shown in figure (4.19 a,b)

Each line of the script file shown in figure (4.18) conforms to the model creation syntax defined above. The second line of the figure depicts the creation of a single ellipsoid, located at the bottom left corner of the model, with all three rotation angles equal to 0° and the three axial lengths taking on the values of 25, 35 and 15 pixels respectively. When all lines of the script were executed by the PhaST package, the model depicted in figures (4.19 a) and (4.19 b) was produced. As the locations of the 48 cylinders are drawn from a uniform distribution, as depicted in the script file on the fourth line from the bottom, should the script have been executed a second time, the positions of the 48 newly created cylinders would not correspond to the locations of the cylinders depicted in figures (4.19 a) and (4.19 b). The model depicted in figure (4.19), represents a nanocluster composed of 64 ellipsoids, whose parameters are drawn from various distributions. Should a

second similar, but not identical, nanocluster be required in the future, the model geometry script file would simply be executed a second time, without the need to redefine the parameters of the model.

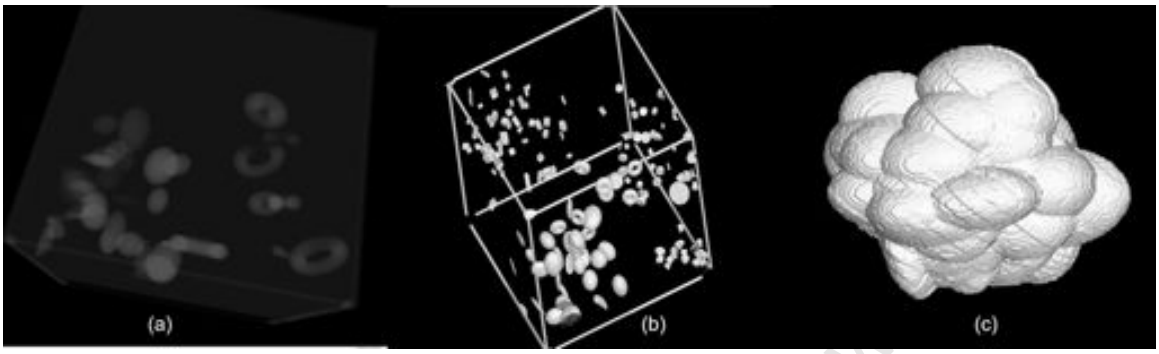

Figure 4.19: (a) a density view of the model, described by the script depicted in figure (4.18), comprised of 48 cuboids, 48 cylinders, 10 tori, 20 cones and 32 ellipsoids. The positions of all objects follow the uniform distribution, while the orientations and spatial parameters of all objects are drawn from a Gaussian distribution. (b), the solid view of the model in (a). (c), a modelled nanocluster composed of 64 ellipsoids, with uniform distributions across the three principal axes and a Gaussian distribution for the spatial coordinates.

4.3.2 Projection Creation in the PhaST Software Package

Once the volume has been created it may then be projected to form an n-axis tilt-series corresponding to a tilt-series acquired by an electron microscope. The created tilt-series may then have a wide range of errors introduced to simulate errors typically encountered during data acquisition, such as in plane shift and rotation of the sample as well as per pixel noise. The user is able to add noise to any image in the generated tilt series, as well as in plane translation and rotation errors, from all of the distributions listed in table (4.3). As the primitive objects to be added to the virtual model are defined in the model geometry file, the list of projections to be created are defined in the projection geometry file, which possesses a different syntax to that used in the model geometry file. The syntax

is depicted in table (4.4), where σ_x and σ_y are the magnitudes of in plane shift in the x and y directions respectively, τ_ρ is the magnitude of in plane rotation and μ_p the per pixel noise applied to each pixel of the projection image.

ϕ	θ	ψ	σ_x	σ_y	τ_ρ	μ_p

Table 4.4: Depiction of the syntax used in projection creation.

As was the case with primitive definition, all projection parameters must be drawn from the distribution list defined in table (4.3). When the projection geometry file is executed, PhaST requires that all of the above mentioned parameters are defined, in the order presented, on each line of the projection geometry file. Extraction of the projection images from the volume is accomplished by the grid-based Fourier inversion technique implemented in SPARX [159].

To aid in the projection of tomographic data sets, the software allows the user to define an entire tilt axis in a single line using the Range command. The range command, which produces projections through a defined range of tilt angles, may only be applied to one of the Euler angles per axis and has the syntax depicted in table (4.5),

RNG	θ_l	θ_r	Δ_θ

Table 4.5: Depiction of the syntax required by the Range command in the PhaST package.

where θ_l is the lower limit of the range, θ_r the upper limit of the range, and Δ_θ the projection angle increment. Each of these variables must be drawn from the distribution pool defined in table (4.3). A sample projection geometry file is pictured in figure (4.20) and the corresponding tilt series, produced from the ellipsoidal nanocluster depicted in figure (4.19 c), is shown in figure (4.21). The first row of figure (4.21) illustrates a tilt series without any per pixel noise or in plane shift or rotation introduced, while the second row of figure (4.21) shows the same projections with varying levels of per pixel noise, drawn from a Gaussian

distribution, in the case of the first two subfigures, and from a uniform distribution, in the case of the last two subfigures.

```
#image projector input file
#contains list of possible inputs

#the image projector file must conform to the following general grammar.
#the order must be kept exact. All the statistical modifiers available to the model
#creator are also available here. At least one of the angular variables should be 'ranged'
#and not simply a single number. The range syntax works as follows:
#RNG A B C - Ranged from A to B in steps of C
#PHI THETA PSI SX SY B INT
#Each uncommented line in this file represents an independent axis, which will be saved seperately.

ABS 0 RNG -50 50 50 ABS 90 GSS 0 25 GSS 0 25 GSS 0 5 GSS 4 0
ABS 0 RNG -50 50 50 ABS 0 GSS 0 25 GSS 0 25 GSS 0 5 GSS 4 5
#RNG -50 50 2 ABS 20 ABS 30 GSS 0 25 GSS 0 25 GSS 0 5 UNI 0 0
#ABS 20 ABS 30 RNG -50 50 2 GSS 0 25 GSS 0 25 GSS 0 5 UNI 0 0


INV
```

Figure 4.20: Projection geometry file to create a double axis tilt measurement.

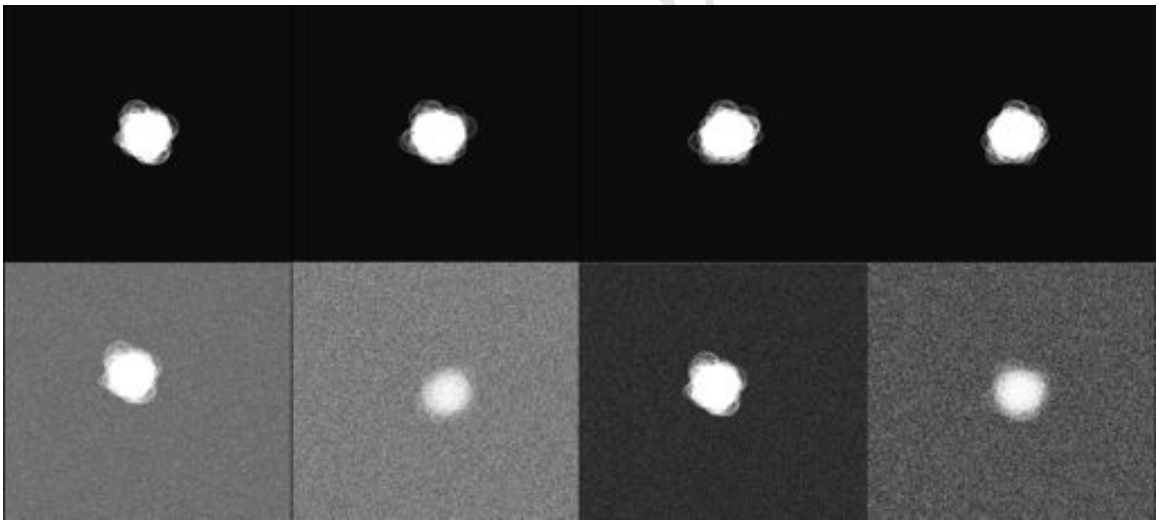

Figure 4.21: Top row, a sample subset of the first axis created by the projection geometry file shown in figure (4.20). Bottom row, the same projection from the extreme left of the top row, but with various levels of noise introduced. All images have been shifted in plane according to a Gaussian distribution. The noise seen in the images is Gaussian for the first two and uniform for the second two projections on the bottom row.

4.3.3 Comparison of the PhaST Software Package to Existing Phantom Creation Software used in Electron Microscopy

The software tool presented here differs from the currently available software by allowing the user to create three dimensional models from a large subset of three dimensional primitive objects, where each attribute associated with every primitive may be drawn from a set of distribution functions, described previously, whose parameters are defined by the user in the form of a script. The distributions allow for the modelling of a wide range of phenomena including, but not limited to: nano-particle volumetric distributions, aerosol and colloid size distributions, fibre size distribution [160], milled particle volumetric size distribution as well as size distribution of living tissues, rendering the phantom creation tool an excellent candidate to forensically analyse which alignment and reconstruction methods perform the best in the aforementioned situations.

Owing to the statistical nature of the PhaST package, when a script is run twice, it creates a different model, defined by the same parameters in the model geometry file, thereby creating a different yet equally valid model with every execution of the script file, which is useful when a second similar model is required in order to test a specific electron microscopy technique.

The created model may then be projected to form an arbitrary number of n axis image series and the transformations and uncertainties mentioned above may be applied to each image. The shift, rotation and pixel error magnitudes may also be drawn from the same set of distributions which can be applied to the primitive objects comprising the model. This allows for the accurate simulation of errors encountered during both data acquisition as well as imaging within the electron detector, which play an important role in the testing of methods used in electron microscopy. To date there is no other phantom creation software for use in electron microscopy which, as a part of core functionality, allows for the creation of a model from primitives whose parameters may be drawn from a set of statistical distributions, and whose projections may be altered for both alignment and pixel intensity error in such a statistical manner.

4.3.4 A Comparison of Various Alignment Software Packages

It was shown in section 4.2 that the viability method of alignment produces superior alignment, both in the case of an acquired image series where the central image is badly misaligned when compared to the rest of the series as well as in the case of dense sample materials. In practice, however, different software implementations of the same technique are able to produce different results, as will be shown in this section. Therefore, in order to gain the best possible results from a tomographic experiment, it is prudent to compare the various software implementations of alignment methods against each other in order to decide which software package produces the best results in practise.

This section explores the currently available open source tomography packages, in order to deduce which alignment package performs best when applied to samples which resemble the silicon nanoparticles under study here. The software packages considered are SPARX [151], TomoJ [152], IMOD [161], SPIDER [150] and the viability method, presented earlier in this chapter.

As has been shown in the TEM image analysis presented in Chapter 3, the primary clusters have dimensions of approximately 120×80 nm, the sizes of the ellipsoidal structures, visible in figure (4.22) were created with sizes to match the results gained from TEM. The test data, pictured in figure (4.22), comprised of a set of ellipsoids with both location as well as size parameters defined by Gaussian distributions, in order to model a collection of Si nanoclusters. As information regarding the length of the third axis is not obtainable from TEM, it was assumed to be approximately equal to the short axis observed in TEM. As the silicon nanoparticles under study may be considered as dense sample material, the three dimensional test data were created to be deliberately dense. This was achieved by setting the intensity values of the voxels in the three dimensional model to 60% of the maximum allowed allowed value of 256. It should be noted that in this approximation a tilt-invariant isotropic density for the nano ellipsoids has been assumed. This model, while sufficient to explore the various alignment packages, may not entirely reflect the composition of real nano ellipsoids, which may exhibit

strong diffraction contrast.

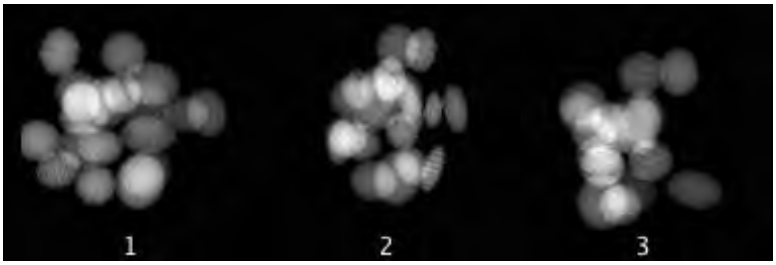

Figure 4.22: A subset of the generated phantom data set comprising 32 ellipsoids, without image noise introduced. From left to right the $-60°, 0°, +60°$ projection images of the synthesised data set.

In order to evaluate the performance of the various methods with varying degrees of image noise, several more tilt series were created with various levels of per pixel noise introduced. All noise was modelled as a zero mean Gaussian distribution, with the σ value increasing with each newly generated tilt series. A total of eight image series were projected, with Gaussian noise of deviation $0, 4, 8, 16, 32, 64, 128$ and 258 pixel intensity units respectively. The software alignment packages discussed above were then employed to produce automated, marker free alignment of all projected image series. As the misalignment is known, it is possible to calculate the residual alignment scores produced by each method for each level of image noise. One may define the average cumulative series translational residual alignment score as

$$R_\tau \equiv \frac{1}{N}\sum_{i=0}^{N}\sqrt{\left(\sigma_x^i - \rho_x^i\right)^2 + \left(\sigma_y^i - \rho_y^i\right)^2}, \tag{4.11}$$

where N is the size of the image series, σ_x^i and σ_y^i are the calculated translation parameters for the i-th series image and ρ_x^i and ρ_y^i are the known image shifts introduced to the reference series.

Sample subsets of the zero noise alignments produced by all software packages are shown in figure (4.23) and all calculated residual scores, corresponding to the alignment of all previously mentioned tilt series, are shown in figure (4.24).

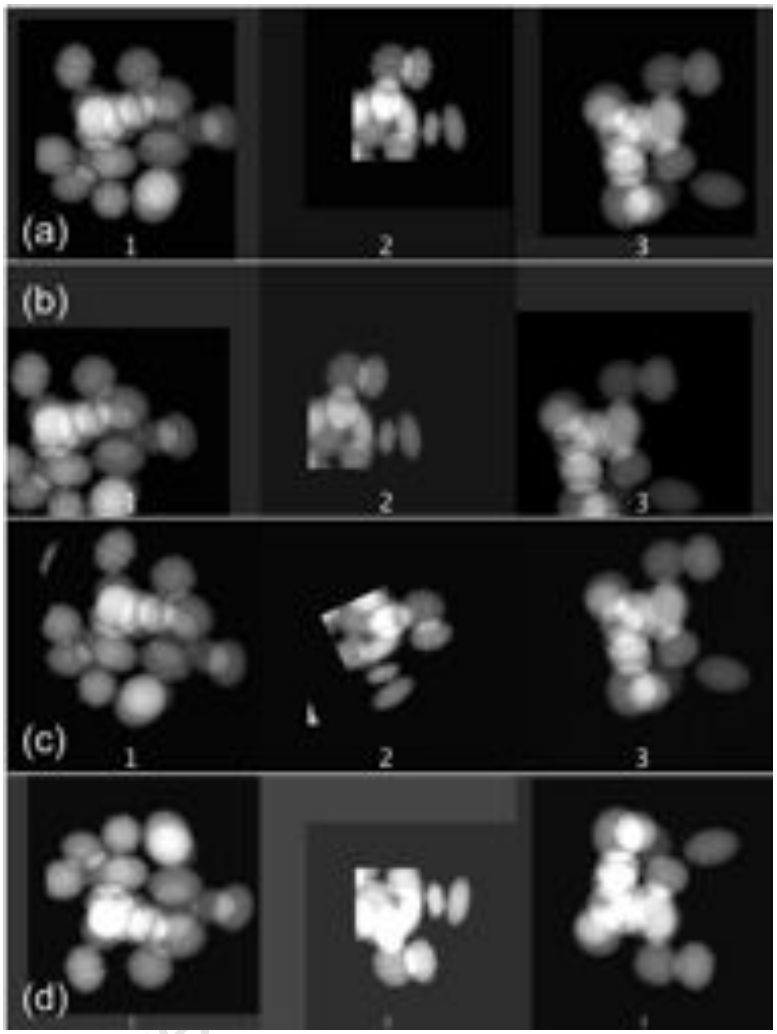

Figure 4.23: Aligned image series produced by various software packages from the synthesised test data shown in figure (4.22). Figures (a, b, c,d) show the alignments produced by the viability method, TomoJ, Sparx and IMOD respectively. Frames $1, 2, 3$ within the figures depict aligned series images of tilt angle $-60°, 0°, +60°$ respectively.

At first sight it would appear that all methods perform similarly at all but the highest levels of noise, with TomoJ producing systematically better alignment by about 3 pixels per image. The increase of the calculated residuals with increasing image noise in the case of IMOD arises from the parameters of the image filtering used in

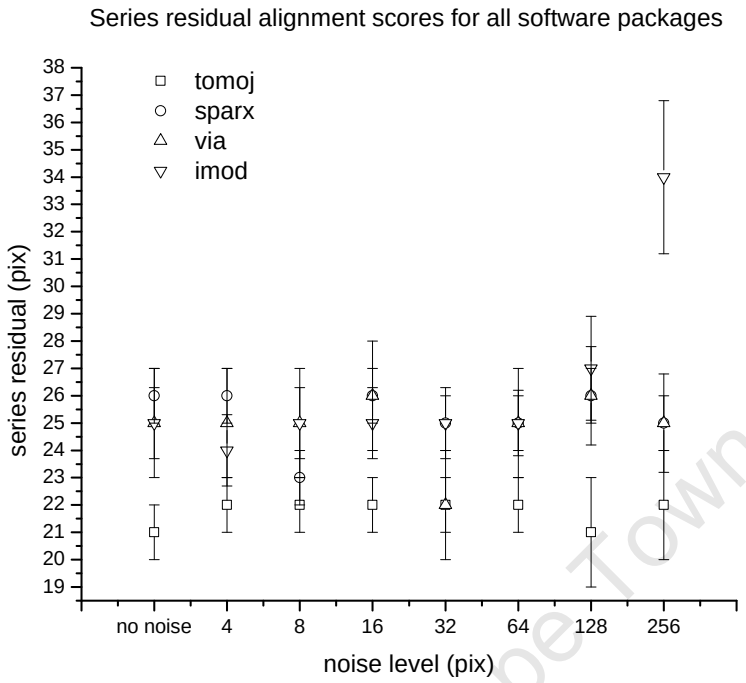

Figure 4.24: Calculated series average residuals produced by various software packages from the synthesised test data shown in figure (4.22).

the alignment. Although the residual scores seem to indicate similar performance, it is only by examining the aligned image series produced by the various methods that the subtleties in their differences become visible. Figure (4.23) shows the results produced by the various alignment methods for the $-60°, 0°, +60°$ projection images respectively. From this figure it is possible to observe various strengths and weaknesses inherent to the alignment techniques.

For example, from the second row of figure (4.23), the TomoJ package, while producing the lowest residual score systematically, is extremely sensitive to the alignment of the central series image. In this case where the central image is badly misaligned with respect to the rest of the stack, the TomoJ package attempts to shift all series images to best fit the alignment of the central image. This results in data loss in the image series as a result of image shifting. This information would

also be absent in any subsequent reconstructions. Row 3 of figure (4.23) shows the alignment produced by SPARX. Unlike the alignment produced by TomoJ, the alignment produced by SPARX does not appear to be heavily biased towards the alignment of the central image, as the remaining images have not been shifted partially out of frame to compensate for the misalignment. What is worth noting however is that the SPARX alignment has introduced an image rotation into only some of the members of the image series, while not rotating the rest. This can be seen in images $1, 3$ in the third row. These two images were generated at the same in plane rotation angle of $0°$, yet post alignment the two images have different rotational parameters, which is undesirable. The undesirable rotational alignment introduced by SPARX has produced artefacts in the images themselves, which in turn would appear as artefacts in the final reconstruction. Row 4 of figure (4.23) shows the alignment produced by the IMOD software package. The first noticeable feature of the IMOD alignment is that all images are inverted about the x axis when compared to the other alignment packages. This difference results from a directional convention and does not adversely affect alignment or reconstruction. It is also possible to observe from the aligned data set that the IMOD package is not as sensitive to the alignment of the central image as the TomoJ software package. Although the IMOD alignment does not seem to be sensitive to the alignment of the central image in a spatial sense, the brightness and contrast of the central image have been altered significantly. This drastic change in contrast, with respect to the other images in the tilt series, may cause artefacts in the reconstruction if not corrected for after alignment. This is a task which must be performed outside of the IMOD environment. In cases such as this, where the contrast of an image has been altered so much as to bleed out information, it may not be possible to recover all pixel information in regions of high contrast. Row 1 of figure (4.23) shows the alignment produced by the viability method. At first glance it is obvious that the viability package adheres to the most common directional conventions with images appearing in the standard orientation. In addition the alignment produced by the viability method does not appear to be affected by the alignment of the central image at all, with the package choosing an alignment which shifts the

position of the central image to match the remaining series images, rather than shifting all remaining series images to match the alignment of the central image. The SPARX and IMOD packages also offer this robustness, but at the cost of the introduction of significant artefacts in the aligned image series. As can be seen from row 1, columns $1, 2, 3$ the viability package achieves alignment with no adverse effect on the contrast of the aligned images, and no artefacts or image ghosting are introduced by in plane shift or rotation.

As can be seen in figure (4.19), the software allows not only for the creation of three dimensional phantom data, but also for the accurate projection of the modelled sample into an arbitrary number of tilt axes, as depicted in figure (4.21), thereby fulfilling the requirements of phantom creation software outlined in Section 4.3 above.

As the silicon nanoparticles under study in this thesis may be considered as a dense sample material which, by definition, possess contrast values close to the colour threshold used in electron tomogaphy software, the contrast artefacts produced by IMOD have a large negative effect on the alignment of an acquired tilt series and may have a negative effect on the reconstruction.

The SPARX software, which introduced unwanted image rotation to some of the images in the tilt series, also does not appear ideal for use with dense sample materials as the introduced image rotation, which was applied to only some of the images in the aligned image series, would produce unwanted artefacts in the reconstruction. The source of the unwanted image rotations may be the result of the cross-correlation operation, used by SPARX to produce alignment, performing poorly in the case of dense samples produced for testing.

The TomoJ package, while not as greatly effected either by the large density of sample or poor misalignment of the central series image as IMOD or SPARX, tends to shift useful information out of the frame of the tilt series images. This missing information in the tilt series image would also be missing in any produced reconstructions, which is clearly undesirable.

The viability software package, however, does not demonstrate any of the artefacts observed in the other alignment software packages investigated and appears to be a good candidate for the alignment of an image series, in the case of dense sample materials as well as the alignment of an image series which possesses large misalignment of the central series image.

The PhaST software easily lends itself to the creation of large, physically meaningful data sets. It is therefore ideal for thoroughly testing tomographic alignment techniques, three dimensional reconstruction techniques, automatic size distribution techniques as well as many others. The ability to add different types of noise to the projection images may also be used to test a wide variety of *CCD* software tools, such as flattening algorithms etc. As many biological samples may be described by distributions, PhaST is a powerful tool to test single particle techniques.

4.4 Electron Tomography of Silicon Nanoparticle Clusters

4.4.1 Sample Preparation

Sample preparation for the tomography experiment was similar to the sample preparation detailed in section 3.2.1, with the nanoparticles produced as in section 2.3.2, with a milling time of 300 minutes. As sample occlusion at high tilt angles owing to foreshortening is problematic in tomography, samples were prepared at a lower concentration of nanoparticle to methanol when compared to the samples prepared for normal TEM and HRTEM imaging, so as to minimise occlusion. As was the case in the previous experiments, the particle dispersions in methanol were dropped onto plain carbon grids using a micro-pipette.

4.4.2 Determination of the Cluster Size Distribution by Electron Tomography

In this section electron tomography is used to gain information about the size distribution as well as the aspect ratios of nanoparticle clusters, by following a similar method to the size distribution determination from TEM images, presented in Chapter 3. The microscope used for data acquisition was the FEI T20 TEM with a L_aB_6 filament and a 2048×2048 pixel camera. An accelerating voltage of 200kV was used throughout data acquisition. Many single axis image series were acquired, each with a tilt range of $-50°$ to $50°$ at an angular step of $0.2°$. As each image series comprised 500 images, the Leginon data acquisition package was used to automate the data acquisition process [162], resulting in many separate single axis tomograms, each containing information for many nanoparticles. To enhance the appearance of particle edges, a constant defocus of $-1.5\mu m$ was applied to each of the acquired images.

As the alignment of the Si nanoparticles under study performs poorly with fiducial markers as well as with mathematically generated landmark based alignment owing to their density, the viability method of alignment, presented in section 4.2, was used [17]. The viability method of alignment assumes no a priori sample information and is not sensitive to the alignment of the central series image, rendering it an ideal alignment tool for images of Si nanoparticles.

The IMOD software package was used for tomographic reconstruction [161], using a weighted back projection method, where the weighting used was equal to the lateral dimensions of the tilt series images. To reduce the computational cost of generating and viewing the tomogram, the images acquired from the microscope were re-scaled to a resolution of 1024×1024 pixels. The resulting tomogram was therefore reconstructed as a cube of length 1024 pixels in each direction. In order to compensate for the effect of the missing wedge, mentioned previously, all tilt series images were acquired with sufficient resolution such that the in-plane axis, perpendicular to the tilt axis, would possess the same resolution as the tilt axis in the reconstructed volume. All tomograms were re-scaled in the z direction,

according to the Crowther Criterion [136] prior to any measurements of the particle and cluster dimensions being carried out.

Figure (4.25) shows a subset of one of the data sets of TEM images used for tomogram reconstruction. As was observed in the previous study, the sample appears to be composed of single particles, clusters, a few large agglomerates and a small amount of partially milled material. An example of the latter is the trapezeoidal structure which can be seen in the upper right quadrant of figure (4.25 b). Throughout the analysis presented earlier, the presence of partially milled, sub-micron single crystallites, was detected in less than 1% of acquired micrographs, each of which contained tens, or in some cases in excess of 100, particle clusters.

As previously observed, the particles appear to possess aspect ratios greater than unity. Although similar in appearance to the artefacts produced by a strongly diffracting particle, beam-sample charging effects can also be seen in the micrographs as the ghosting artefacts which surround the larger particles as well as the partially milled crystallite. Also, as before, the white lines visible around the perimeters of particles are the intended effect of the applied defocus. The effect of the lower concentration of nanoparticle to methanol can easily be seen, when the micrographs in figure (4.25) are compared to the micrographs shown in figure (3.2), as the density of material visible in the tomography sample is significantly lower when compared to the earlier samples. This lower density greatly improves the analysis by allowing for the acquisition of data over a significantly wider angular range than would be allowed for by the samples prepared for conventional TEM imaging, owing to occlusion of the desired sample area, by neighbouring particles and clusters, at large tilt angles.

Figure (4.26) shows a third angle orthographic projection from the tomogram, reconstructed from the dataset shown in figure (4.25), corrected for anisotropy using Eq. 4.3. The orthographic projections are used for particle size and shape analysis, by highlighting the three axes of individual particles from the tomogram with crosshairs. The plan view in the lower right quadrant shows the in-plane, or XY,

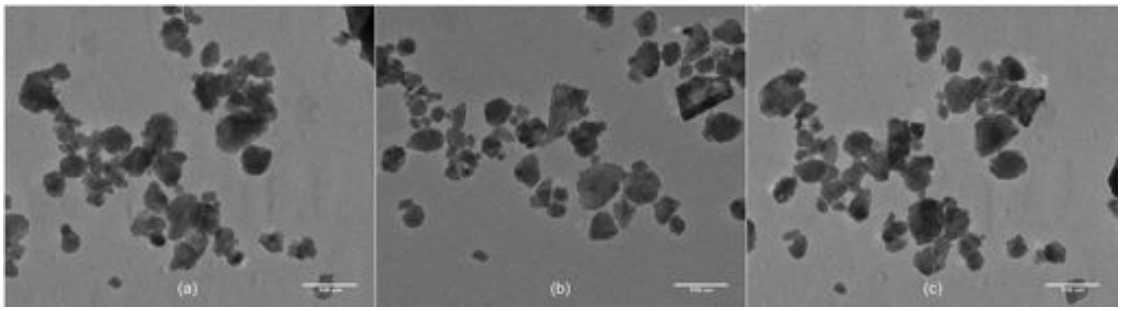

Figure 4.25: Subset of one of the tomographic data sets used in the analysis. From left to right the $-50°, 0°, +50°$ tilt series images respectively.

view of the sample, while the other two views show the YZ and XZ projections of the tomogram, sectioned through the particle of interest, respectively. Examination of the two orthogonal particle views reveals an approximately circular cross section. At first glance the particles appear to be cigar like, prolate structures with both of the minor axes being approximately equal in length.

The front view of the figure in the top right quadrant qualitatively demonstrates the the goodness-of-alignment of the image series from which the tomogram of the dense sample material, by the viability alignment method, was reconstructed. In general, when an image series is imperfectly aligned, the ray-like structures, which appear in the projections of the in-plane axis perpendicular to the tilt axis and emanate outwards from each reconstructed object in the tomogram, tend to be asymmetric, while in the case of a well aligned data set, the ray-like structures are symmetric about all objects in the reconstructed scene, as is the case here. This is important as, should the image series be imperfectly aligned, the reconstruction would, at the very least, be far less sharp and, in the worst case scenario, may suffer from distortion, such that application of the anisotropy correction, described in section (4.1.1) above, would no longer yield meaningful results.

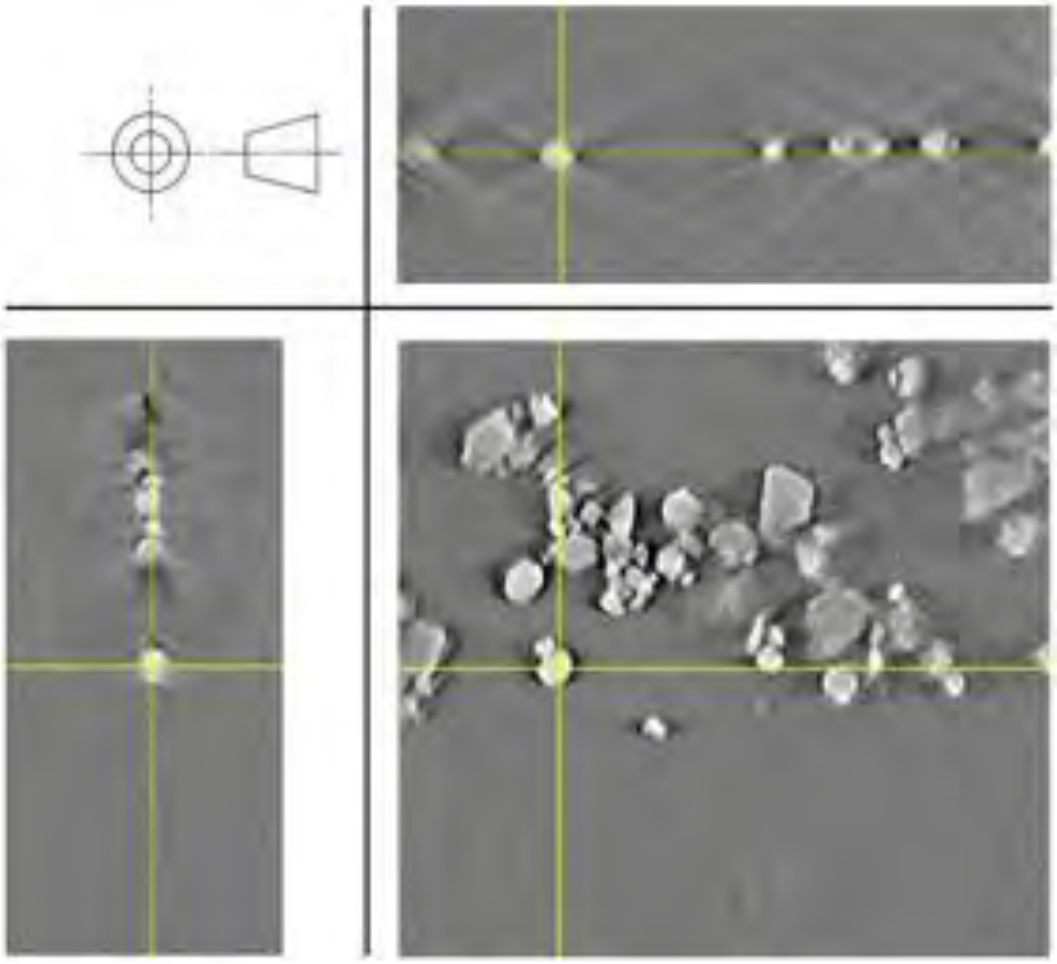

Figure 4.26: Third angle orthographic projection of the reconstruction of the sample depicted in figure (4.25), post anisotropic voxel correction. The bottom-right quadrant shows the the in-plane, or XY view, of the sample while the bottom-left and top-right quadrants show the YZ and XZ views of the sample respectively.

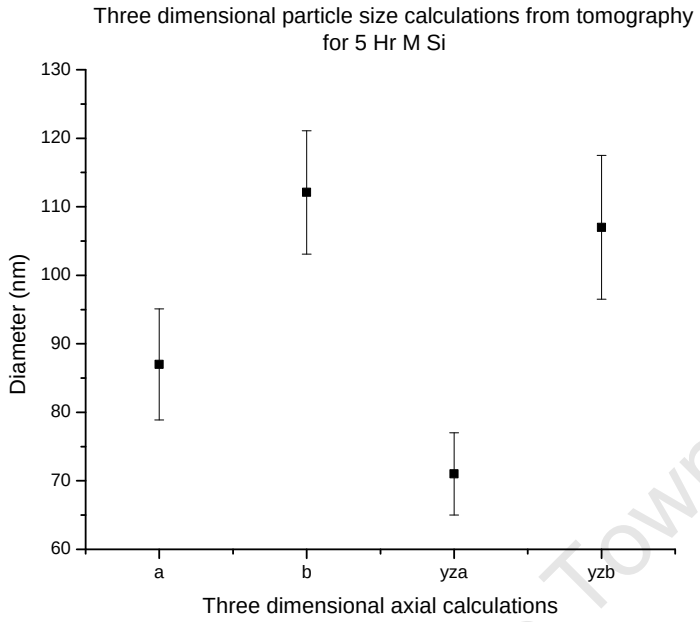

Figure 4.27: Visualisation of three dimensional axial lengths.

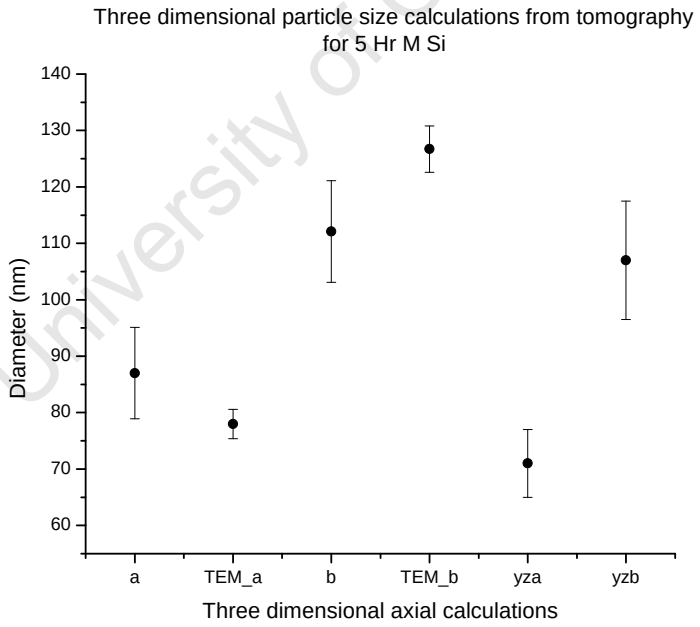

Figure 4.28: A comparison of calculated tomography results with those obtained directly from TEM images.

For each identifiable particle cluster in each tomogram, both the long and short axes were measured in the XY as well as XZ planes. These four axial measurements, corrected for voxel anisotropy, are shown in figure (4.27). Figure (4.28) shows the tomographic size results on the same set of axes as the size distribution results calculated from the TEM measurements. From figure (4.27) the average shape of the Silicon nanoparticle clusters is indeed ellipsoidal with major axis of length $b = 110 \pm 10nm$, and minor axes of length $a = 86 \pm 8nm$ and $c = 70 \pm 7nm$. From the calculated values of a, b and c, it can be inferred that the average cluster has a volume of $36 \times 10^4\ nm^3$, a surface area of $25 \times 10^3\ nm^2$, a surface to volume ratio of $7 \times 10^{-3}\ nm^{-1}$, with the surface area given by Knud Thomsen's formula

$$A_s = 4 \cdot \pi \left(\frac{a^p b^p + a^p c^p + b^p c^p}{3} \right)^{\frac{1}{p}}, \tag{4.12}$$

where p has a value of 1.6075.

Finally, the comparison between previous TEM size measurements as well as those used in the analysis, depicted in figure (4.28) are also shown to be in agreement, albeit with significantly smaller error bars. The lower uncertainty associated with the TEM size measurements may be attributed to the large data set of thousands of particles while the larger uncertainty seen in the three dimensional measurements presented here may similarly be attributed to the comparatively smaller data set comprising fewer clusters. From the agreement between the two microscopic methods, across multiple sample types with the same milling parameters, we may conclude that the particle production process is indeed consistent and is able to reliably produce materials with similar morphology, as was demonstrated in the TEM experiment.

4.4.3 Electron Tomography of a Primary Particle Cluster

In this section electron tomography is used to gain information about the morphology of primary clusters of nanoparticle clusters and the particle surface. The

microscope experimental setup used was the same as for the wide area electron tomography experiment described above. Figure (4.29a) shows a broad overview of one of the sample micrographs, while figure (4.29b) shows an enlarged view of the nanoparticle cluster which will be discussed. Similarly, figure (4.30a) shows a broad overview of the reconstructed tomogram, while figure (4.30b) shows an enlarged view of the cluster. Figure (4.31) shows a reconstruction of the particle cluster under investigation from multiple view angles. The threshold value used for the surface renderings was 0.020.

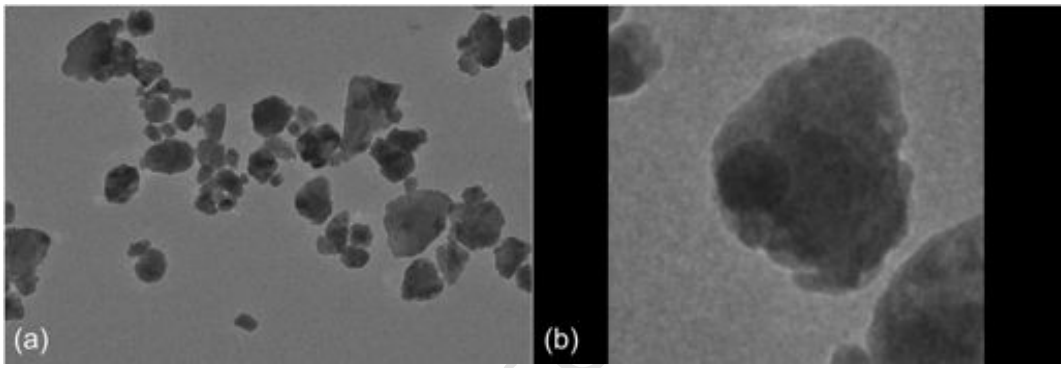

Figure 4.29: TEM micrographs depicting a single cluster. In (a), a broad overview of the tomography sample. In (b), the same micrograph as in (a), re-scaled to focus on the single cluster.

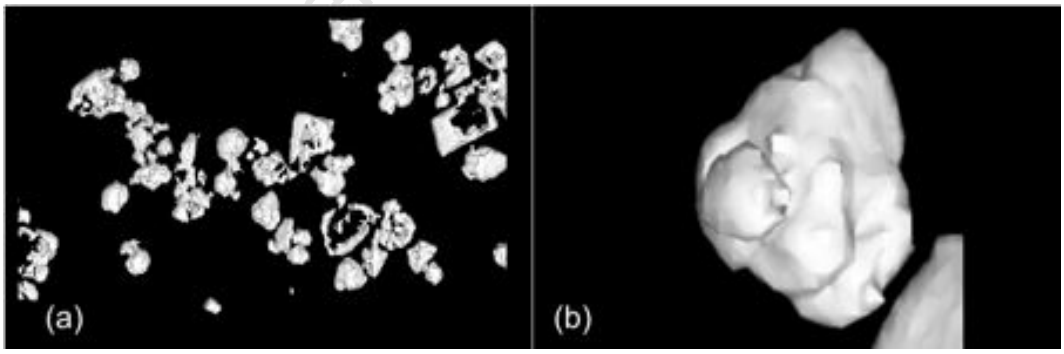

Figure 4.30: TEM reconstruction depicting a single cluster. In (a), a broad overview of the reconstruction. In (b), the same reconstruction as in (a), re-scaled to focus on the single cluster.

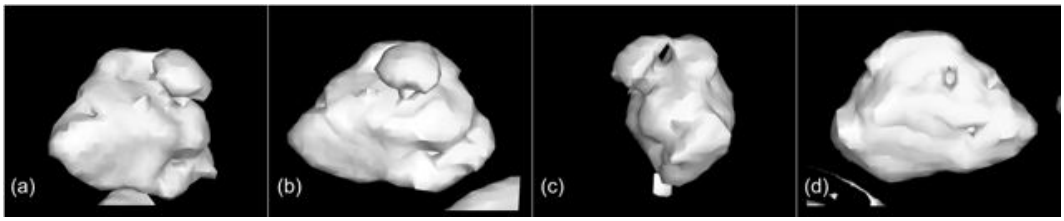

Figure 4.31: TEM reconstruction depicting a single cluster. Figures (a), (b), (c), (d), show the nanocluster various view angles.

From a comparison between figures (4.29) and (4.30), the conclusion may be drawn that both tomogram alignment as well as reconstruction are performed correctly as the reconstruction, depicted in figure (4.30) closely matches the original micrographs, pictured in figure (4.29).

However, upon examination of figure (4.31), it is clear that the structure under investigation appears to be a dense cluster and not a single particle as the outlines of the particles which make up the cluster start to become visible, with one particle, which appears loosely attached to the cluster, clearly visible on the surface of the cluster. For the case of the loosely attached particle, as well as for the particles which appear more tightly attached, two dimensional TEM images, such as figure (4.25) and those used the analysis presented previously, are insufficient to determine the particle location relative to the cluster. As can be seen from figure (4.29 b), it is not possible to determine whether or not the particle lies above, below, or inside the cluster and, consequently, no conclusions may be drawn with regards to particle attachment to the cluster. This information is only obtainable from reconstruction, which clearly shows, as depicted in figure (4.31), that the particle is attached to the cluster and is located at the front of the cluster, when the cluster is oriented as in figure (4.29 b).

From scaled measurements, the size of the reconstructed object is approximately 130 nm and the size of the loosely attached particle approximately 40 nm, as measured across the longest axes of the cluster and particle respectively.

4.4.4 Physical Representation of a Single Cluster by Three Dimensional Printing and Vitrography

This section describes the physical reconstruction of the three dimensional information in the tomogram, reconstructed from a single silicon nanoparticle cluster, into a real world object via three dimensional printing and three dimensional representation of the tomogram inside of a block of optical glass achieved with laser engraving, also known as vitrography [163]. The former is equivalent to a solid rendering view of the tomogram, whereas the latter corresponds to a map of the surface.

The three dimensional printer used to produce the object was the CREATOR printer, manufactured by 3D Stuffmaker. The printer works by first reducing the model to be printed into a set of two dimensional planes, which are then printed on top of each other in the correct order to produce the object. Each printed layer is composed of polylactic acid (PLA), a thermoplastic aliphatic polyester, created from renewable resources, which is melted and extruded through a print head, by a process known as fused filament fabrication (FFF) [164].

The CREATOR printer used here is able to print objects of maximum dimension 110x130x105 mm in the x, y and z dimensions respectively, with a minimum layer thickness of 100μm and a layer placement accuracy of 5μm [165]. The object under study was produced at the highest possible resolution of the printer.

Figure (4.32) depicts the printed nanocluster from similar view angles as shown in figure (4.31). From a comparison between these two figures it is clear that the three dimensional printed object closely resembles the depicted tomogram and reproduces the structures visible in the tomogram. The parallel lines, seen in the photograph, correspond to the individual planes from which the model is constructed. This is an artefact of the printing process and is not a structural feature of the sample.

From an examination of the solid model it can be seen the cluster under study is hierarchical, i.e., that the cluster is composed of a large nanoparticle as a core with

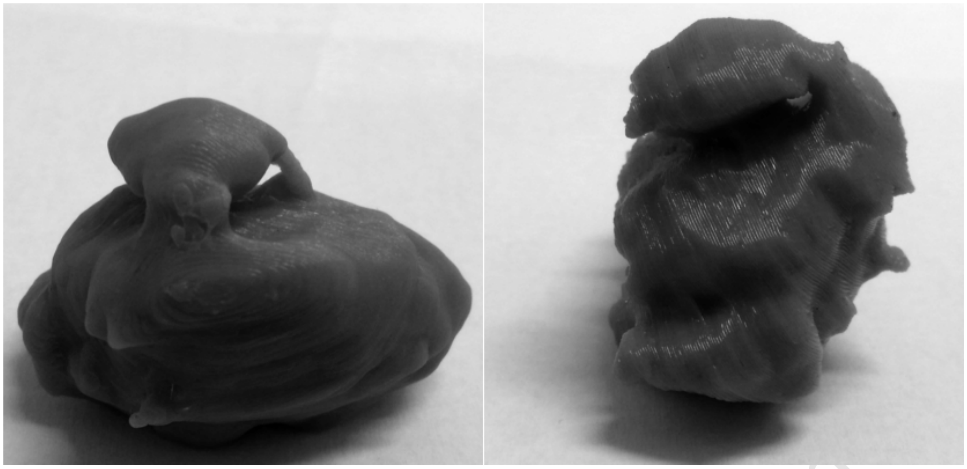

Figure 4.32: Two views of a three dimensionally printed real world object, corresponding to the tomographic reconstruction depicted in figure (4.31).

increasingly smaller particles attached to the cluster, with the sizes of the attached particles decreasing with increasing distance from the centre. This cannot easily be deduced from the tomogram data presented in figure (4.31), but is especially visible in figure (4.32 a), which clearly depicts a large central structure, with smaller structures attached.

In order to produce the glass structure by vitrography, a Mee Laser Engraver 1000 was used. This hardware applies a high energy, 1kW, green laser to high quality optical lead crystal glass in order to create small spherical fractures within the glass. Each of the fractures corresponds to a discrete point from the model being printed and, when sufficiently many discrete points are produced, the three dimensional image, shown in figure (4.33), is created inside the glass block that closely matches the model file.

At first glance, it is clear that the structure created inside the lead glass block closely matches both the tomographic reconstruction, shown in figure (4.31) and the three dimensionally printed solid model. Closer examination of the figure, however, reveals that the vitrograph shows considerable information with respect to both the attachment of the loosely bound particle to the cluster as well as information regarding the surfaces of many of the particles which constitute the

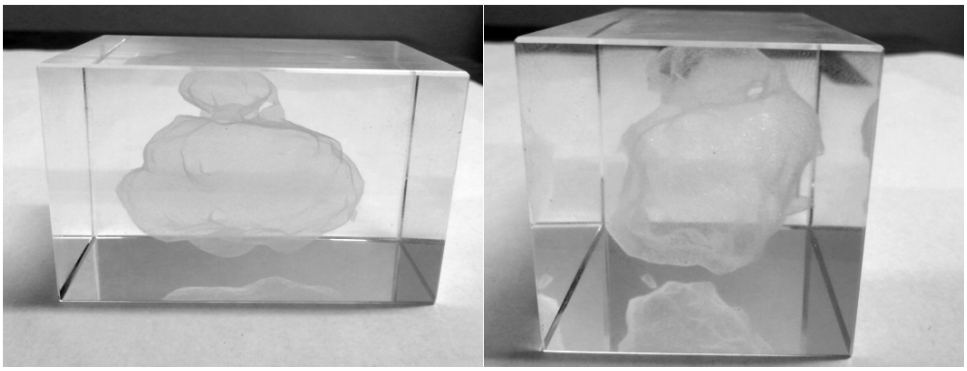

Figure 4.33: A three dimensional representation of a cluster produced by vitrography, corresponding to the tomographic reconstruction depicted in figure (4.31).

cluster.

In figure (4.32) it can be seen that the surfaces of the particles which make up the cluster are, in fact, faceted. This interesting feature, which is not readily viewable from either conventional tomography, which is ultimately a two dimensional representation of a three dimensional object onto a computer display, or from three dimensional printing techniques, owing to the opaque nature of the PLA plastic, is depicted clearly in the vitrograph.

The three cluster representations shown thus far each provide new information about the particle cluster. From the two dimensional TEM analysis it appears as though the object is a cluster, as the object appears to possess internal structure, while the tomography analysis confirms that the object is indeed a cluster and shows the general morphology. The three dimensionally printed cluster shows that the particle clustering is in fact hierarchical, which cannot easily be determined from the previous sample representations. From the vitrograph it is clear that the nanoparticles which are attached to the cluster core possess faceted surfaces. While this information is technically recoverable from solid and intensity representations of the tomogram, the vitrograph and solid model add a tactile sense and gestalt that provides a superior three dimensional overview of the sample when compared only to the intensity and solid mode representations commonly used in electron tomography

5 Combination of Electron Tomography and Ultra Small X-ray Scattering (USAXS) to Study Cluster Orientation in Printed Nanoparticulate Layers

In this chapter the experimental results obtained from electron microscopy and tomography will be brought together in order to infer structural and orientation information regarding the silicon nanoparticles and nanoparticle clusters which comprise a printed silicon layer as presented in chapter 2. To do so the experimental results of the electron tomography based size distribution, presented in chapter 4, will be combined with the USAXS experimental data. As the particles used to create the printed silicon layers are the same particles under study in the tomography experiment, it follows that the first structural level observed by USAXS corresponds either to the nanoparticle size or to the size of the smallest stable primary clusters, composed of particles, which may be considered as a quasi-species of particle in their own right.

Small angle scattering (SAS) is the name given to a group of experimental techniques which allow researchers to probe the structure of small systems with feature sizes in the range of 10 to 10^4 Angstroms [166]. The techniques work by scattering incident radiation, usually light, X-rays or neutrons, from a sample and then analysing the resulting scattering pattern to extract sample information such as particle size [167] at an angle of acquisition which is small enough so as to correspond to the zeroth order of diffraction. As the mathematical principles which govern SAS are independent of the frequency or type of the incident radiation, the technique is able to observe a wide range of sample sizes by altering the beam source [168]. If an X-ray wavelength source is used, the observable feature sizes are of the order of Angstroms, and the technique is known as small angle x-ray scattering (SAXS) [169, 170].

In SAXS the energy of the X-rays is generally high, of the order of 15 kV [171], so

that all electrons in the sample contribute to the scattering pattern. The scattering intensity, describing the scattering of the radiation beam from a single particle, at a scattering angle of 2θ can be expressed mathematically as

$$I(\boldsymbol{q}) = \frac{1}{V}|\int_V \rho(r)e^{-i\boldsymbol{q}r}dr|^2, \tag{5.1}$$

where $\rho(r)$ is the sample electron density, V is the illuminated sample volume and q is the scattering vector of the form

$$\boldsymbol{q} = \frac{4\pi \sin\theta}{\lambda}, \tag{5.2}$$

where θ is the scattering angle and λ the wavelength. As the scattering intensity, $I(q)$, is proportional to the square of the Fourier transform of the electron density, for many identical particles, where $\rho(r)$ is a constant, the scattering function may be expressed as:

$$I(\boldsymbol{q}) = \frac{N}{V}\left(\rho_P - \rho_0\right)^2 V_P^2 |\frac{1}{V_P}\int \rho(r)e^{-i\boldsymbol{q}r}dr|^2, \tag{5.3}$$

where $\rho_P - \rho_0$, often referred to as the scattering contrast, is the difference in electron density between the particle and the surrounding medium, which may be a vacuum, and V_p is the volume occupied by one particle. The form factor, $P(q)$, is defined as

$$P(\boldsymbol{q}) = |\frac{1}{V_P}\int \rho(r)e^{-i\boldsymbol{q}r}dr|^2. \tag{5.4}$$

The scattering intensity function, as well as the form factor and scattering contrast, all depend on the structure being modelled [172]. In the case of particulate systems which contain sharp interfaces, a new scattering intensity function may be derived for q large compared to the inverse size of the scattering object,

$$I(\boldsymbol{q}) = \frac{2\pi S(\Delta\rho_P)^2}{\boldsymbol{q}^4}, \tag{5.5}$$

where S is the surface area of the scatterer and $\Delta\rho_P$ is the scattering contrast corresponding to a vacuum. This case, where the scattering intensity drops by the fourth power of the scattering vector is known as Porod's law [173]. Deviations from Porod's law indicate a fractal structure [174]. When the magnitude of q is similar to the inverse size of the scattering object the equation which describes scattering from an isolated particle, where coherent X-ray scattering occurs between various regions of the particle, is known as the Guinier law [173]

$$I(\boldsymbol{q}) = I_0 exp(-\boldsymbol{q}^2 \frac{R_g^2}{3}). \tag{5.6}$$

R_g is known as the radius of gyration and is defined as the root mean square of the distances between the electrons and the centroid of their distribution [173]. Fundamentally, the radius of gyration, or R_g, stands out as one of the most important parameters in the field of small angle scattering as it is the parameter which is used to describe particle size. Mathematically the radius of gyration is expressed as

$$R_g^2 = \frac{\int \Delta\rho(r_i) r_i^2 dV_i}{\int \Delta\rho(r_i) 2 dV_i}. \tag{5.7}$$

From the above relation, the radius of gyration for various solid objects may be derived, the most common of which is

$$R_g = \sqrt{\frac{3}{5}} R, \tag{5.8}$$

which defines the radius of gyration for a solid sphere of radius R. For the case of a solid rod of length L with circular cross section of radius R

$$R_g = \frac{L^2}{12} + \frac{R^2}{2}. \tag{5.9}$$

Finally, as the nanoparticles under study are modelled as ellipsoids, the radius of gyration for a solid ellipsoid with major axis length b, and minor axes a c is given

by

$$R_g = \frac{1}{\sqrt{5}} \left(a^2 + b^2 + c^2\right)^{\frac{1}{2}} . \tag{5.10}$$

5.1 USAXS Study of Printed Silicon

For the USAXS experiments, the silicon nanoparticles were produced as described in section 2.3.2, with a milling time of 300 minutes. The nanoparticles were then used as the active component in the four semiconductor inks, each differing in nanoparticle concentration, as described in section 2.4. The printed layers, which correspond to the USAXS samples under study in this section, were produced from these various inks as described in section 2.4.

Figure (5.1) shows a typical USAXS experimental setup [175], where the collimating Si (220) crystals act as a monochromator to ensure a nearly parallel beam, while the Si (220) analysing crystals, placed in between the sample and the detector, allow the scattering intensities to be measured as a function of the scattering vector q, defined below, by rotating both the analysing crystals as well as the detector.

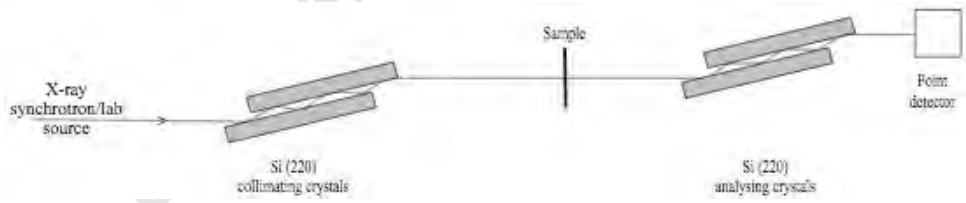

Figure 5.1: Schematic diagram depicting a typical USAXS setup [175].

The USAXS measurements were conducted as part of a study of the influence of flow properties on network topology [175, 176] at the Advanced Photon Source, Argonne National Laboratories using the USAXS facility at Sector 15ID [175]. With a beam energy of 16.85 keV, a q range of $1.5 \times 10^{-4}\text{Å}^{-1} < q < 1\text{Å}^{-1}$ could be covered. In both reports, the focus was basically on the aggregates with no

particular emphasis on the shape of the primary clusters, but the radii of gyration for different structural levels were determined.

The desmeared scattering data for all the samples were fitted using the unified fitting function [177] which is given as

$$I(q) = \sum_{i=1}^{n} G_i \exp\left(\frac{-q^2 R_{gi}^2}{3}\right) + B_i \exp\left(\frac{-q^2 R_{g(i+1)}^2}{3}\right) \left[\frac{(erf(qR_{gi}/\sqrt{6}))^3}{q}\right]^{p_i}. \tag{5.11}$$

In Eq. 5.11, n is the number of structural levels in the scattering pattern where $i = 1$ refers to the smallest structural level or the primary particles. The first term of Eq 5.11, which is the Guinier function, describes a structure of average size R_{gi} with G_i as the Guinier prefactor. The second term originates from the Porod equation, with prefactor B_i and a power law exponent p_i, for a structural level. For all samples, two structural levels were fitted to the data but, for the purposes of the analysis presented in this work, the radius of gyration for the first structural level corresponding to the primary particle or cluster size is of particular interest. The primary radii of gyration were found to be 57 ± 3, 95 ± 5, 120 ± 3 and 150 ± 5nm for the layers printed from inks with particle loadings ranging from 80% to 50% inks respectively [98].

5.2 Radii of Gyration for a Network of Ellipsoidal Particles

In order to combine the results of electron tomography with the scattering data, a measurand which is independently calculable in all experiments is exploited, namely the radius of gyration, described above. As USAXS measures changes in the electron density of the sample, it observes the distance between the centres of the particles, which corresponds to their diameter when closely connected [173]. This implies that in order to accurately compare electron microscopy based size distribution data with USAXS data, R_g must be calculated from microscopy measurements using the diameters of the particles and compare these radii of gyration

to those inferred from USAXS. As electron microscopy measures particle size characteristics directly, it is possible to calculate many reasonable candidates for the radius of gyration. These candidates differ only in the arrangements of particles within the printed layer. Thus, only those radii of gyration corresponding to actual particle configurations found within the printed layers, via USAXS, should match those calculated from microscopy experiments.

Figures (5.2) and (5.3) show a montage view of all the hypothesised network configurations of particles or primary clusters. From electron tomography experiments, it has been shown that the Silicon nanoparticles may be accurately approximated as ellipsoids with dimensions 112 ± 10, 86 ± 8, $70 \pm 7nm$, for the three axes respectively.

Some of the hypothesised cluster network configurationss, namely those depicted in figures (5.2a) and (5.2b), form a pair of network geometries which correspond to the same radius of gyration. With the current USAXS data, this degeneracy cannot be resolved. On the other hand, all remaining postulated network geometries result in unique radii of gyration, all of which are investigated, in detail, below.

Figures (5.2e) and (5.2f) show two particle network geometries, each with two particles standing vertically on top of the substrates. From the tomography analysis, we know the particles to be prolate, with the a and c axes parallel to the XY plane and the b axes orthogonal to a and c, directed out of the page, for both geometries. The dotted lines show the radii of gyration, generated by the USAXS model, for ellipsoidal particles of dimension $< a, a, b >$. Mathematically these correspond to a radius of gyration of:

$$R_g \equiv \sqrt{\frac{3}{5}a^2}, \tag{5.12}$$

Figures (5.2a) and (5.2b) show the cases of two particle network geometries, each consisting of two prolate particles sitting side-by-side on the substrates with both of the particle's b axes parallel to the substrate. The radius of gyration, generated by the USAXS model, for ellipsoidal particles of dimension $< a, b, a >$ corresponds

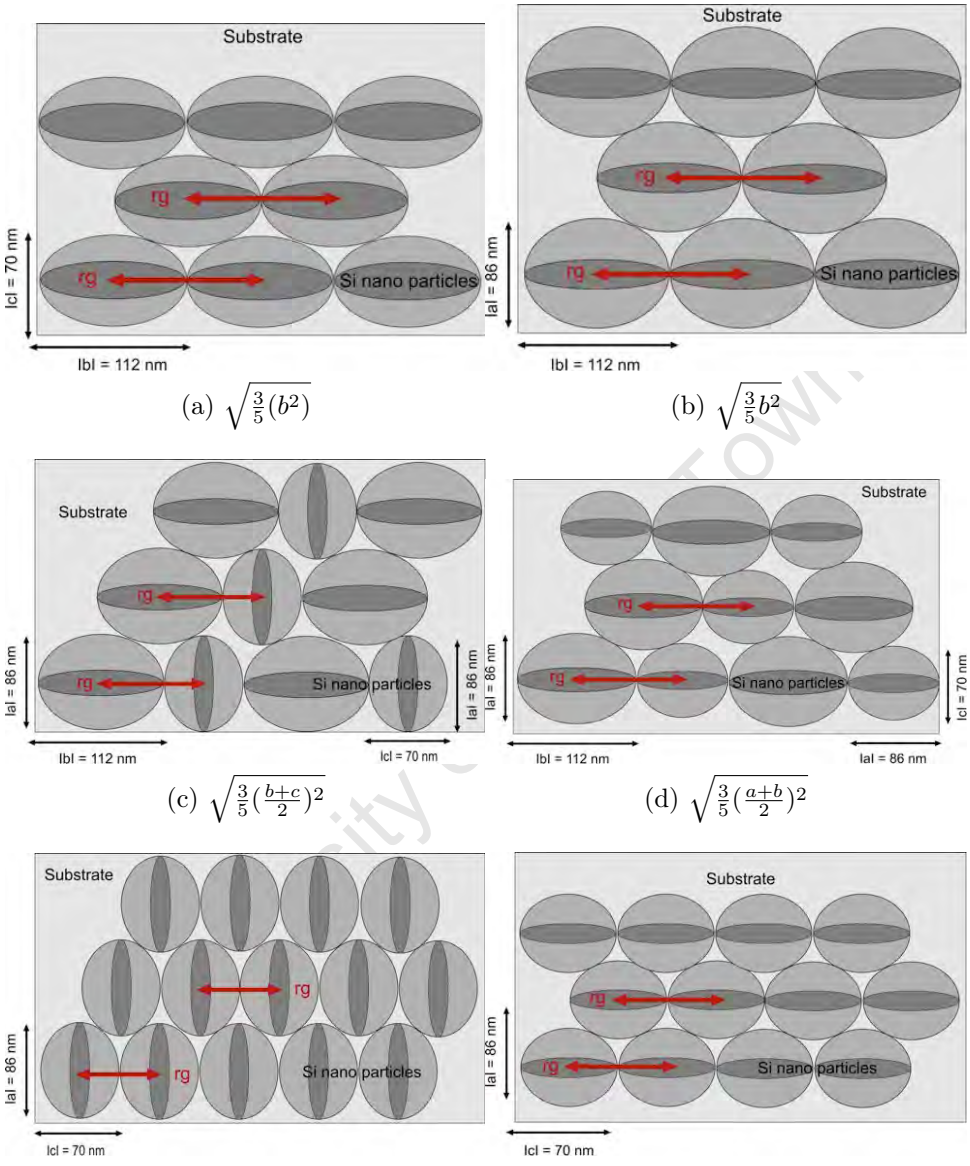

(a) $\sqrt{\frac{3}{5}(b^2)}$ (b) $\sqrt{\frac{3}{5}b^2}$

(c) $\sqrt{\frac{3}{5}(\frac{b+c}{2})^2}$ (d) $\sqrt{\frac{3}{5}(\frac{a+b}{2})^2}$

(e) $\sqrt{\frac{3}{5}(c^2)}$ (f) $\sqrt{\frac{3}{5}a^2}$

Figure 5.2: Visualisation of various plausible particle network geometries with the radii of gyration shown. All geometries are viewed from above, i.e. in the XY plane, with the substrate parallel to the page.

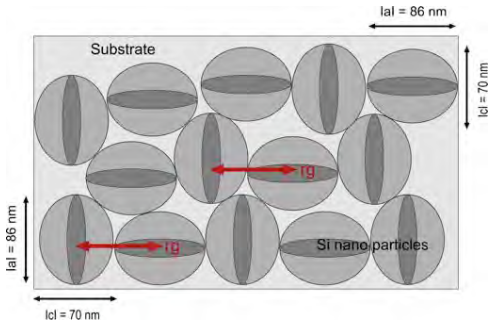

(a) $\sqrt{\frac{3}{5}(\frac{a+c}{2})^2}$

Figure 5.3: Visualisation of the final particle network geometry with the radius of gyration shown. The geometry is viewed from above, i.e. in the XY plane, with the substrate parallel to the page.

to

$$R_g \equiv \sqrt{\frac{3}{5}b^2} \tag{5.13}$$

Figure (5.2c) demonstrates the geometry of two prolate ellipsoidal particles lying next to each other with the particle on the left having its long axis, b orientated parallel to the substrate and the particle on the right having it's long axis perpendicular to the substrate. This results in a USAXS model prediction for the radius of gyration of

$$R_g \equiv \sqrt{\frac{3}{5}\left(\frac{b+c}{2}\right)^2}, \tag{5.14}$$

Figure (5.2d) demonstrates the geometry of two prolate ellipsoidal particles lying next to each other with the particle on the left having its long axis, b orientated parallel to the substrate and the particle on the right having it's long axis perpendicular to the substrate. This results in a USAXS model prediction for the radius

of gyration of

$$R_g \equiv \sqrt{\frac{3}{5}\left(\frac{a+b}{2}\right)^2}. \tag{5.15}$$

Figure (5.3) demonstrates the geometry of two prolate ellipsoidal particles next to each other each with their major, or b, axes orientated perpendicular to the substrate. The remaining two axes, namely the semi-major and minor, or a and c, are orientated such that half of the particles semi major axes are parallel to the Y axis and the other half perpendicular to the Y axis of the sample coordinate system. This results in a USAXS model prediction for the radius of gyration of

$$R_g \equiv \sqrt{\frac{3}{5}\left(\frac{a+c}{2}\right)^2}. \tag{5.16}$$

Figure (5.4) shows the radii of gyration corresponding to the postulated network geometries presented in figures (5.2) and (5.3). The radii of gyration of the various printed layers, as calculated by USAXS are superimposed on the figure. Upon first glance, it can be seen that the postulated network geometries presented in figures (5.2e, 5.2f, 5.3) agree with, within experimental uncertainty, the radius of gyration determined from the USAXS data for a printed silicon layer with a concentration of 80% silicon. In addition, the network geometries depicted in figures (5.2a) and (5.2b), agree with the radius of gyration observed by USAXS for a printed layer of 70% silicon, as does the network geometry shown in figure (5.2d), albeit with only borderline agreement. The geometry pictured in figure (5.2c), while not in agreement with any of the USAXS data, lies in between the 80% and 70% printed layers. For printed layers created from inks with below 70% Silicon, there is no observed agreement at all between electron tomography and USAXS. However, these inks are known, from electrical studies, to form a layer without an interconnecting network of particles and clusters. In this case R_g can be seen as a measure of the separation between dense small clusters.

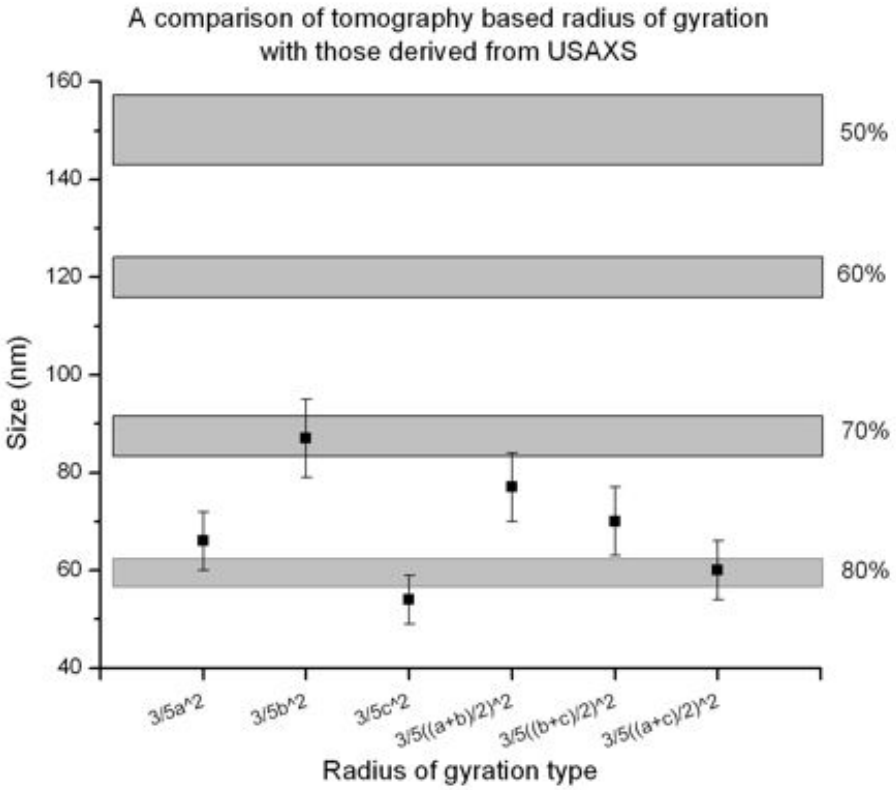

Figure 5.4: A comparison of TEM based R_g calculations vs those derived from USAXS for silicon layers printed with inks with different particle loadings.

From the agreement for layers deposited from the highest concentration inks, two different network geometries are possible (figures (5.2e) and (5.2f)). Both of these network geometries correspond to a vertical orientation of primary clusters of nanoparticles within the printed layer network, with the clusters orientated with their long axes perpendicular to the substrate, and their short axes in the plane of the substrate. The only difference between the two geometries is a 90° rotation of the particles in the plane of the substrate. The USAXS experiment is unable to differentiate between these two geometries, and it is likely that the two geometries appear within the printed layer at random with no preferred orientation, in the plane of the substrate.

In the case of printed layers created from inks with 70% particle loading, it may be

inferred that two network geometries are observed which, as in the case above, occur at random, with neither one given preference. The two geometries are depicted in figures (5.2a) and (5.2b). It is interesting to note that as the concentration of Silicon nanoparticles within the ink is reduced, the standing particle network geometry described above gives way to a network with the majority of the particles orientated with their long axes parallel to the substrate and the minority of the particles orientated with their long axes perpendicular to the substrate. It is also interesting to note that, unlike the layer containing 80% Si nanoparticles, there is an observed preferred orientation of the remaining standing particles within the printed layer in the plane of the substrate, namely the geometry depicted in figure (5.2d) agrees with USAXS data for 70% layers, while the geometry depicted in figure (5.2c) does not.

6 Conclusions

In this thesis the morphology and surface structure of high energy milled silicon nanoparticles and nanoparticle clusters have been studied using a combination of conventional TEM imaging, high resolution TEM imaging and transmitted electron tomography. These studies have shown that the nanoparticles tend to form tightly bound hierarchical clusters of particles with faceted surfaces. The high resolution TEM study has shown that the surfaces of milled particles contain regions which possess ordered structure and regions which appear amorphous. These ordered regions enable charge transport through a tightly packed network composed of nanoparticle clusters which, in turn, has led to the development of the printed electronic devices described in the introduction.

New techniques for use in electron microscopy have been presented. A correlation based alignment method, termed the viability method, has challenged the axiom in image alignment which states that in order to minimise cumulative alignment error in the direction of the image alignment, the pairwise alignment must commence from the centre of the acquired image series. It has been shown that superior results may be obtained by starting the alignment from another image in the series, which may be close to the centre. The methods presented are also not sensitive to a badly misaligned central series image unlike many of the other available methods.

New software to create distributed synthetic phantom data has also been presented. The ability to create statistically distributed data sets from a large set of three dimensional primitive objects across all parameters allows for the modelling of samples where the size, shape, orientation or location of the sample may be modelled by one of the included distributions. The advantage of the statistical approach to sample modelling is that each time an identical sample creation script is run, an entirely different, however equally meaningful, model is created, rendering the software tool an ideal candidate to test a wide range of automated analysis techniques.

As the software package is also able to create micrograph projections of the sample

at any angle, with per pixel noise, it is also an excellent tool to test many current techniques in the field of electron microscopy. In this thesis the PhaST package has been used to create the phantom data used to test the new correlation based alignment method presented in chapter 3 and also to create the phantom data for the comparison of various alignment packages, also in chapter 3. At the time of writing there exists no other software package, in the field, which offers the ability to freely create large, yet detailed statistically distributed data sets for use in electron microscopy.

The newly developed software has enabled tomography studies which have provided the means to determine the size and aspect ratio distribution of the nanoclusters. The tomography study conducted on a single nanoparticle cluster has revealed the hierarchical nature of the cluster which is composed of a large central core with smaller nanoparticles attached to it. As it is difficult to gain an overview simply by examination of a tomogram, three dimensional printing techniques and vitrography have been used to produce solid and intensity models of the cluster respectively. Although the physical models fabricated do not contain any information which is not present in the tomogram, they allow for a broad contextual overview and gestalt which greatly improves the extraction of qualitative as well as quantitative data from the reconstruction. From the solid model, morphological information is visible which demonstrates the hierarchical nature of the cluster, while from the intensity model, the surfaces of the particles which are attached to the cluster are clearly visible and found to be faceted, properties which are not easily seen when the reconstruction is viewed on either a two or three dimensional display.

From a combination of tomography and SAXS studies it has been shown that in the case of inks created from high particle loading, approximately 80%, the network is composed of nanoparticles which are aligned perpendicular to the substrate. If the particles are modelled as ellipsoids, the long axes of the ellipsoids are orientated perpendicular to the substrate, while the two short axes are orientated in the plane of the substrate. As the concentration of Si within the inks is reduced

to approximately 70% the standing arrangement of particles described above gives way to a network composed of particles of which half of the particles stand vertically, as described in the case above, while the other half are orientated with their long axes parallel to the substrate. Lowering the Si concentration further yields a printed layer in which the particles are all, on average, orientated with their longest axes parallel to the plane of the substrate.

References

[1] T.H.J. van Osch, J. Perelaer, A.W.M. de Laat, and U.S. Schübert. Inkjet printing of narrow conductive tracks on untreated polymeric substrates. *Advanced Materials*, 20(2):343 – 345, 2008.

[2] D.T. Britton and M. Härting. Printed nanoparticulate composites for silicon thick film electronics. *Pure and Applied Chemistry*, 78:1723–1739, 2006.

[3] A.C. Arias, J. Daniel, B. Krusor, S. Ready, V. Sholin, and R. Street. All-additive ink-jet-printed display backplanes: Materials development and integration. *Journal of the Society for Information Display*, 15(7):485 – 490, 2007.

[4] U.P. Männl, A. Chuvilin, B. Magunje, E.O. Jonah, M. Härting, and D.T. Britton. Interfacial and network characteristics of silicon nanoparticle layers used in printed electronics. *Japanese Journal of Applied Physics*, 52(5):05DA11–05DA11–3, 2013.

[5] M. Härting, J. Zhang, D.R. Gamota, and D.T. Britton. Fully printed field effect transistors. *Applied Physics Letters*, 94:193509, 2009.

[6] M. Pudas, J. Hagberg, and S. Leppavuori. Printing parameters and ink components affecting ultra-fine-line gravure-offset printing for electronics applications. *Journal of the European Ceramic Society*, 10(11):2943 – 2950, 2004.

[7] D.T. Britton, S.D. Walton, S. Zambou, B. Magunje, E.O. Jonah, and M. Härting. A novel mode of current switching dependent on activated charge transport. *AIP Advances*, 3(8):082110, 2013.

[8] D.T. Britton, E.A. Odo, G. Goro Gonfa, E.O. Jonah, and M. Härting. Size distribution and surface characteristics of silicon nanoparticles. *Journal of Applied Crystallography*, 42:448–456, 2009.

[9] Y. Lee, J. Choi, K.J. Lee, N.E. Stott, and D. Kim. Large-scale synthesis of copper nanoparticles by chemically controlled reduction for applications of inkjet-printed electronics. *Nanotechnology*, 41:415604, 2008.

[10] Y. Li, Y. Wu, and B.S. Ong. Facile synthesis of silver nanoparticles useful for fabrication of high-conductivity elements for printed electronics. *Journal of the American Chemical society*, 127(10):3266 – 3267, 2005.

[11] S. Magdassi, M. Grouchko, and A. Kamyshny. Copper nanoparticles for printed electronics: Routes towards achieving oxidation stability. *Materials*, 3(9):4626 – 4638, 2010.

[12] R. Shankar, L. Groven, A. Amert, K.W. Whites, and J.J. Kellar. Non-aqueous synthesis of silver nanoparticles using tin acetate as a reducing agent for the conductive ink formulation in printed electronics. *Journal of Material Chemistry*, 21:10871 – 10877, 2011.

[13] X. Huang, X. Teng, D. Chen, F. Tang, and J. He. The effect of the shape of mesoporous silica nanoparticles on cellular uptake and cell function. *Biomaterials*, 31(3):438 – 448, 2010.

[14] D.E. Olins, A.L. Olins, H.A. Levy, R.C. Durfee, S.M. Margle, E.P. Tinnel, and S.D. Dover. Electron microscope tomography: Transcription in 3-d. *Science*, 220:498–500, 1983.

[15] R.A. Crowther and A. Klug. Art and science or conditions for three-dimensional reconstruction from electron microscope images. *Journal of Theoretical Biology*, 32(1):199–203, 1971.

[16] M. Radermacher. *Weighted back-projection methods in electron tomography.* Springer, 1992.

[17] S.D. Jones and M. Härting. A new correlation based alignment technique for use in electron tomography. *Ultramicroscopy*, 135:56 – 63, 2013.

[18] E.O. Jonah, D.T. Britton, P. Beaucage, D.K. Rai, G. Beaucage, B. Magunje, J. Ilavsky, M.R. Scriba, and M. Härting. Topological investigation

of electronic silicon nanoparticulate aggregates using ultra-small-angle x-ray scattering. *Journal of Nanoparticle Research*, 14:1 – 10, 2012.

[19] T. Rieker, A. Hanprasopwattana, A. Datye, and P. Hubbard. Particle size distribution inferred from small-angle x-ray scattering and transmission electron microscopy. *Langmuir*, 15:638–641, 1999.

[20] A. Prasad, R. Schroff, S.Rane, and G. Beaucage. Morphological study of hdpe blown films by saxs, sem and tem: a relationship between the melt elasticity parameter and lamellae orientation. *Polymer*, 42:3103–3113, 2001.

[21] V. Causin, C. Marega, A. Marigo, and G. Ferrara. Assessing organo-clay dispersion in polymer layered silicate nanocomposites: A saxs approach. *Polymer*, 46:9533–9537, 2005.

[22] J.M. Rosalie and B.R. Pauw. Form-free size distributions from complementary stereological tem/saxs on precipitates in a mg-zn alloy. *Condensed Matter Materials Science*, page arXiv:1210.5366v4, 2013.

[23] Industry Standards Organisation. Nanotechnologies – terminology and definitions for nano-objects – nanoparticle, nanofibre and nanoplate, 2008.

[24] C. Granqvist, R. Buhrman, J. Wyns, and A. Sievers. Far-infrared absorption in ultrafine al particles. *Physical Review Letters*, 37(10):625, 1976.

[25] C. Hayashi, R. Uyeda, and A. Tasaki. Ultra-fine particles: exploratory science and technology (1997 translation of the japan report of the related erato project 1981-86). *Noyes Publications*, 1997.

[26] L.B. Kiss, J. Soderlund, G.A. Niklasson, and C.G. Granqvist. New approach to the origin of lognormal size distributions of nanoparticles. *Nanotechnology*, 10:25, 1999.

[27] G. Reiss and A. Hutten. *Handbook of Nanophysics: Nanoparticles and Quantum Dots.* CRC Press, 2010.

[28] F.A. Khan. *Biotechnology Fundamentals.* CRC Press, 2012.

[29] P.S. Rawson. *Ceramics.* University of Pennsylvania Press., 2012.

[30] M. Faraday. Experimental relations of gold (and other metals) to light. *Phil. Trans. Roy. Soc. London*, 147:145 – 181, 1857.

[31] K.L. Kelly, E. Coronado, L.L. Zhao, and G.C. Schatz. The optical properties of metal nanoparticles: The influence of size, shape, and dielectric environment. *Journal of Physical Chemistry B*, 107(3):668 – 677, 2002.

[32] A. Gajewicz, T. Puzyn, B. Rasulev, D. Leszczynska, and J. Leszczynski. Metal oxide nanoparticles: Size-dependence of quantum-mechanical properties. *Nanoscience and Nanotechnology Asia*, 1:53 – 58, 2011.

[33] B. Clemens, X. Chen, R. Narayanan, and M.A. El-Sayed. Chemistry and properties of nanocrystals of different shapes. *Chemical Review*, 105:1025 – 1102, 2005.

[34] Y.L. Hewakuruppu, L.A. Dombrovsky, C. Chen, V. Timchenko, X. Jiang, S. Baek, and R.A. Taylor. Plasmonic pump-probe method to study semi-transparent nanofluids. *Applied Optics*, 52(24):6041 – 6050, 2013.

[35] Haizheng Zhong, Zhibin Wang, Enrico Bovero, Zhenghong Lu, Frank C. J. M. van Veggel, and Gregory D. Scholes. Colloidal cuinse2 nanocrystals in the quantum confinement regime: Synthesis, optical properties, and electroluminescence. *The Journal of Physical Chemistry C*, 115(25):12396–12402, 2011.

[36] J.A. Scholl, A.L. Koh, and J.A. Dionne. Quantum plasmon resonances of individual metallic nanoparticles. *Nature*, 483:421 – 427, 2012.

[37] R.A. Taylor, P.E. Phelan, T.P. Otanicar, R. Adrian, and R. Prasher. Nanofluid optical property characterization: Towards efficient direct absorption solar collectors. *Nanoscale Research Letters*, 6(1):225, 2011.

[38] Yen-Hsun Su, Yuan-Feng Ke, Shi-Liang Cai, and Qian-Yu Yao. Surface plasmon resonance of layer–by–layer gold nanoparticles induced photoelec-

tric current in environmentally–friendly plasmon–sensitized solar cell. *Light: Science and Applications*, 14, 2012.

[39] J.M. Luther, P.K. Jain, T. Ewers, and A.P. Alivisatos. Localized surface plasmon resonances arising from free carriers in doped quantum dots. *Nature Materials*, 10:361 – 366, 2011.

[40] Shunping Zhang, Kui Bao, Naomi J. Halas, Hongxing Xu, and Peter Nordlander. Substrate-induced fano resonances of a plasmonic nanocube: A route to increased-sensitivity localized surface plasmon resonance sensors revealed. *Nano Letters*, 11(4):1657–1663, 2011.

[41] Mark J. Polking, Prashant K. Jain, Yehonadav Bekenstein, Uri Banin, Oded Millo, Ramamoorthy Ramesh, and A. Paul Alivisatos. Controlling localized surface plasmon resonances in gete nanoparticles using an amorphous-to-crystalline phase transition. *Phys. Rev. Lett.*, 111:037401, Jul 2013.

[42] K.M. Mayer, F. Hao, S. Lee, P. Nordlander, and J.H. Hafner. A single molecule immunoassay by localized surface plasmon resonance. *Nanotechnology*, 21(25):255503, 2010.

[43] S. Zeng, K.T. Yong, I. Roy, X.Q. Dinh, X. Yu, and F. Luan. A review on functionalized gold nanoparticles for biosensing applications. *Plasmonics*, 6(3):491 – 506, 2011.

[44] Obaid ur Rahman, Subash Chandra Mohapatra, and Sharif Ahmad. Fe3o4 inverse spinal super paramagnetic nanoparticles. *Materials Chemistry and Physics*, 132(1):196 – 202, 2012.

[45] Keisuke Sato, Shinobu Yokosuka, Yasunori Takigami, Kenji Hirakuri, Kouki Fujioka, Yoshinobu Manome, Hiroaki Sukegawa, Hideo Iwai, and Naoki Fukata. Size-tunable silicon/iron oxide hybrid nanoparticles with fluorescence, superparamagnetism, and biocompatibility. *Journal of the American Chemical Society*, 133(46):18626–18633, 2011.

[46] Shen Wu, Aizhi Sun, Fuqiang Zhai, Jin Wang, Wenhuan Xu, Qian Zhang, and Alex A. Volinsky. Fe3o4 magnetic nanoparticles synthesis from tailings by ultrasonic chemical co-precipitation. *Materials Letters*, 65(12):1882 – 1884, 2011.

[47] S.P. Gubin. *Magnetic nanoparticles.* Wiley., 2009.

[48] S.A. Corr. *Nanoscience: Volume 1.* Royal Society of Chemistry Publishing, 2013.

[49] K. Tvrdy, P.A. Frantsuzov, and P.V. Kamat. Photoinduced electron transfer from semiconductor quantum dots to metal oxide nanoparticles. *Proceedings of the National Academy of Sciences*, 108(1):29–34, 2011.

[50] Jingbi You, Chun-Chao Chen, Letian Dou, Seiichiro Murase, Hsin-Sheng Duan, Steven A. Hawks, Tao Xu, Hae Jung Son, Luping Yu, Gang Li, and Yang Yang. Metal oxide nanoparticles as an electron-transport layer in high-performance and stable inverted polymer solar cells. *Advanced Materials*, 24(38):5267–5272, 2012.

[51] Sudipta Sarkar, E. Guibal, F. Quignard, and A.K. SenGupta. Polymer-supported metals and metal oxide nanoparticles: synthesis, characterization, and applications. *Journal of Nanoparticle Research*, 14(2), 2012.

[52] I. Chung and M.G. Kanatzidis. Metal chalcogenides: A rich source of nonlinear optical materials. *Chemistry of Materials*, 26(1):849 – 869, 2014.

[53] J.K.J. Van Duren, B.J. Bollman, M. Roscheisen, and B. Sager. Chalcogenide solar cells, November 1 2011. US Patent 8,048,477.

[54] D.T. Britton and M. Härting. Printed nanoparticulate composites for silicon thick film electronics. *Pure and Applied Chemistry*, 78:1723–1739, 2006.

[55] Z. Zhao, Z. Zhou, J. Bao, Z. Wang, J. Hu, X. Chi, K. Ni, R. Wang, X. Chen, Z. Chen, and J. Gao. Octapod iron oxide nanoparticles as high-performance t2 contrast agents for magnetic resonance imaging. *Nature Communications*, 4:2266, 2013.

[56] A.T. Bell. The impact of nanoscience on heterogeneous catalysis. *Science*, 299(5613):1688 – 1691, 2003.

[57] M. Haruta and M. Dat. Advances in the catalysis of au nanoparticles. *Applied Catalysis A: General*, 222(1 – 2):427 – 437, 2001.

[58] M. Haruta. Catalysis of gold nanoparticles deposited on metal oxides. *CATTECH*, 6(3):102 – 115, 2002.

[59] M. Valden, X. Lai, and D. W. Goodman. Onset of catalytic activity of gold clusters on titania with the appearance of nonmetallic properties. *Science*, 281:1647 – 1650, 1998.

[60] M. Turner, V.B. Golovko, O.P. H. Vaughan, P. Abdulkin, A. Berenguer-Murcia, M.S. Tikhov, B.F.G. Johnson, and R.M. Lambert. Selective oxidation with dioxygen by gold nanoparticle catalysts derived from 55-atom clusters. *Nature*, 454:981 – 983, 2008.

[61] N. Carlie, L. Petit, , and K. Richardson. Fabrication and testing of planar chalcogenide waveguide integrated microfluidic sensor. *Optics Express*, 15(5):2307, 2007.

[62] N. Anscombe. The promise of chalcogenides. *Nature Photonics*, 5:474, 2011.

[63] M.R. Gao, Y.F. Xu, J. Jiang, and S.H. Yu. Nanostructured metal chalcogenides: synthesis, modification, and applications in energy conversion and storage devices. *Chemical Society Review*, 42:2986 – 3017, 2013.

[64] M.A. Reed. Quantum dots. *Scientific American*, 268(1):118, 1993.

[65] C. Wang, M. Shim, and P. Guyot-Sionnest. Electrochromic nanocrystal quantum dots. *Science*, 291(5512):2390 – 2392, 2001.

[66] D. Loss and D.P. DiVincenzo. Quantum computation with quantum dots. *Physical Review A*, 57:120 – 126, 1998.

[67] E.C. Cho, S. Park, X. Hao, D. Song, G. Conibeer, S.C. Park, and M.A. Green. Silicon quantum dot/crystalline silicon solar cells. *Nanotechnology*, 19(24):245201, 2008.

[68] J.H. Warner, A. Hoshino, K. Yamamoto, and R.D. Tilley. Water-soluble photoluminescent silicon quantum dots. *Angewandte Chemie*, 117(29):4626 – 4630, 2005.

[69] M. Howarth, W. Liu, S. Puthenveetil, Y. Zheng, L.F. Marshall, M.M. Schmidt, K.D. Wittrup, M.G. Bawendi, and A.Y. Ting. Monovalent, reduced-size quantum dots for imaging receptors on living cells. *Nature Methods*, 5(5):397 – 399, 2008.

[70] G. Belomoin, J. Therrien, and M. Nayfeh. Oxide and hydrogen capped ultrasmall blue luminescent si nanoparticles. *Applied Physics Letters*, 7(6):779 – 781, 2000.

[71] S.K. Murthy. Nanoparticles in modern medicine: State of the art and future challenges. *International Journal of Nanomidicine*, 2(2):129 – 141, 2007.

[72] T. Ung, L.M. Liz-Marzan, and P. Mulvaney. Optical properties of thin films of au sio2 particles. *Journal of Physical Chemistry B*, 105(17):3441 – 3452, 2001.

[73] B. Magunje. *PhD Thesis - Charge Transport in Printed Silicon Nanoparticle Networks*. University of Cape Town, South Africa, 2013.

[74] M.R. Scriba, D.T. Britton, C. Arendse, M.J. van Staden, and M. Härting. Composition and crystallinity of silicon nanoparticles synthesised by hot wire thermal catalytic pyrolysis at different pressures. *Thin Solid Films*, 517(30):3484 – 3487, 2009.

[75] M.R. Scriba, C. Arendse, M. Härting, and D.T. Britton. Hot-wire synthesis of si nanoparticles. *Thin Solid Films*, 516(5):844 – 846, 2008.

[76] Y. Wang and Y. Xia. Bottom-up and top-down approaches to the synthesis of monodispersed spherical colloids of low melting-point metals. *Nano Letters*, 4(10):2047 – 2050, 2004.

[77] Y. Kobayashi, H. Nakashima, D. Takagi, and Y. Homma. Cvd growth of single-walled carbon nanotubes using size-controlled nanoparticle catalyst. *Thin Solid Films*, 464:286 – 289, 2004.

[78] A.A. Onischuk, A.I. Levykin, V.P. Strunin, M.A. Ushakova, R.I. Samoilova, K.K. Sabelfeld, and V.N. Panfilov. Aerosol formation under heterogeneous/homogeneous thermal de- composition of silane: experiment and numerical modeling. *Journal of Aerosol Science*, 31:879 – 906, 2000.

[79] I.V. Zhigaltsev, N. Belliveau, I. Hafez, A.K. Leung, J. Huft, C. Hansen, and P.R Cullis. Bottom-up design and synthesis of limit size lipid nanoparticle systems with aqueous and triglyceride cores using millisecond microfluidic mixing. *Langmuir*, 28(7):3633 – 3640, 2012.

[80] T.Y. Kim, T. Hirano, Y. Kitamoto, and Y. Yamazaki. Novel nanoparticle milling process for bi-yig dispersed transparent films. *IEEE Transactions on Magnetics*, 39(4):2078 – 2080, 2003.

[81] N. Hanada, T. Ichikawa, and H. Fujii. Catalytic effect of nanoparticle 3d-transition metals on hydrogen storage properties in magnesium hydride mgh2 prepared by mechanical milling. *Journal of Physical Chemistry B*, 109(15):7188 – 7194, 2005.

[82] Y.B. Li, B.Q. Wei, J. Liang, Q. Yu, and D.H. Wu. Transformation of carbon nanotubes to nanoparticles by ball milling process. *Carbon*, 37(3):493 – 497, 1999.

[83] R.C. Jaeger. *Introduction to Microelectronic Fabrication (2nd ed.)*. Prentice Hall, Upper Saddle River, 2002.

[84] A.N. Broers et al. Electron beam lithography - resolution limits. *Microelectronic Engineering*, 32:131 – 142, 1996.

[85] K.W. Lee. Secondary electron generation in electron-beam-irradiated solids:resolution limits to nanolithography. *Journal of the Korean Physical Society*, 55(4):1720, 2009.

[86] S. Bernotat and K. Schonert. Size reduction. in: Ullmann encyclopedia of industrial chemistry. *Verlagsgesellschaft*, B2:5.1 – 5.39, 1998.

[87] A.J.E. Welch. The reaction of crystal lattice discontinuities to mineral dressing. in: Devel- opments in mineral dressing. *The Institution of Mining and Metallurgy, London*, pages 387 – 392, 1953.

[88] R.P. Rittinger. *Lehrbuch der Aufbereitungskunde.* Ernst and Korn, Berlin, 1867.

[89] F. Kick. *Das Gesetz der proportionalen Widerstande und seine anwendung.* Felix, Leipzeg, 1885.

[90] F.C. Bond. The third theory of comminution. *Trans. AIME*, 193:484 – 494, 1952.

[91] A.A. Griffith. The phenomena of rupture and flow in solids. *Philosophical Transactions of the Royal Society, London*, A221:163 – 198, 1920.

[92] A. Smekal. Technische festigkeit und molekulare festigkeit. *Naturwissenschaften*, 10:799 – 804, 1922.

[93] G. Heinicke. *Tribochemistry.* Akademie-Verlag, Berlin, 1984.

[94] P. Balaz. *Intensification of Chalcopyrite Oxidative Leaching.* PhD. Thesis, Mining Institute of Slovak Academy of Sciences, 1981.

[95] P. Balaz. *Extractive Metallurgy of Activated Minerals.* Elsevier, Amsterdam, 2000.

[96] R.R. Klimpel. *Introduction to the Principles of Size Reduction of Particles by Mechanical Means.* Engineering Research Center at the University of Florida, Gainesville, 1997.

[97] J.S. Wang, R. Jerome, P. Bayard, M. Patin, P. Teyssie, B. Vuillemin, and P Heim. An- ionic polymerization of acrylic monomers. 16. living anionic copolymerization of methyl methacrylate and tert-butyl acrylate as promoted by lithium 2-(2-methoxyethoxy) eth- oxide. *Macromolecules*, 27:4635 – 4638, 1994.

[98] E.O. Jonah. *PhD Thesis - The Topology and Electrical Properties of Nanoparticle Networks.* University Of Cape Town, South Africa, 2014.

[99] B. Fultz and J. Howe. *Transmission Electron Microscopy and Diffractometry of Materials.* Springer, 2007.

[100] TD. Courjon and J. Bulabois. Real time holographic microscopy using a peculiar holographic illuminating system and a rotary shearing interferometer. *Journal of Optics*, 10(3), 1979.

[101] H. H. Rose. Optics of high-performance electron microscopes. *Science and Technology of Advanced Materials*, 9:014107, 2008.

[102] N. Tanaka. Present status and future prospects of spherical aberration corrected tem/stem for study of nanomaterials. *Science and Technology of Advanced Materials*, 9:014111, 2008.

[103] A.V. Crewe, M. Isaacson, and D. Johnson. A simple scanning electron microscope. *Rev. Sci. Inst.*, 40(2):241–246, 1969.

[104] R.F. Egerton. Mechanisms of radiation damage in beam-sensitive specimens, for tem accelerating voltages between 10 and 300 kv. *Microscopy Research and Technique*, 75(11):1550–1556, 2012.

[105] B. Fultz and J. Howe. *Transmission Electron Microscopy and Diffractometry of Materials 4th ed..* Springer, 2013.

[106] A. Hubbard. *The Handbook of surface imaging and visualization.* CRC Press, 1995.

[107] P.E. Champness. *Electron Diffraction in the Transmission Electron Microscope.* Garland Science, 2001.

[108] D. Williams and C. Carter. *Transmission Electron Microscopy. 1 - Basics.* Plenum Press, 1996.

[109] J. Buckingham. Thermionic emission properties of a lanthanum hexaboride/rhenium cathode. *British Journal of Applied Physics*, 16(12):1821, 1965.

[110] R.G. Forbes and J.H.B Deane. Reformulation of the standard theory of fowler-nordheim tunnelling and cold field electron emission. *Proceedings of the Royal Society A*, 463(2087):2907 – 2927, 2013.

[111] J. Orloff. *Handbook of Electron Optics.* CRC Press, 1997.

[112] J.M. Cowley and A.F. Moodie. The scattering of electrons by atoms and crystals. i. a new theoretical approach. *Acta Crystallographica*, 199(3):609–619, 1957.

[113] R.F. Egerton. *Electron Energy-loss Spectroscopy in the Electron Microscope.* Springer, 1996.

[114] E.O. Jonah, D.T. Britton, P. Beaucage, D.K. Rai, G. Beaucage, B. Magunje, J. Ilavsky, M.R. Scriba, and M. Härting. Topological investigation of electronic silicon nanoparticulate aggregates using ultra-small-angle x-ray scattering. *Journal of Nanoparticle Research*, 14:1–10, 2012.

[115] D.T. Britton and M. Härting. Method of producing stable oxygen terminated semiconducting nanoparticles, May 7 2013. US Patent 8,434,704.

[116] G.T. Herman. *Fundamentals of computerized tomography: Image reconstruction from projection, 2nd edition.* Springer, 2009.

[117] M. Weyland and P.A. Midgley. 3d electron microscopy in the physical sciences: the development of z-contrast and eftem tomography. *Ultramicroscopy*, 96(3):413–431, 2003.

[118] R. McIntosh, D. Nicastro, and D. Mastronarde. New views of cells in 3d: an introduction to electron tomography. *Trends in Cell Biology*, 15(1):43 – 51, 2005.

[119] C. Suloway, J. Shi, A. Cheng, J. Pulokas, B. Carragher, C.S. Potter, S.Q. Zheng, D.A. Agard, and G.J. Jensen. Fully automated, sequential tilt-series acquisition with leginon. *Journal of Structural Biology*, 167(1):11 – 18, 2009.

[120] C.S Potter, H. Chu, B. Frey, C. Green, N. Kisseberth, T.J. Madden, K.L. Miller, K. Nahrstedt, J. Pulokas, A. Reilein, D. Tcheng, D. Weber, and B. Carragher. Leginon: a system for fully automated acquisition of 1000 electron micrographs a day. *Ultramicroscopy*, 77(3-4):153 – 161, 1999.

[121] C. Suloway, J. Pulokas, D. Fellmann, A. Cheng, F. Guerra, J. Quispe, S. Stagg, C.S. Potter, and B. Carragher. Automated molecular microscopy: The new leginon system. *Journal of Structural Biology*, 151(1):41 – 60, 2005.

[122] S.Q. Zheng, B. Keszthelyi, E. Branlund, J.M. Lyle, M.B. Braunfeld, J.W. Sedat, and D.A. Agard. {UCSF} tomography: An integrated software suite for real-time electron microscopic tomographic data collection, alignment, and reconstruction. *Journal of Structural Biology*, 157(1):138 – 147, 2007. Software tools for macromolecular microscopy.

[123] S. Nickell, F. Förster, A. Linaroudis, W.D. Net, F. Beck, R. Hegerl, W. Baumeister, and J.M. Plitzko. {TOM} software toolbox: acquisition and analysis for electron tomography. *Journal of Structural Biology*, 149(3):227 – 234, 2005.

[124] J. Shi, D.R. Williams, and P.L. Stewart. A script-assisted microscopy (sam) package to improve data acquisition rates on {FEI} tecnai electron microscopes equipped with gatan {CCD} cameras. *Journal of Structural Biology*, 164(1):166 – 169, 2008.

[125] J. Kuo. *Electron Microscopy: Methods and Protocols*. Springer, 2007.

[126] C.R. Booth, J. Jakana, and W. Chiu. Assessing the capabilities of a 4kx4k ccd camera for electron cryo-microscopy at 300kv. *Journal of Structural Biology*, 156:556 – 563, 2006.

[127] P. Penczek, M. Marko, K. Buttle, and J. Frank. Double-tilt electron tomography. *Ultramicroscopy*, 3:393, 1995.

[128] C.H. Owen and W.J. Landi. Alignment of electron tomographic series by correlation without the use of gold particles. *Ultramicroscopy*, 63(1):27 – 38, 1996.

[129] M. Hayashida, T. Iijima, M. Tsukahara, and S. Ogawa. High-precision alignment of electron tomography tilt series using markers formed in helium-ion microscope. *Micron*, 50:29 – 34, 2013.

[130] P.A. Penczek. Fundamentals of three-dimensional reconstruction from projections. *Enzymology Methods*, 482:1–33, 2010.

[131] F. Natterer. *The Mathematics of Computerized Tomography.* SIAM: Society for Industrial and Applied Mathematics, 2001.

[132] S.W. Smith. *The Scientist and Engineer's Guide to Digital Signal Processing.* California Technical Publishing, San Diego, CA, 1997.

[133] N. Tanaka. An investigation of filter choice for filtered back-projection reconstruction in pet. *IEEE Transactions on Nuclear Science*, 45(3):1133, 1998.

[134] G.L. Zeng and A. Zamyatin. A filtered backprojection algorithm with ray-by-ray noise weighting. *Medical Physics*, 40(3):031113, 2013.

[135] W.J.C. Geerts, D. Zeuschner, J. Klumperman, and A.J. Koster. 3d electron tomography and edx: high-resolution imaging tools for cell biological applications, 2013.

[136] D. J. DeRosier R. A. Crowther and A. Klug. The reconstruction of a three-dimensional structure from projections and its application to electron mi-

croscopy. *Proceedings of the Royal Society of London*, 317(1530):319 – 340, 1970.

[137] R. Ng. Fourier slice photography. *ACM Transactions on Graphics*, 24(3):735 – 744, 2005.

[138] J. Berriman, R.K. Bryan, R. Freeman, and K.R. Leonard. Methods for specimen thickness determination in electron microscopy. *Ultramicroscopy*, 13:351, 1984.

[139] S. Brandt, J. Heikkonen, and P. Engelhardt. Multiphase method for automatic alignment of transmission electron microscope images using markers. *Journal of Structural Biology*, 133(1):10–22, 2001.

[140] D. Ress, M.L. Harlow, M. Schwarz, R.M. Marshall, and U.J. McMahan. Automatic acquisition of fiducial markers and alignment of images in tilt series for electron tomography. *Journal of Electron Microscopy*, 48(3):277–287, 1999.

[141] P.K. Luther, M.C. Lawrence, and R.A. Crowther. A method for monitoring the collapse of plastic sections as a function of electron dose. *Ultramicroscopy*, 24(7):1988, 1988.

[142] Z.Q. Jing and F. Sachs. Alignment of tomographic projections using an incomplete set of fiducial markers. *Ultramicroscopy*, 35:37, 1991.

[143] J.R. Kremer, D.N. Mastronarde, and J.R. McIntosh. Computer visualisation of three-dimensional image data using imod. *Journal of Structural Biology*, 116:71–76, 1996.

[144] J.C. Fung, W. Liu, W.J. de Ruitjer, H. Chen, C.K. Abbey, J.W. Sedat, and D.A. Agard. Toward fully automated high-resolution electron tomography. *Journal of Structural Biology*, 116(1):181–189, 1996.

[145] *Electron Tomography: Methods for Three-Dimensional Visualization of Structures in the Cell, Second Edition.* Springer Books, New York, 2006.

[146] R. Guckenberger. Determination of a common origin in the micrographs of tilt series in three-dimensional electron microscopy. *Ultramicroscopy*, 9:167–174, 1982.

[147] A.J. Koster, H. Chen, J.W. Sedat, and D.A. Agard. Automated microscopy for electron tomography. *Ultramicroscopy*, 46:207–227, 1992.

[148] P. Gilbert. Iterative methods for the three-dimensional reconstruction of an object from projections. *Journal of Theoretical Biology*, 36(1):105–117, 1972.

[149] B. Goris, T. Roelandt, K.J. Batenburg, H. Heidari Mezerji, and S. Bal. Advanced reconstruction algorithms for electron tomography: From comparison to combination. *Ultramicroscopy*, 127:40–47, 2013.

[150] T.R. Shaikh, H. Gao, W.T. Baxter, F.J. Asturias, N. Boisset, A. Leith, and J. Frank. Spider image processing for single-particle reconstruction of biological macromolecules from electron micrographs. *Nature Protocols*, 3:1941–1974, 2008.

[151] M .Hohn, G. Tang, G. Goodyear, P.R. Baldwin, Z. Huang, P.A. Penczek, Y.C, R.M. Glaeser, P.D. Adams, and S.J. Ludtke. Sparx, a new environment for cryo-em image processing. *Journal of Structural Biology*, 157:47–55, 2007.

[152] C. Messaoudii, T. Boudier, C.O. Sanchez Sorzano, and S. Marco. Tomoj: tomography software for three-dimensional reconstruction in transmission electron microscopy. *BMC Bioinformatics*, 8:288, 2007.

[153] C. Suloway, J. Shi, A. Cheng, J. Pulokas, B. Carragher, C.S. Potter, S.Q. Zheng, D.A. Agard, and G.J. Jensen. Fully automated, sequential tilt-series acquisition with leginon. *Journal of Structural Biology*, 167:111–118, 2009.

[154] L. Joyeux and P.A. Penczek. Efficiency of 2d alignment methods. *Ultramicroscopy*, 92:33–46, 2002.

[155] J.R. Bilbao-Castro, C.O. Sorzano, I. Garcia, and J.J. Fernandez. Phan3d: Design of biological phantoms in 3d electron microscopy. *Bioinformatics*, 20(17):3266 – 3288, 2004.

[156] R. Marabini, I.M. Masegosa, M.C. San Martin, J.J. Fernandez, L.G. de la Fraga, C. Vaquerizo, and J.M. Carazo. Xmipp: An image processing package for electron microscopy. *Journal of Structural Biology*, 116(1):237 – 240, 1996.

[157] R. Marabini, I.M. Masegosa, M.C. San Martin, J.J. Fernandez, L.G. de la Fraga, C. Vaquerizo, and J.M. Carazo. Xmipp: A new generation of an open-source image processing package for electron microscopy. *Journal of Structural Biology*, 148(2):194 – 204, 2004.

[158] J.M. de la Rosa-Trevin, J. Oton, R. Marabini, A. Zaldivar, J. Vargas, J.M. Carazo, and C.O. Sorzano. Xmipp 3.0: An improved software suite for image processing in electron microscopy. *Journal of Structural Biology*, 184(2):321 – 328, 2013.

[159] P.A. Penczek, R. Renka, and H. Schomberg. Gridding-based direct fourier inversion of the three-dimensional ray transform. *Optics InfoBase*, 4:499 – 509, 2004.

[160] T. Schneider. Shape and orientation effects on volume determination by microscopy of lath-shaped fibres modeled by trivariate log-normal size distributions. *Journal of Aerosol Science*, 24(7):963 – 971, 1993.

[161] J.R. Kremer, D.N. Mastronarde, and J.R. McIntosh. Computer visualization of three-dimensional image data using imod. *Journal of Structural Biology*, 116:71 – 76, 1996.

[162] P.A. Penczek, C. Yang, J. Frank, and C.M.T. Spahn. Fully automated, sequential tilt-series acquisition with leginon. *Journal of Structural Biology*, 167(1):11 – 18, 2009.

[163] H. Zhu, N. Li, and Z.J. Liu. 3d laser inner engraving path generation and simulation for crystal glass. *Advanced Materials Research*, 201:225 – 228, 2011.

[164] R. Partridge, N. Conlisk, and J.A. Davies. In-lab three-dimensional printing: An inexpensive tool for experimentation and visualization for the field of organogenesis. *Organogenesis*, 8(1):22 – 27, 2012.

[165] Stuffmaker. The creator 3d printer by stuffmaker, http://www.3dstuffmaker.com/creator-3d-printer.

[166] J. Lambard, P. Lesieur, and T. Zemb. A triple axis double crystal multiple reflection camera for ultra small angle x-ray scattering. *Journal of Physics I*, 2(6):1191 – 1213, 1992.

[167] A. Guinier and G. Fournet. *Small Angle Scattering of X-rays*. Wiley, New York, 1955.

[168] P. Lindner and Th. Zemb. *Neutrons, X-rays and Light: Scattering Methods Applied to Soft Condensed Matter*. Elsevier, North-Holland, 2002.

[169] R.J. Roe. *Methods of X-ray and Neutron Scattering in Polymer Science*. 0195113217, 2000.

[170] D.J. Griffiths. *Introduction to Quantum Mechanics*. Prentice-Hall, 1995.

[171] T. Narayanan, O. Diat, and P. Bosecke. Saxs and usaxs on the high brilliance beamline at the esrf. *Nuclear Instruments and Methods in Physics A*, 467(2):1005 – 1009, 2001.

[172] J.S. Pedersen. Analysis of small-angle scattering data from colloids and polymer solutions: Modeling and least-squares fitting. *Advances in Colloid and Interface Science*, 70:171–210, 1997.

[173] O. Glatter and O. Kratky. Small angle x-ray scattering. *Academic press London*, 102:17–52, 1982.

[174] G. Beaucage. Small-angle scattering from polymeric mass fractals of arbitrary mass- fractal dimension. *Journal of Applied Crystallography*, 29:134 – 146, 1996.

[175] J. Ilavsky, P.R. Jemian, A.J. Allen, F. Zhang, L.E. Levine, and G.G. Long. Ultra-small-angle x-ray scattering at the advanced photon source. *Journal of Applied Crystallography*, 42:469–479, 2009.

[176] J. Ilavsky and P.R. Jemian. Irena: tool suite for modeling and analysis of small-angle scattering. *Journal of Applied Crystallography*, 42:347–353, 2009.

[177] G. Beaucage. Approximations leading to a unified exponential/power-law approach to small-angle scattering. *Journal of Applied Crystallography*, 28:717–728, 1995.